UNIVERSITY OF SIENA

Department of Medical Biotechnologies

PhD Program in Medical Biotechnology

Section of Microbiology and Vaccines

XXIX Cycle

Alternative tools and new molecules proposed to face the antibiotic resistance crisis

Supervisor:
Prof. Gian Maria Rossolini
Co-Supervisor:
Dr. Lucia Pallecchi

PhD student:
Giulia Landini

2017

ACKNOWLEDGMENTS

I am sincerely grateful to my supervisor Prof. Gian Maria Rossolini for giving me the opportunity to carry out this PhD research and for his continuous support and precious advice.

I wish to thank very much Dr. Lucia Pallecchi for conveying to me her knowledge and enthusiasm in microbiology, and for helping me in developing critical thinking.

I would also like to thank Prof. Luca Gavioli for introducing me to the “nano-world” and for sharing such a challenging experience.

Finally, a special thanks to all the people in the “RossoLab” who supported me during the whole PhD period, especially Tiziana, Samanta, Antonio, Tommaso, Vincenzo, Eleonora, Fabio, Jean Denis, Nagaia, Viola, Alberto, Simona, Marco, Lucia.

FOREWORD

This thesis is divided in four parts: documentation requested, introduction to PhD research, summary results and discussion, and annexes.

The annexes include selected bibliography and all the related material that has been published or to be submitted to international scientific journals in relation to the thesis work and also one paper published in PhD period, but not discussed in the present work.

Contents

Part I

DOCUMENTATION

REQUESTED

Abstract

Multidrug- or pandrug-resistant microorganisms and bacterial biofilms are increasing issue of concern and represent two sides of the same coin, since threaten the very core of modern medicine and the sustainability of an effective, global public health response to the difficult-to-treat infections [Høiby N, 2015; Olsen L, 2015; WHO 2014]. The increasing awareness of the reduced efficacy of antibiotic has prompted the renewing of antibiotic discovery and development programs to fight the antibiotic resistance crisis. On this basis, strengthening behaviors have been aimed at reducing the dissemination of multidrug resistant pathogens (e.g. surveillance, infection control practices and adoption of antimicrobial stewardship programs) [Rossolini GM, 2014; Yokoe DS, 2014].

This PhD project approached this intriguing issue from different points of view.

With the purpose of evaluating the efficacy of recently introduced antimicrobial agents, the bactericidal activity of ceftaroline, a new broad-spectrum cephalosporin, was analyzed against mature *Staphylococcus aureus* biofilms. The detected activity of long-term treatment against mature staphylococcal biofilms reinforces previous findings and encourages further studies to consolidate ceftaroline within the armamentarium for the treatment of biofilm-associated staphylococcal infections.

Moreover, the evaluation of antimicrobial and anti-biofilm activity of well-known mucolytic agent *N*-acetylcysteine (NAC) have led to highlight promising efficacy against some clinically relevant respiratory pathogens (i.e. *Pseudomonas aeruginosa, S. aureus, Stenotrophomonas maltophilia*, *Burkholderia cepacia* complex, and *Haemophilus influenzae*). Obtained results bolstering foregoing findings and demonstrating for the first time the efficacy of NAC against emergent respiratory pathogens such as *S. maltophilia* and *B. cepacia* complex. In addition, no modulatory effect of NAC was observed on the activity of antibiotics with the exception of carbapenems, thus paving the way to further evaluation about a possible synergistic interaction between NAC and antibiotics against cells both in planktonic phase and biofilm.

The infection control practices were dealt by evaluating antimicrobial coatings composed of nanoparticles synthetized by supersonic cluster beam deposition apparatus (i.e. innovative deposition method which produces clusters without chemical synthesis). A broad-spectrum bactericidal activity of pure silver nanoparticles films deposited on microscope slides was demonstrated for the first time. Furthermore, the bactericidal activity of bi-metal nanoparticles (i.e.

50% silver and 50% titanium) on commercial chrome-plated support were analyzed, demonstrating that titanium remarkably enhances the adhesion of nanoparticles upon the supports and provides a comparable antimicrobial activity of pure silver nanoparticles, saving at the same time more than 85% of the expensive metal. Further exploitation of the supersonic cluster beam deposition apparatus would aim to generate nanoparticles coating with broader antimicrobial spectrum and anti-biofilm activity.

Several worldwide surveillance studies have shown the clonal dissemination of KPC-type carbapenemase-producing *Klebsiella pneumoniae* belonging to clonal complex 258 (CC258), characterized by extensively drug resistant phenotypes and ability to rapidly disseminate in healthcare settings. In order to deeply investigate the two differentially distributed lineages (i.e. clade I and clade II) belonging the CC258, genome analysis and biofilm forming assays were carried out. The prevalent distribution of clade II has been awarded to difference in the mrk mannose-resistant fimbrial gene cluster, since non-silent mutation on *mrkABCDFHIJ* cluster genes detected on clade I genome determined reduced fimbrial synthesis and biofilm forming ability on abiotic surfaces. Further studies aimed to evaluate the role of this mutation in the adhesion on biotic surfaces are needed to deeply explain such widespread dissemination.

Among novel techniques proposed to go beyond the antibiotic resistance crisis, the laser therapy has been considered an alternative tool. On this basis, the anti-biofilm activity of λ 808-nm diode laser was assessed. Mature staphylococcal biofilms grown on titanium discs (surface of the osseous interface of dental implants), however, were not eradicated by λ 808-nm diode laser, even if a significant reduction of microbial load was highlighted. λ 808-nm diode laser could be considered a valuable tool for increasing the odds of successful control of peri-implant diseases, probably combined with conventional therapy.

In conclusion, alternative tools and new molecules to fight difficult-to-treat infection (i.e. ceftaroline, *N*-acetylcysteine, and laser therapy), to contain and limit the indirect transmission of pathogens (i.e. antimicrobial coating composed of mono- or bi-metal nanoparticles), and to get novel insights on clonal dissemination of high-risk clone, are shown. Present results suggest encouraging outcome, but more efforts should be carried out in order to avoid the return to “pre-antibiotic era”.

Final Report

First year 2013-2014

Educational activities:

The PhD student attended a course of advanced english organized by the “Centro Linguistico di Ateneo” at the University of Siena, and two courses entitled “Valorizzazione dei risultati della ricerca e della proprietà intellettuale”; “Conoscenza dei sistemi di ricerca europei” organized by the University of Siena, in collaboration with the Liaison Office.

The PhD student also won an annual research grant on "Studio dell’attività antimicrobica di film di nanoparticelle di argento generati mediante sorgente supersonica di cluster", distributed by the University of Siena.

Partecipation to scientific conferences:

- 54th Interscience Conference on Antimicrobial Agents and Chemotherapy (ICAAC), Washington, USA.
- 15th Trends in Nanotechnology (TNT2014), Barcelona, Spain.
- 24th European Congress of Clinical Microbiology and Infectious Diseases (ECCMID), Barcelona, Spain.
- 42° Congresso nazionale Società Italiana Microbiologia (SIM), Turin, Italy.

Second year 2014-2015

Educational activities:

The PhD student, attended a weekly class by Prof. Andre Matagne and Prof. Jean-Marie Frere entitled “Functional and structural properties of proteins: theory and practice” and seminar "Zinc as a key player in metallo-beta-lactamase activity and stability" at the University of Siena.

The annual research grant has been renewed on "Studio dell’attività antimicrobica di film di nanoparticelle di argento generati mediante sorgente supersonica di cluster", distributed by the University of Siena.

Scientific publications:

- Bactericidal activity of ceftaroline against mature *Staphylococcus aureus* biofilms. G. Landini, E. Riccobono, T. Giani, F. Arena, G.M. Rossolini, L. Pallecchi. *International Journal of Antimicrobial Agents*.
- Highly bactericidal Ag nanoparticle films obtained by cluster beam deposition. E. Cavaliere, S. De Cesari, G. Landini, E. Riccobono, L. Pallecchi, G.M. Rossolini, L. Gavioli. *Nanomedicine: Nanotechnology, Biology and Medicine*.

Partecipation to scientific conferences:

- 43° Congresso nazionale Società Italiana Microbiologia (SIM), Naples, Italy.

Third year 2015-2016

Educational activities:

The PhD student won an annual research grant on "Studio della sensibilità agli antibiotici di patogeni respiratori cresciuti come biofilm ", distributed by the University of Siena.

Scientific publications:

- Characterization of KPC-encoding plasmids from two endemic settings, Greece and Italy. C.C. Papagiannitsis, V. Di Pilato, T. Giani, P. Giakkoupi, E. Riccobono, G. Landini, V. Miriagou, A.C. Vatopoulos, G.M. Rossolini. *Journal of Antimicrobial Chemotherapy*.
- The effects of diode laser on *Staphylococcus aureus* biofilm and *Escherichia coli* lipopolysaccharide adherent to titanium oxide surface of dental implants. An *in vitro* study. M. Giannelli, G. Landini, F. Materassi, F. Chellini, A. Antonelli, A. Tani, S. Zecchi-Orlandini, G.M. Rossolini, and D. Bani. *Lasers in Medical Science*.
- Effect of high *N*-acetylcysteine concentrations on antibiotic activity against a large collection of respiratory pathogens. G. Landini, T. Di Maggio, F. Sergio, J.D. Docquier, G.M. Rossolini, and L. Pallecchi. *Antimicrobial Agents and Chemotherapy*.

Partecipation to scientific conferences:

- European Respiratory Society International Congress (ERS), London, UK.
- 44° Congresso nazionale Società Italiana Microbiologia (SIM), Pisa, Italy.
- XLV Congresso nazionale Associazione Microbiologi Clinici Italiani (AMCLI), Rimini, Italy.
- 4th Italian experience in biomedical research: young minds at work, Desenzano del Garda, Italy.

Awards:

- Award for best poster session for Bacteriology, Mycology and Parasitology during 44° Congresso nazionale Società Italiana Microbiologia (SIM), Pisa, Italy.

Part II

INTRODUCTION

TO

PhD RESEARCH

PhD research: General Objective

The General Objective of the PhD research was investigating altarnative tools to combat, prevent and deeply analyze the widespread dissemination of high-risk clones and biofilm-associated infections.

The antimicrobial and anti-biofilm efficacy of conventional and non-conventional treatments were evaluated (i.e. ceftaroline, *N*-acetylcysteine, laser therapy). Deepened investigations of the possible reasons behind widespread dissemination of high-risk clone (*Klebsiella pneumoniae* sequence type 258) were performed. Moreover, analysis of the efficacy of antimicrobial coatings which could limit the indirect transmission of pathogens (i.e. nanoparticles films produced by supersonic cluster beam deposition) were carried out.

PhD research: Specific Topics addressed

In detail, the PhD research focused on the following specific topics:

- Determination of the *in vitro* activity of a new broad-spectrum cephalosporin, ceftaroline, against mature *Staphylococcus aureus* biofilms.

- Investigation of the antimicrobial and anti-biofilm activity of *N*-acetylcysteine against clinically relevant respiratory pathogens.

- Evaluation of efficacy of antimicrobial coatings composed of metallic nanoparticles films produced by supersonic cluster beam deposition technique (i.e. pure silver nanoparticles and bi-metal nanoparticles composed of silver and titanium).

- Study of the mechanisms involved in the differential dissemination of two clades of sequence type 258 KPC-producing *Klebsiella pneumoniae* linked to different expression of the Mrk fimbiral system.

- Determination of the effect of diode laser against mature *Staphylococcus aureus* biofilm grown on titanium oxide surface of dental implants.

Part III

SUMMARY OF RESULTS AND DISCUSSION

1

Bactericidal activity of ceftaroline against mature *Staphylococcus aureus* biofilms

Related Publications:

- Landini G, Riccobono E, Giani T, Arena F, Rossolini GM, and Pallecchi L. 2015. Bactericidal activity of ceftaroline against mature *Staphylococcus aureus* biofilms. *International journal of antimicrobial agents*, 45(5), 551.

Staphylococcus aureus biofilms represent a major clinical challenge in some infections, including those of artificial devices (and related bloodstream infections), osteomyelitis, endocarditis and complicated skin and soft tissue infections [Hall-Stoodley L, 2004]. To note, cells embedded in biofilm are poorly susceptible to host defenses and antimicrobial drugs, and treatment failures/recurrences are often observed in absence of debridement or removal of contaminated medical devices [Hall-Stoodley L, 2004; Lewis K, 2007]. Several mechanisms account for biofilm-associated antimicrobial tolerance (i.e. the ability of sessile cells to survive killing by antimicrobials without expressing resistance mechanisms). Among them, the most relevant is the presence of persisters, which are dormant, non-dividing cells exhibiting multidrug tolerance [Lewis K, 2007]. While great efforts and promising advances have been made in the development of innovative anti-biofilm strategies during the last decade [Bjarnsholt T, 2013; Conlon BP, 2013], conventional medical treatment of staphylococcal biofilm-associated infections continues to rely upon combination antibiotic therapy for prolonged periods [Bjarnsholt T, 2013]. Following the ever increasing prevalence of methicillin-resistant *S. aureus* (MRSA) isolates worldwide, the activity of anti-MRSA agents against staphylococcal biofilms is a matter of increasing interest [Kiedrowski MR, 2011].

Ceftaroline, the active metabolite of ceftaroline fosamil, is a new broad-spectrum cephalosporin exhibiting bactericidal activity against *S. aureus*, including MRSA isolates [Saravolatz LD, 2011]. Recently, ceftaroline combinations with either daptomycin or vancomycin were found to exert *in vitro* bactericidal activity (>3 log reduction in viable cell count) against one day-old MRSA biofilms

after 24 hours of exposure, although exposure to ceftaroline alone did not result in sustained killing (i.e. regrowth was observed within 8 hours in presence of a ceftaroline concentration of 2 μg/ml) [Barber KE, 2014].

Aiming to investigate the anti-biofilm activity of ceftaroline as a long-lasting monotherapy, we challenged five mature (four days-old) staphylococcal biofilms (i.e. one MSSA and one MRSA reference strain, and four MRSA clinical isolates) with ceftaroline for prolonged exposure times at antibiotic concentrations achievable *in vivo* (range 16-0.03 μg/ml). In agreement with data reported in the single previous study on anti-staphylococcal biofilm activity of ceftaroline [Barber KE, 2014], MICB (Minimum Inhibitory Concentration of planktonic cells shed from Biofilms), MBEC (Minimum Biofilm Eradication Concentration) and MVCC (Mean Viable Cell Count per peg) were determined at day 1, 2, 3 and 6 of exposure [Harrison JJ, 2010]. For biofilm time-kill curves, the *S. aureus* ATCC 6538 was used as a model and tested with all the ten ceftaroline concentrations. For all the other strains, time-kill curves were determined using ceftaroline 2 and 8 μg/ml, plus a concentration corresponding to the MIC values of each isolates. In addition, vancomycin was also used as a comparator in time-kill curves of the reference MSSA strain ATCC 6538.

MICBs ranged within one doubling dilution of the respective MICs and were stable over the 6-day challenge experiment, demonstrating that no resistant mutants were selected under these conditions (Table 1). MBECs remained above the maximum ceftaroline concentration tested (i.e. >16 μg/ml) for all tested strains (Table 1). However, despite the lack of complete biofilm eradication, time-kill curves of ATCC 6538 biofilm revealed a bactericidal activity already after 24 hours of exposure at a ceftaroline concentration achievable *in vivo* (16 μg/ml) (Figure 1A). Starting from day 2, a bactericidal effect was already observed at concentrations as low as the MIC (0.25 μg/ml), and the MVCC fell below the limit of detection (1.1 log CFU/peg) at concentrations ≥8 μg/ml and ≥1 μg/ml after 3 days and 6 days of exposure, respectively. In agreement with the known time-dependent activity of ceftaroline [Lewis K, 2007], no concentration-dependent effect was observed (Figure 1A). At the tested concentrations, vancomycin appeared to be significantly less effective than ceftaroline against mature staphylococcal biofilms (Figure 1B), congruent with the lower anti-biofilm activity of vancomycin compared with another anti-MRSA cephalosporin recently demonstrated in a similar experimental model [Kiedrowski MR, 2011]. Time-kill curves of the four MRSA strains were overall in agreement with those of MSSA ATCC 6538 (Figure 1C-F). In particular, MRSA ATCC 43300 and MRSA-IT1 showed similar time–kill curves characterized by absence of killing at ceftaroline concentrations equal to MICs and lack of a concentration-dependent effect at

concentrations higher than the MIC (Figure 1C, and Figure 1D). Despite the clinical strains MRSA-IT16 and MRSA-IT23 producing a less abundant and less homogeneous biofilm, the overall response to ceftaroline was coherent (Figure 1E, and Figure 1F).

In conclusion, we demonstrated that, following prolonged exposure times, ceftaroline exerted a bactericidal activity both against MSSA and MRSA biofilms. These results reinforce previous findings on the *in vitro* efficacy of ceftaroline combinations against staphylococcal biofilms [Barber KE, 2014] and encourage further studies on the role of ceftaroline for the treatment of biofilm-associated staphylococcal infections.

Table 1. Features of the *Staphylococcus aureus* isolates investigated and anti-biofilm activity of ceftaroline.

Strain	Origin	Antibiotic susceptibility of planktonic cells										Ceftaroline activity against mature biofilms							
		MIC [a,b]										Day 1		Day 2		Day 3		Day 6	
		CPT	ERY	CLI	CN	LEV	VAN	TEI	LZD	TGC	DPC	MICB [b]	MBEC [b]	MICB	MBEC	MICB	MBEC	MICB	MBEC
ATCC 6538	ATCC	0.25	0.25	<0.12	0.25	0.25	1	0.25	1	0.12	0.5	0.25	>16	0.25	>16	0.25	>16	0.25	>16
ATCC 43300	ATCC	1	>16	>4	>4	0.25	1	0.5	4	0.12	0.5	1	>16	1	>16	1	>16	1	>16
MRSA-IT1 [c,d]	Blood	0.5	0.5	0.25	2	8	2	4	2	0.25	4	1	>16	1	>16	1	>16	1	>16
MRSA-IT16 [d]	Wound	2	>16	>4	>4	>16	1	2	4	>1	1	2	>16	2	>16	2	>16	2	>16
MRSA-IT23 [d]	CSF	2	>16	>4	>4	>16	1	2	2	0.5	1	2	>16	2	>16	2	>16	2	>16

MIC, minimal inhibitory concentration; CPT, ceftaroline; ERY, erythromycin; CLI, clindamycin; CN, gentamicin; LEV, levofloxacin; VAN, vancomycin; TEI, teicoplanin; LZD, linezolid; TGC, tigecycline; DPC, daptomycin; MICB, minimum inhibitory concentration of planktonic cells shed from biofilms; MBEC, minimum biofilm eradication concentration; MRSA, meticillin-resistant *S. aureus*; CSF, cerebrospinal fluid.

[a] MICs were determined in triplicate using a commercial kit (TREK BMD custom panel; Thermo Fisher Scientific, Oakwood Village, OH).

[b] MICs, MICBs and MBECs are expressed in μg/ml.

[c] *Staphylococcus aureus* MRSA-IT1 was categorized as heterogeneous vancomycin-intermediate *S. aureus* (hVISA) based on the population analysis profile–area under the curve (PAP-AUC) method [Wootton M, 2001].

[d] By characterization of staphylococcal cassette chromosome *mec* (SCC*mec*) elements [Kondo Y, 2007] and staphylococcal protein A (*spa*) typing [Harmsen D, 2003], the MRSA clinical strains were assigned to non-typeable *spa* type/SCC*mec* IV (MRSA-IT1), t041/SCC*mec* I (MRSA-IT16) and t288/SCC*mec* I (MRSA-IT23).

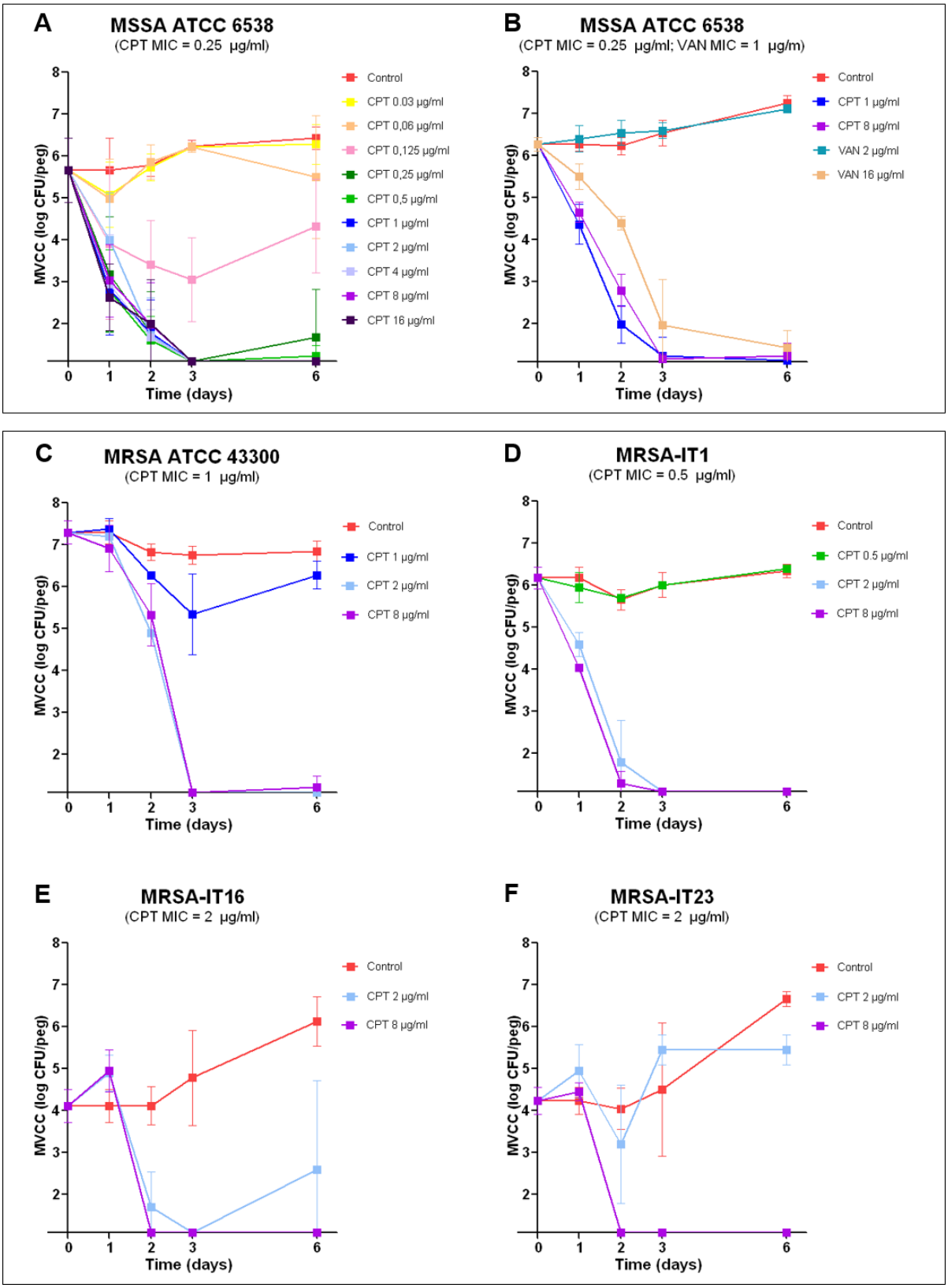

Figure 1. Time-kill curves of *S. aureus* biofilms exposed to ceftaroline (CPT). (A) MSSA reference strain ATCC 6538 exposed to ten CPT concentrations achievable *in vivo*. (B) MSSA reference strain ATCC 6538 exposed to CPT or vancomycin (VAN) at 1× and 8× the susceptibility breakpoints. (C–F) MRSA reference strain ATCC 43300 and three MRSA clinical strains exposed to ceftaroline ≥MICs. The *x*-axis is set at the limit of detection. Error bars represent standard deviations. MVCC, mean viable cell count.

2

N-acetylcysteine: antimicrobial activity against clinically relevant respiratory pathogens grown in planktonic phase and biofilm

Related Publications:

- Landini G, Di Maggio T, Sergio F, Docquier JD, Rossolini GM, and Pallecchi L. 2016. Effect of high *N*-acetylcysteine concentrations on antibiotic activity against a large collection of respiratory pathogens. *Antimicrobial Agents and Chemotherapy*, AAC-01334.

N-acetylcysteine (NAC) has been used since the early 1960s as a mucolytic agent [Hurst GA, 1967], thanks to its capacity of disrupting disulfide bridges within the glycoprotein matrix of mucus [Rushworth GF, 2014; Samuni Y, 2013]. Moreover, acting as a precursor of glutathione (GSH, a key intracellular detoxifying and antioxidant agents) and as a source of reduced thiol moieties, NAC has been shown to interact with several biochemical pathways via complex and still partially understood mechanisms [Rushworth GF, 2014; Samuni Y, 2013]. In fact, NAC has been used for decades for the treatment of paracetamol intoxication and, more recently, its therapeutic potential has been investigated for a wide range of other diseases where oxidative stress is considered a trigger (e.g. cardiovascular diseases, cancer, neuropsychiatric disorders) [Rushworth GF, 2014; Samuni Y, 2013]. NAC is commonly administered together with antibiotics for the treatment of respiratory tract infections and, considering its likely multifactorial beneficial impact (i.e. mucolytic, antioxidant, and anti-inflammatory), there has been also a growing interest for evaluating its role in the management of cystic fibrosis (CF) and other chronic respiratory diseases (e.g. chronic obstructive pulmonary disease - COPD, bronchiectasis) [Cazzola M, 2015; Rushworth GF, 2014; Skov M, 2015].

In this contest, we investigated the intrinsic antimicrobial and anti-biofilm activity of NAC against a large collection of respiratory pathogens, and we performed a study to evaluate the effect of high NAC concentrations on the activity of several antibiotics.

- **Antimicrobial activity of *N*-acetylcysteine against a large collection of respiratory pathogens**

Despite *in vitro* antimicrobial activity of NAC was first observed in the late 1970s [Parry MF, 1977] the underlying mechanisms remain largely unknown, and important knowledge gaps and relevant inconsistencies characterize the data published on this topic over the last decades. Limitations of previous studies include both the type, origin and number of tested strains (i.e. only few type of pathogens, mostly reference strains but not clinical isolates, usually a very low number of strains investigated in each study [Goswami M, 2010; Moon JH, 2016]), the antimicrobial susceptibility testing procedures adopted (i.e. diverse approaches, often preventing direct data comparison [Aslam S, 2011; Olofsson AC, 2003]), and possibly important experimental issues [Rodríguez-Beltrán J, 2015].

To overcome limitations of previous data, the antimicrobial activity of NAC, with a special focus on respiratory pathogens, were evaluated by performing diverse antimicrobial susceptibility testing procedures.

A total of 140 reference and clinical strains of the major respiratory pathogens (i.e. *Escherichia coli, Klebsiella* spp.*, Enterobacter cloacae, Pseudomonas aeruginosa, Acinetobacter baumannii, Stenotrophomonas maltophilia*, *Burkholderia cepacia* complex – BCC, *Moraxella catarrhalis, Haemophilus influenzae, Staphylococcus aureus, Streptococcus pyogenes, Streptococcus pneumoniae,* and *Corynebacterium striatum*), including strains with resistance phenotypes of clinical relevance, were selected. Minimal Inhibitory Concentrations (MICs) [CLSI M07-A10, 2015], Minimum Bactericidal Concentrations (MBCs) [CLSI M26-A, 1999], effect of NAC on the growth kinetics and time-kill assay were performed [CLSI M26-A, 1999].

MICs were determined, using NAC ranging from 16 to 0.03 mg/ml in all respiratory pathogens analyzed, except for *S. maltophilia* and BCC isolates, where the highest concentration tested was 32 mg/ml. MICs were >16 mg/ml for the majority of pathogens tested, with the notable exception of three *P. aeruginosa*, two *A. baumannii,* and a consistent number of *H. influenzae* strains (i.e. 15 out of 20) (Table 2). All the MICs of *S. maltophilia*, and BCC tested were ranged from 32 to 16 mg/ml (Table 2). Of note, NAC was shown to exert bactericidal activity against one and three strains of *S. maltophilia* which showed MBC = 16 mg/ml and MBC = 32 mg/ml, respectively, and one BCC clinical isolate with MBC = 32 mg/ml (Table 2).

The growth curves were performed to evaluate the effect of sub-MIC concentrations of NAC on the growth kinetics. Bacteria cultures, dispensed in microtiter plate, were monitored by measuring the absorbance at 600 nm up to 20 hours, with exception of *S. maltophilia*, BCC, *M. catarrhalis*, *S. pneumoniae*, and *C. striatum* where macro-volumes were performed due to not optimal results

obtained in microplates. Two fixed NAC concentrations (i.e. 4 and 16 mg/ml) were chosen to challenge clinical isolates with MICs >16 mg/ml, meanwhile only 4 mg/ml was tested for strains in which MIC was 16 mg/ml. Sub-MIC NAC concentrations were demonstrated to be able to slow down the growth of a relevant number of strains, belonging to the majority of bacterial species investigated. However, heterogeneity was observed both in the percentage of affected strains within each species and in the level of growth inhibition, demonstrating a strain dependent effect. *P. aeruginosa, A. baumannii*, *S. maltophilia,* BCC, and *M. catarrhalis* resulted the most affected species, with a clear inhibitory effect on bacterial growth curves observed at sub-MIC NAC concentrations with the majority of tested isolates (Figure 2 and Figure 3).

To further access the *in vitro* efficacy of NAC, time-kill assays with a panel of 14 respiratory pathogens were undertaken. *H. influenzae* (n=3), *P. aeruginosa* (n=1)*, A. baumannii* (n=2), *S. maltophilia* (n=4), and *B. cepacia* complex (n=4) were chosen on the basis of MIC values (i.e. MIC =16 mg/ml). Both planktonic cells in exponential and stationary phase of growth were tested in the presence and absence of 16 and 32 mg/ml of NAC (determining the number of viable cells at 3, 6 and 24 hours of exposure) with the exception of *H. influenzae* strains, for which only the exponential phase of growth was tested due to bacterial instability in the buffer used for testing cells in stationary phase of growth. Assays, performed with cells in exponential phase of growth, showed antibacterial activity of NAC for all the eleven *S. maltophilia*, BCC and *H. influenzae* strains investigated, while no activity was evidenced against *P. aeruginosa* and *A. baumannii* clinical isolates (Figure 4). In particular, NAC at 32 mg/ml was bactericidal (i.e. caused a reduction of bacterial inoculum by more than 3 logs) against one *S. maltophilia* and one BCC isolate, and accounted for a reduction ranging from 1.1 to 1.7 log CFU/ml with four additional isolates (one *H. influenzae*, two *S. maltophilia* and one BCC) (Figure 4). Otherwise, no major effect was observed with the remaining isolates (Figure 4). A slight killing activity of NAC was also observed against cells in stationary phase of growth (i.e. late-stationary phase cultures resuspended in Phosphate Buffer Saline - PBS), with a reduction of 0.5-1 log CFU/ml achieved with all except one strains at NAC 32 mg/ml (Figure 5).

In conclusion, we highlighted the intrinsic antimicrobial activity of NAC against a relevant number respiratory pathogens, including *S. maltophilia*, *B. cepacia* complex, *H. influenzae*, and few strains of *P. aeruginosa* and *A. baumannii*. Moreover, the MBC determination, and time-kill assays demonstrated killing activity of NAC against some *H. influenzae, S. maltophilia*, and BCC clinical isolates, exerting bactericidal effect against one *S. maltophilia* and one BCC at 32 mg/ml. Sub-MIC concentrations of NAC were found to slow down the growth of a relevant number of tested strains, indeed the degree of growth rate inhibition appeared to be proportional to the NAC exposures with

P. aeruginosa, A. baumannii, *S. maltophilia*, *B. cepacia* complex, *H. influenzae*, and *M. catarrhalis* clinical isolates. All these findings suggested additional beneficial effect of NAC in the management of respiratory tract infections which could be added to its mucolytic, antioxidant, and anti-inflammatory proprieties.

Table 2. Minimal Inhibitory Concentration (MIC) and Minimal Bactericidal Concentration (MBC) of the 140 clinical isolates included in the study.

Strain	MIC mg/ml (n)	MBC mg/ml (n)
Escherichia coli (n=6)	>16 (6)	-
***Klebsiella* spp.** (n=14)	>16 (14)	-
Enterobacter cloacae (n=5)	>16 (5)	-
Pseudomonas aeruginosa (n=16)	16 (3), >16 (13)	-
Acinetobacter baumannii (n=10)	16 (2), >16 (8)	-
Stenotrophomonas maltophilia (n=15)	16 (10), 32 (5)	16 (1), 32 (3)
***Burkholderia cepacia* complex** (n=15)	16 (7), 32 (8)	32 (1)
Moraxella catarrhalis (n=11)	>16 (11)	-
Haemophilus influenzae (n=20)	16 (15), >16 (5)	-
Staphylococcus aureus (n=10)	>16 (10)	-
Beta-hemolytic streptococci (n=6)	>16 (6)	-
Streptococcus pneumoniae (n=10)	>16 (10)	-
Corynebacterium striatum (n=2)	>16 (2)	-

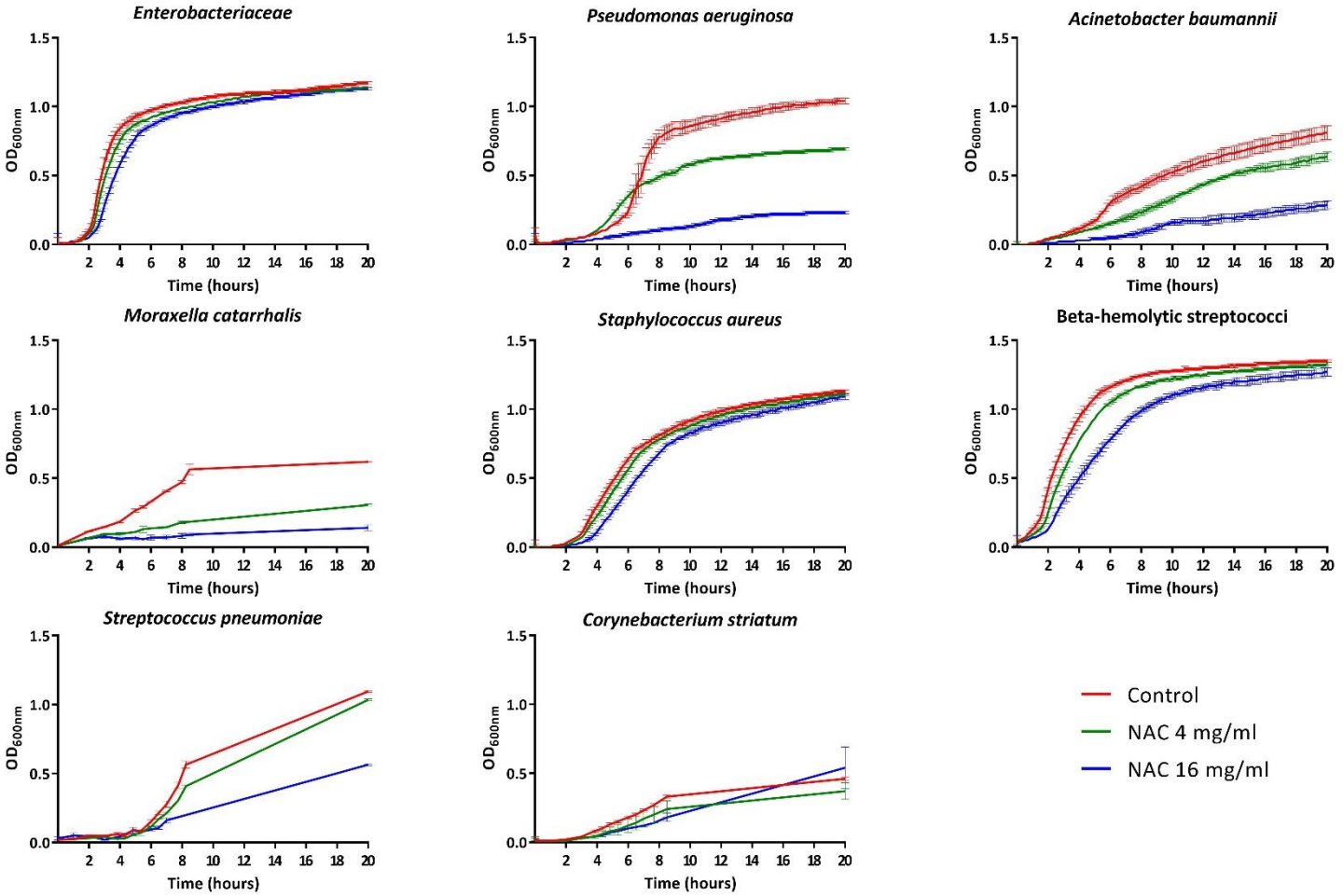

Figure 2. Explicative growth curves of one strain for each family/species (NAC MIC >16 mg/ml). Optical density at 600 nm (OD_{600nm}) of bacterial cultures dispensed in microtiter plates were monitored over 20 hours, in at least two replicates per condition; *M. catarrhalis, S. pneumoniae*, and *C. striatum* growth curves were performed in macro-volumes because of not optimal results obtained in microplates. Turbidity measurements were plotted over time to construct growth curves.

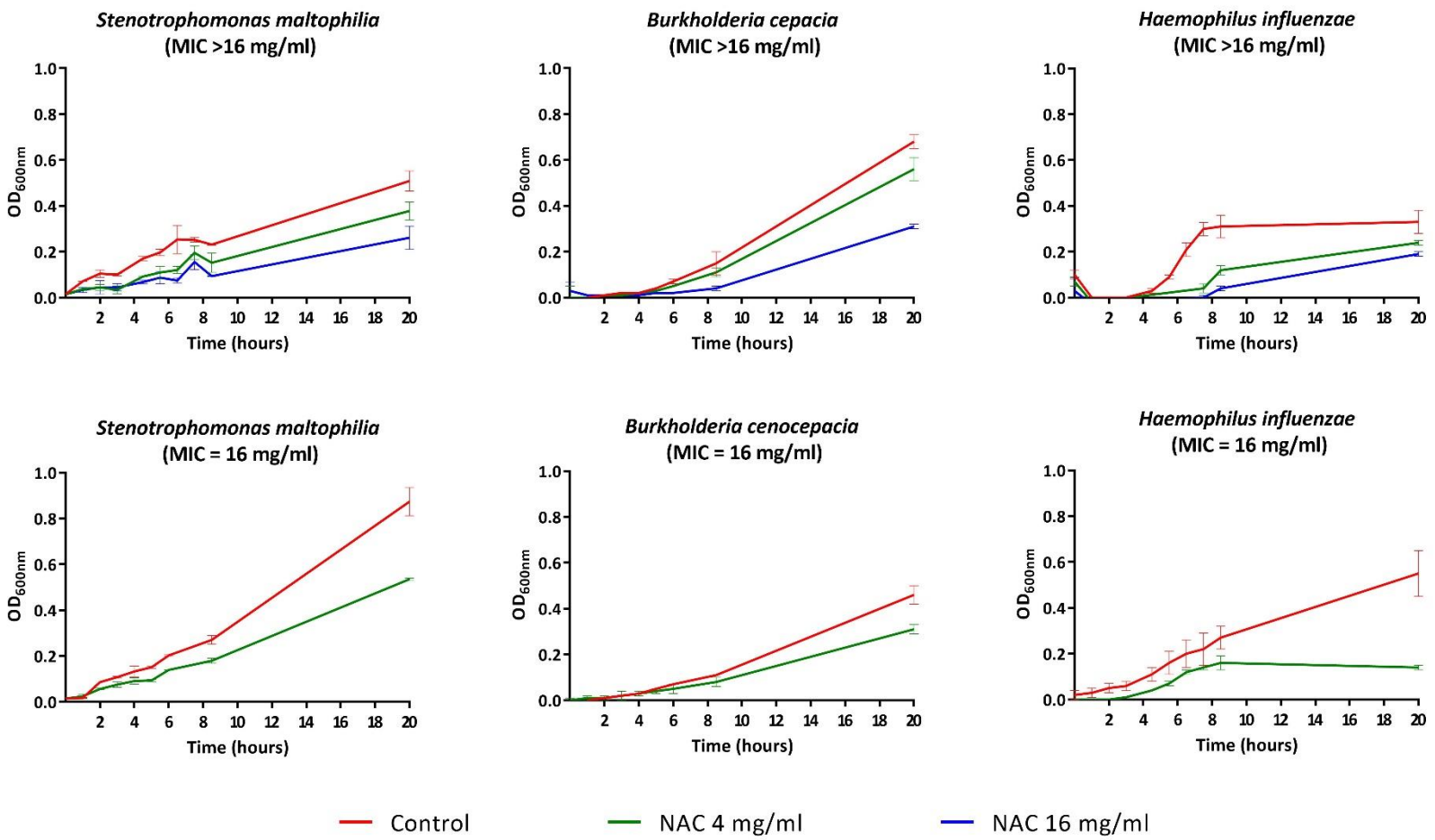

Figure 3. Explicative growth curves of two strains for each species characterized by MIC >16 and MIC =16 mg/ml of NAC. Optical density at 600 nm (OD_{600nm}) of bacterial cultures in macro-volumes were monitored over 20 hours, in at least two replicates per condition because of not optimal results obtained in microplates. Turbidity measurements were plotted over time to construct growth curves.

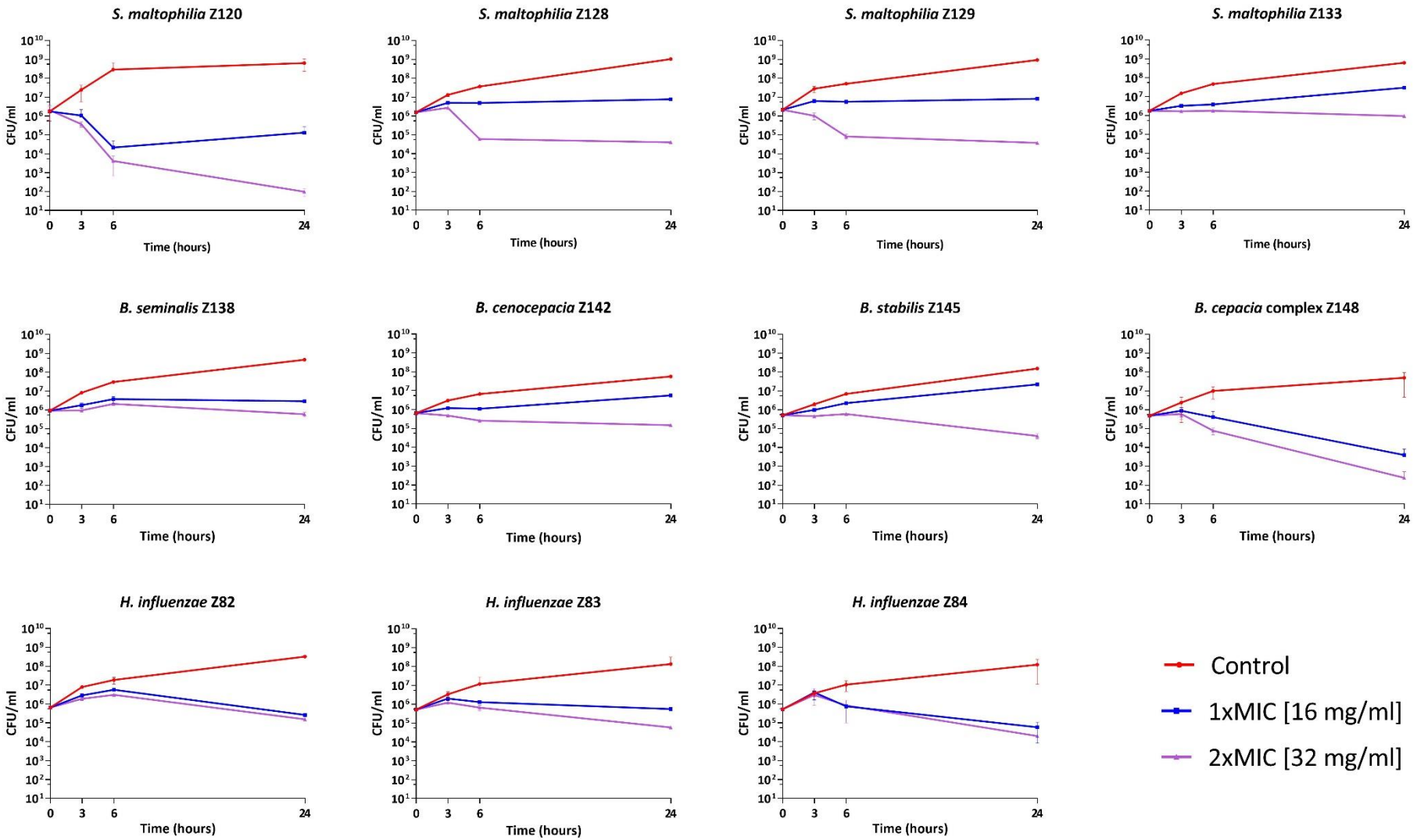
S. maltophilia Z120
S. maltophilia Z128
S. maltophilia Z129
S. maltophilia Z133
B. seminalis Z138
B. cenocepacia Z142
B. stabilis Z145
B. cepacia complex Z148
H. influenzae Z82
H. influenzae Z83
H. influenzae Z84
CFU/ml
Time (hours)
0
3
6
24
Control
1xMIC [16 mg/ml]
2xMIC [32 mg/ml]

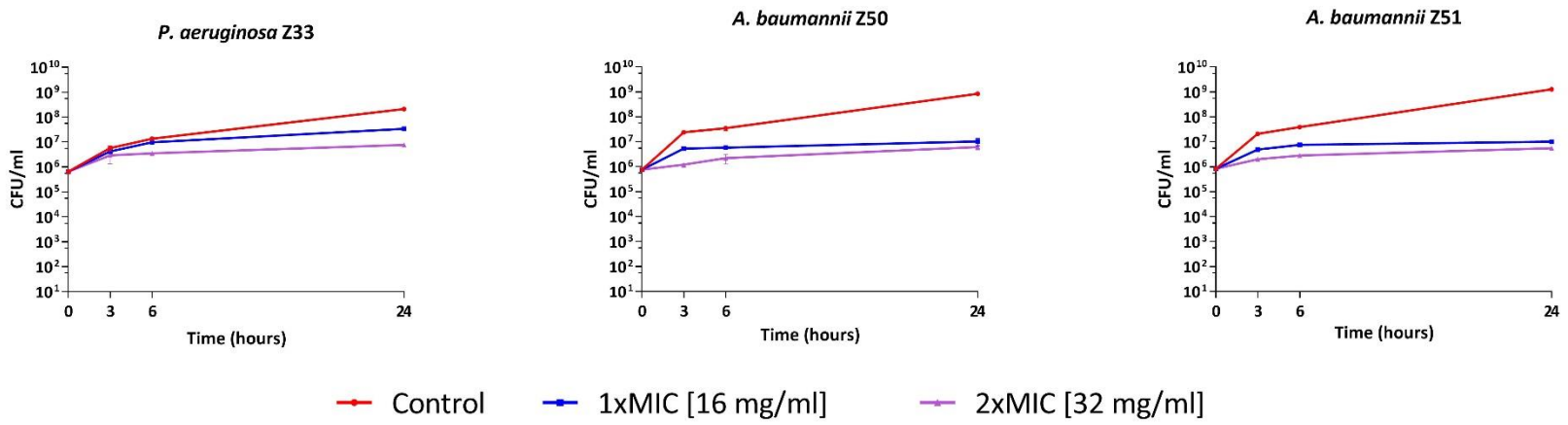

Figure 4. Time-kill assays with planktonic cells in exponential phase. Selected clinical isolates with MIC =16 mg/ml were challenged against 16 and 32 mg/ml of NAC (i.e. 1xMIC and 2xMIC, respectively); viable cell count (VCC, CFU/ml) were determined after 3, 6 and 24 hours of exposition, in at least two replicates per condition per experiment. Time-kill curves were constructed by plotting mean colony counts versus time.

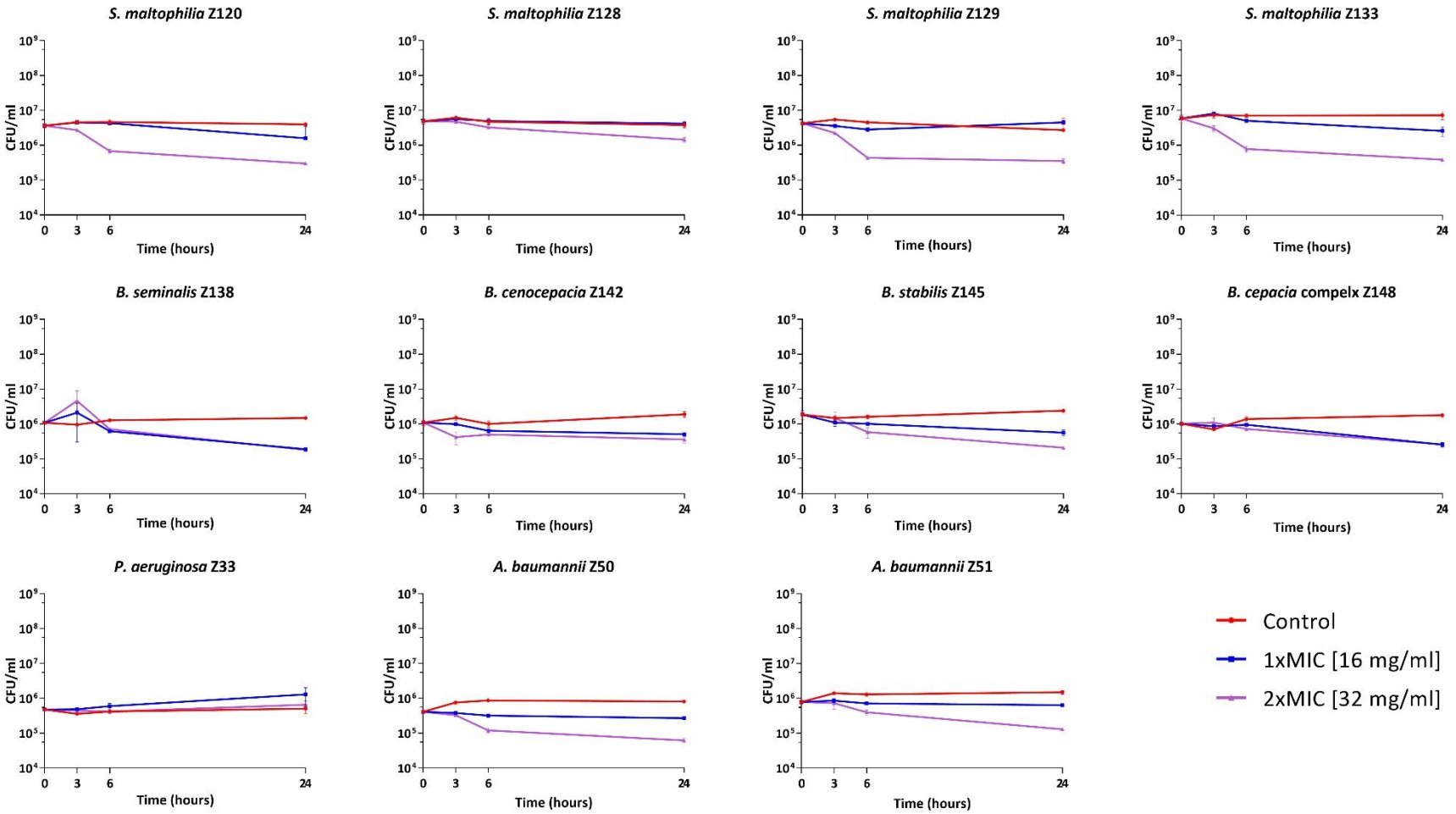

Figure 5. Time-kill assays with planktonic cells in stationary phase of growth. Selected clinical isolates with MIC =16 mg/ml were challenged against 16 and 32 mg/ml of NAC (i.e. 1xMIC and 2xMIC, respectively); viable cell count (VCC, CFU/ml) were determined after 3, 6 and 24 hours of exposition, in at least two replicates per condition per experiment. Time-kill curves were constructed by plotting mean colony counts versus time.

- **Anti-biofilm activity of *N*-acetylcysteine against clinically relevant respiratory pathogens**

In vitro anti-biofilm activity of NAC has been suggested for a wide range of microbial pathogens, including Gram positives (i.e. *Staphylococcus* spp., *Enterococcus faecalis* [Aslam S, 2007; Aslam S, 2011; El-Feky MA, 2009; Mansouri MD, 2013; Perez-Giraldo C, 1997]), Gram negatives (i.e. *E. coli*, *K. pneumoniae*, *E. cloacae*, *Proteus vulgaris*, *P. aeruginosa*, *A. baumannii* [Aslam S, 2007; Aslam S, 2011; El-Feky MA, 2009; Mansouri MD, 2013; Olofsson AC, 2003; Zhao T, 2010]), anaerobes (i.e. *Prevotella intermedia* [Moon JH, 2015]), and yeasts (i.e. *Candida albicans* [El-Baky RMA, 2014]). Nonetheless, a comprehensive interpretation of the published data is not straightforward, due to: i) the diverse parameters used for evaluating NAC anti-biofilm activity (e.g. inhibition of biofilm formation *vs.* eradication of preformed biofilms); ii) the very heterogeneous experimental approaches adopted for growing (e.g. different supports, diverse times of growth) and analyzing biofilms (e.g. measure of biofilm mass by crystal violet staining; viable cell count). In addition, the majority of those studies involved only a very limited number of strains (usually not characterized for their phenotypic/genotypic features).

Here, a study for the evaluation of the anti-biofilm activity of NAC, with a special focus on biofilms formed by respiratory pathogens, was proposed.

The anti-biofilm activity of NAC in both inhibiting biofilm formation and eradicating mature biofilm were evaluated against *P. aeruginosa* (n=6)*, S. aureus* (n=6)*, S. maltophilia* (n=4) and *B. cepacia* complex (n=5) respiratory pathogens including reference and clinical isolates, characterized by susceptible and multidrug resistance phenotype, from different origin (Table 3). Susceptibility testing were performed using the MBEC High-Throughput Assay (also known as Calgary Biofilm Device), and evaluated by viable cell count (VCC) [Harrison JJ, 2010]. Moreover, other biofilm models (i.e. flat-bottom microtiter plates or titanium discs) were used to consolidate possibly misleading results. Biofilms were treated with different NAC concentrations ranging from 16 to 0.16 mg/ml, and including 32 mg/ml in the treatment of mature biofilms. Data were obtained in two independent experiments, with at least four replicates per condition per experiment. Comparisons between VCC of treated and untreated biofilms were analyzed using an unpaired *t*-tests (Graph-Pad Prism 7.0), and results were considered statistically significant if p value ≤0.01.

The anti-biofilm activity of NAC against *P. aeruginosa* was found to be strain-dependent. In particular, a trend toward an inhibitory effect of NAC on biofilm formation was observed in 2 out of 6 tested strains (Figure 6a). On the contrary, no inhibition of biofilm formation was observed for the remaining four isolates, and a “paradoxical” effect (resulting in higher VCC) was observed with *P. aeruginosa* Z34 and *P. aeruginosa* Z38 at the highest NAC concentrations tested (i.e. NAC 16 mg/ml) (Figure 6a). The obtained results were also corroborated in two different *in vitro* models

(i.e. flat-bottom microtiter plates and titanium discs) (data not shown). Whilst the biofilm inhibitory effect observed with clinically relevant *P. aeruginosa* strains (including also a strain resistant to all available antibiotics – *P. aeruginosa* Z29) is promising, further studies would be warranted for understanding the mechanisms accounting for the "paradoxical" effect observed at high NAC concentrations with two strains (e.g. starting from the analysis of any possible experimental variable that might have biased the behavior of the two specific strains in the *in vitro* biofilm models used), and determine the frequency of such phenomenon in a larger collection of *P. aeruginosa* isolates from respiratory tract infections. Regarding the NAC activity against mature *P. aeruginosa* biofilms, the exposure to high NAC concentrations (i.e. 16 and 32 mg/ml) resulted in a decrease in viable cell count of four *P. aeruginosa* clinical isolates (Figure 6b). Among them, the major effect was observed in mature biofilm of the reference strain *P. aeruginosa* PAO-1, where a statistical significant reduction of VCC were highlighted after 24-hours-treatment with 8, 16 and 32 mg/ml of NAC (1.2, 0.8, and 1.7 log CFU/peg reduction, respectively) (Figure 6b). On the basis of results obtained, further studies would be focused on the evaluation of long-term-treatment of NAC alone against mature biofilms (e.g. by biofilm time-kill assay), in order to determine if a time-dependent effect would be reached.

Staphylococcal biofilm formations were overall affected by the presence of NAC, a clear dose-dependent inhibitory effect on *S. aureus* biofilm formation was observed with all the four strains that gave an adequate biofilm growth in the MBEC High-Throughput Assay: *S. aureus* ATCC 6538, *S. aureus* ATCC 25923, *S. aureus* Z59, and *S. aureus* Z60 (Figure 7a). The Δlog CFU/peg, compared to control, ranged from 2.5 to 0.6 log CFU/peg and from 2.7 to 0.7 log CFU/peg at NAC 8 mg/ml and NAC 16 mg/ml, respectively (Figure 7a). The effect of NAC in inhibiting biofilm formation of the two remaining *S. aureus* isolates (i.e. *S. aureus* MRSA-IT1 and *S. aureus* ATCC 43300) was tested using flat-bottom microtiter plates. Unlike promising previous results, NAC did not affect the biofilm forming capability of these methicillin resistant isolates (Figure 7b). These heterogeneous results might not be associated to the anti-biofilm activity of NAC *per se*, but being possibly related to the different stage of biofilm formation evaluated in the different models (i.e. VCC much higher in non-treated biofilm grown in flat-bottom compared to those in Calgary Biofilm Device). For sure, it would be interesting evaluate the biofilm formation kinetics, in presence of different NAC concentrations at different stages of biofilm growth. On the other hand, no effect was exerted against mature biofilms of all the *S. aureus* evaluated, even at the highest concentration tested (i.e. 32 mg/ml) (Figure 7c). Further studies would be aimed to investigate the NAC activity against early staphylococcal biofilms.

Promising results were obtained in preventing biofilm formation of *S. maltophilia* and BCC (i.e. species more susceptible to NAC activity compared to the previous ones). Significantly reduction of number of viable sessile cells were determined for all the *S. maltophilia* clinical isolates in presence of NAC in a dose-dependent manner both at MIC and at sub-MIC concentrations (i.e. 4 mg/ml, 8 mg/ml, and 16 mg/ml) (Figure 8a). The Δlog CFU/peg, compared to control, ranged from 0.8 to 3.9 log CFU/peg and from 2.5 to 6.3 log CFU/peg at NAC 8 mg/ml and NAC 16 mg/ml, respectively (Figure 8a). Otherwise, the activity of NAC against the BCC biofilms were strain-dependent, three BCC isolates showed a dose-dependent susceptibility (i.e. with at least 1.3 log CFU/peg reduction at NAC 16 mg/ml – Figure 8b), meanwhile no effect were demonstrated against the remaining two isolates, one of those exhibited a trend toward an increasing number of viable cells at 16 mg/ml of NAC (Figure 8b). Results obtained are strongly correlated with the activity of NAC on planktonic cells (i.e. biofilms more affected are the same for which NAC demonstrated slowdown of planktonic cells growth at sub-MICs). It would be interesting investigate this possible relationship through increasing the number of strains tested and by evaluating the effect of NAC in biofilm grown for longer time (i.e. biofilm growth curve). In conclusion, these original data suggested that NAC could play a role in the prevention of biofilm formation of *S. maltophilia* and BCC clinical isolates. Since NAC has already been used in clinical practices, proofs obtained should encourage the NAC employment in the management of respiratory tract infections.

Table 3. Origin and main features of the 21 strains included in the study.

Strain	Origin and main features	NAC MIC [mg/ml]
P. aeruginosa PAO-1	*P. aeruginosa* reference strain [Stover CK, 2000]	>16
P. aeruginosa Z29	Lower respiratory tract infection, XDR clinical isolate	>16
P. aeruginosa Z32	Lower respiratory tract infection, MDR clinical isolate	>16
P. aeruginosa Z33	Cystic fibrosis (2-year lung colonization), MDR clinical isolate	16
P. aeruginosa Z34	Cystic fibrosis (3-year lung colonization), MDR clinical isolate	>16
P. aeruginosa Z38	Acute bacterial rhinosinusitis clinical isolate	>16
S. aureus ATCC 6538	ATCC reference MSSA strain	>16
S. aureus ATCC 25923	ATCC reference MSSA strain	>16
S. aureus ATCC 43300	ATCC reference MRSA strain	>16
S. aureus MRSA-IT1	Bloodstream infection, MRSA, hVISA [Landini G, 2015]	>16
S. aureus Z59	Community-acquired pneumonia, MRSA clinical isolate	>16
S. aureus Z60	Community-acquired pneumonia, MRSA clinical isolate	>16
S. maltophilia Z120	Lower respiratory tract infection clinical isolate	16
S. maltophilia Z128	Lower respiratory tract infection clinical isolate	16
S. maltophilia Z129	Lower respiratory tract infection clinical isolate	16
S. maltophilia Z133	Lower respiratory tract infection clinical isolate	32
B. multivorans genomovar II Z136	Cystic fibrosis, clinical isolate	32
B. seminalis BCC7 Z138	Cystic fibrosis, clinical isolate	16
B. cenocepacia genomovar IIIA Z142	Cystic fibrosis, clinical isolate	16
B. stabilis genomovar IV Z145	Cystic fibrosis, clinical isolate	16
B. cepacia complex Z148	Clinical isolates	16

When available, main features concerning resistance determinants were reported. ATCC, American Type Culture Collection; MDR, multidrug resistant isolates exhibiting a resistance phenotype including aminoglycosides, fluoroquinolones, and beta-lactams (excluding carbapenems); XDR, extensively drug resistant isolates exhibiting a resistance phenotype including aminoglycosides, fluoroquinolones, and beta-lactams (including also carbapenems); MSSA, methicillin-susceptible *S. aureus*; MRSA, methicillin-resistant *S. aureus*; hVISA, heterogeneous vancomycin-intermediate *S. aureus*; BCC, *Burkholderia cepacia* complex.

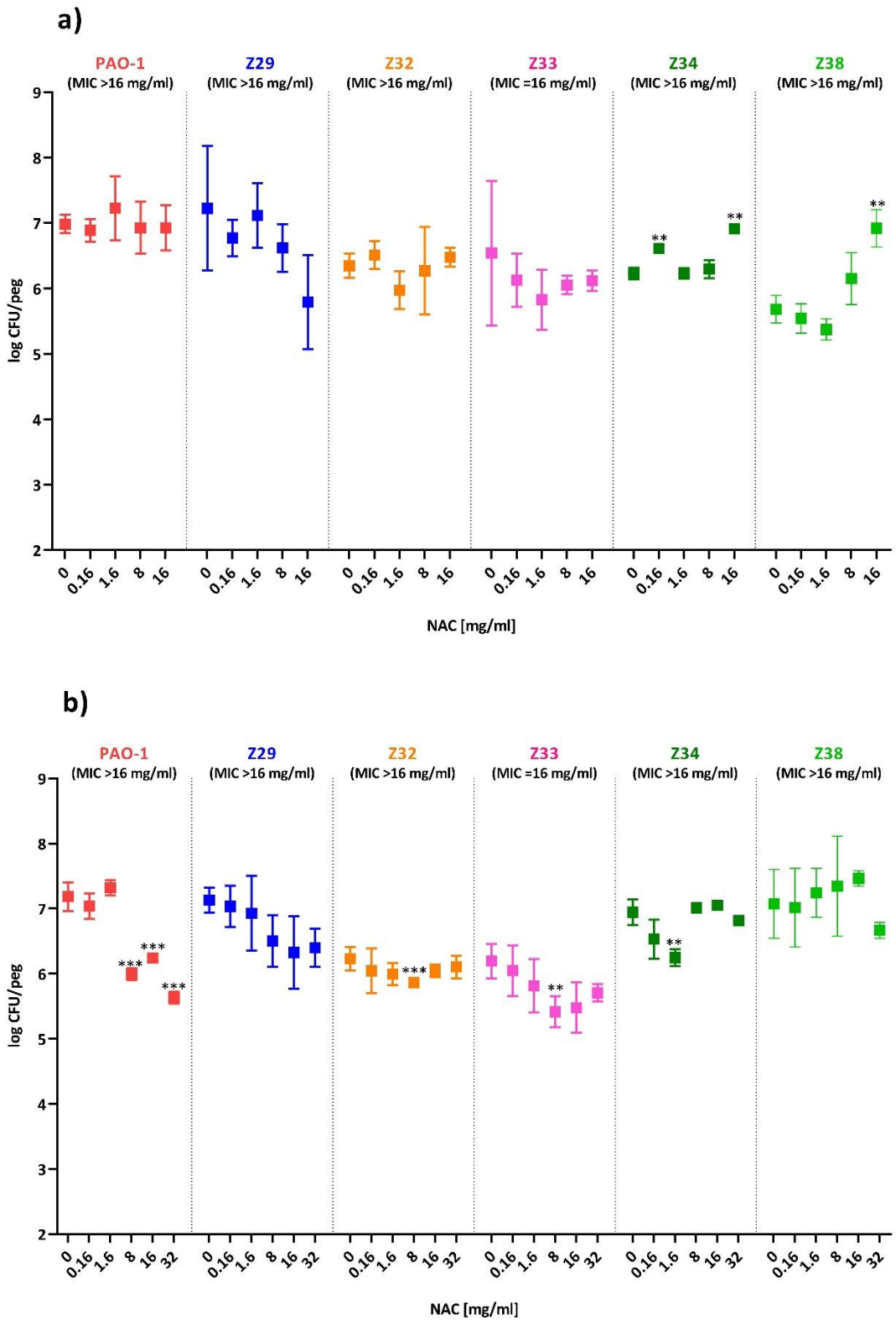

Figure 6. *N*-acetylcysteine alone in inhibiting biofilms formation (a), and eradicating mature biofilm (b) of six *P. aeruginosa* clinical isolates. (a) Biofilms were grown in presence or absence of NAC for three days in daily refreshed medium; (b) three-days-old mature biofilms were challenged for additional 24 hours with NAC. NAC concentrations ranging from 16 to 0.16 mg/ml, including 32 mg/ml for the treatment of mature biofilms. The *x*-axis is set at the limit of detection; ** *p* value ≤ 0.01; *** *p* value ≤ 0.001.

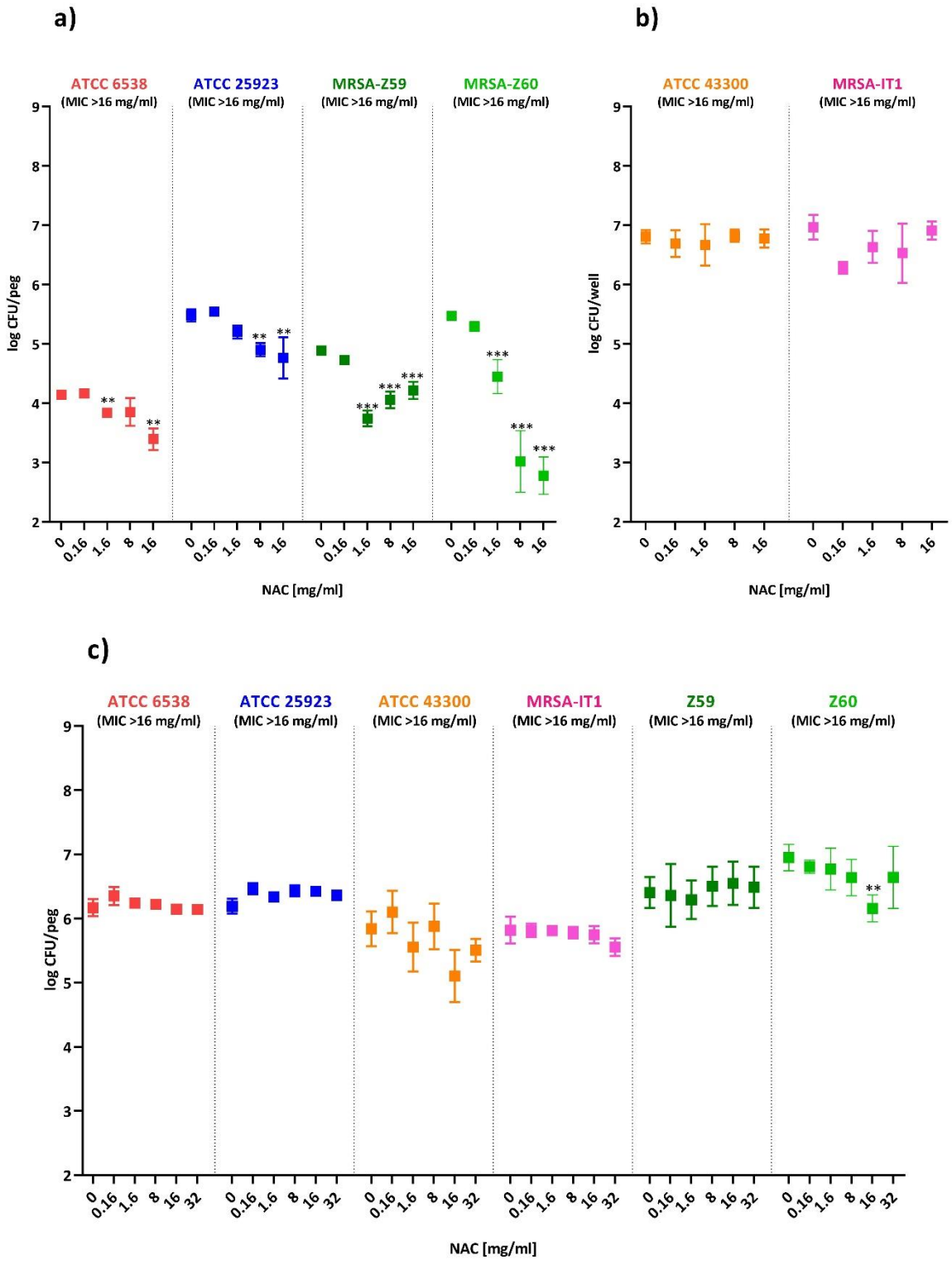

Figure 7. *N*-acetylcysteine alone in inhibiting biofilms formation (a-b), and eradicating mature biofilm (c) of six *S. aureus* clinical isolates. (a) Biofilms were grown in presence or absence of NAC for 24 hours in MBEC High-Throughput Assay; (b) Biofilms were grown in presence or absence of NAC for 24 hours in flat-bottom microtiter plate; (c) six-days-old mature biofilms were challenged for additional 24 hours with NAC. NAC concentrations ranging from 16 to 0.16 mg/ml, including 32 mg/ml for the treatment of mature biofilms. The *x*-axis is set at the limit of detection; ** *p* value ≤ 0.01; *** *p* value ≤ 0.001.

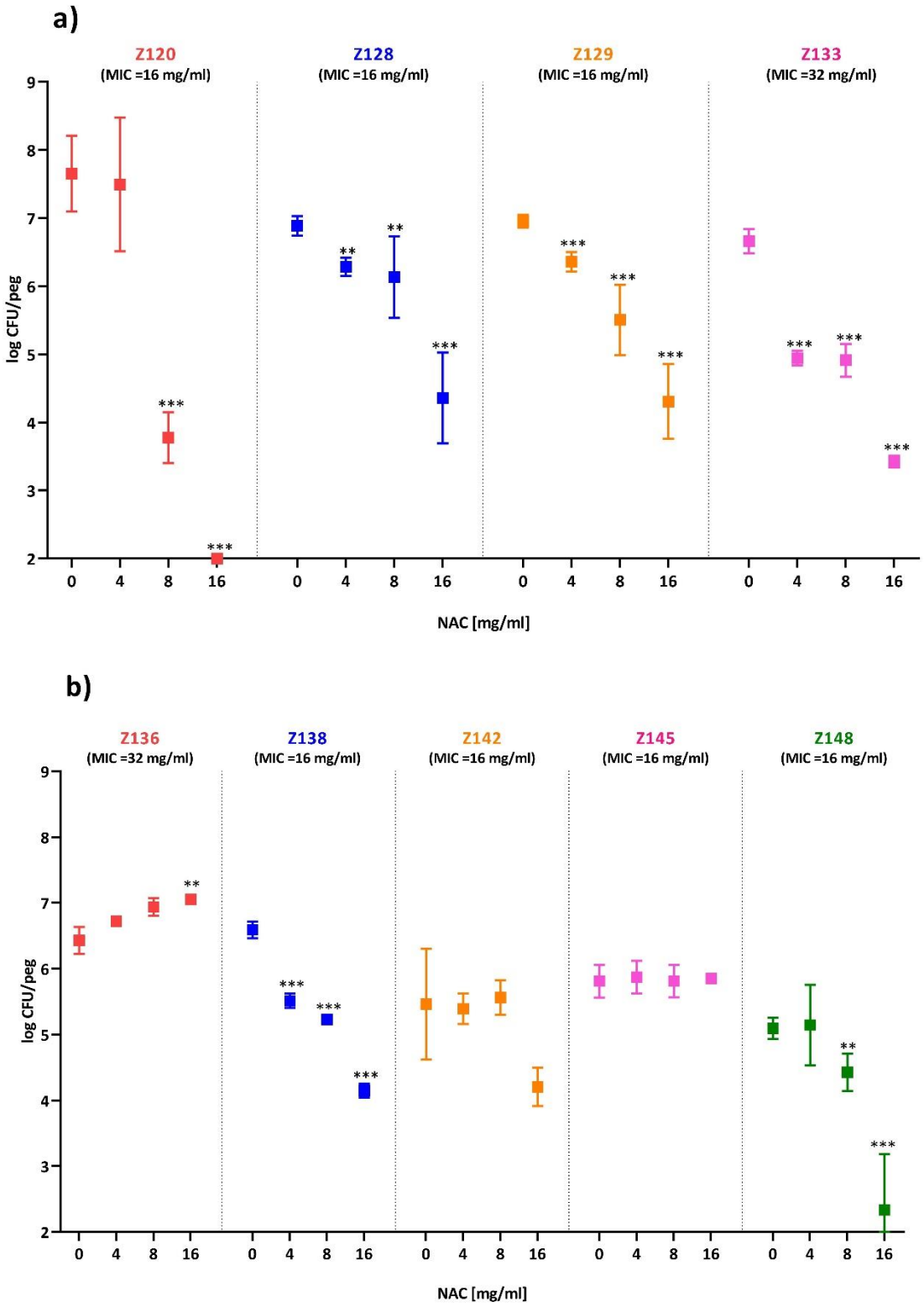

Figure 8. *N*-acetylcysteine alone in inhibiting biofilms formation of four *S. maltophilia* clinical isolates (a), and five *B. cepacia* complex clinical isolates (b). Biofilms of *S. maltophilia* and *B. cepacia* complex were grown in presence or absence of 4, 8 and 16 mg/ml of NAC for 24 and 48 hours, respectively. The *x*-axis is set at the limit of detection; ** *p* value ≤ 0.01; *** *p* value ≤ 0.001.

- **Effect of high *N*-acetylcysteine concentrations on antibiotic activity against a large collection of respiratory pathogens**

The noteworthy lack of consistent data regarding the potential modulatory effect of NAC on antibiotic activity is a matter of concern [Alfredsson H, 1987; Goswami M, 2010; Parry MF, 1977; Rodríguez-Beltrán J, 2015; Yang F, 2016]. In particular, discordant results were recently reported in two independent studies which investigated the effect of 10 mM NAC (i.e. 1.6 mg/ml, a rather high concentration achievable by topical administration [Szkudlarek U, 2004]) on the activity of some antibiotics against few Gram negative pathogens (including *E. coli*, *Klebsiella* spp., *P. aeruginosa*, and *A. baumannii*). Indeed, the modulatory effect observed by Goswami *et al.* in 2010 (i.e. synergism with ampicillin; antagonism with fluoroquinolones, aminoglycosides and macrolides) [Goswami M, 2010] was not confirmed in a more recent study by Rodríguez-Beltrán *et al.* [Rodríguez-Beltrán J, 2015], who demonstrated that the modulation of activity of fluoroquinolones and aminoglycosides was actually related to the low pH of pure NAC powder solutions and not to NAC by itself, suggesting that pH related issues had likely contributed to the inconsistency of data from previous studies. In their work, Rodríguez-Beltrán *et al.* found that only the activity of imipenem was significantly affected by NAC, and proposed that for *P. aeruginosa* this antagonism was due to competitive inhibition of imipenem uptake through OprD by NAC [Rodríguez-Beltrán J, 2015].

Considering the relevance of a potential antagonistic effect of NAC with antibiotic activity, especially in case of long-term high-dosage topical administration (as should be the case for chronic respiratory diseases [Blasi F, 2016]), the evaluation of the effect of high *N*-acetylcysteine concentrations on antibiotic activity against a large collection of respiratory pathogens was carried out.

The effect of 10 mM NAC, and 50 mM NAC (i.e. 1.6 and 8 mg/ml representing the concentration tested in previous studies and a 5-fold higher concentration, respectively) on antibiotic susceptibility of 40 reference and clinical isolates of respiratory pathogens (i.e. *E. coli, Klebsiella* spp.*, E. cloacae, P. aeruginosa, A. baumannii, M. catarrhalis, H. influenzae, S. aureus, S. pyogenes, S. pneumoniae,* and *C. striatum*) were evaluated (Table 4). Minimal Inhibitory Concentrations (MICs) of the most relevant therapeutic options for the different respiratory pathogens were determined by broth microdilution [CLSI M07-A10, 2015], in the absence or presence of the two selected NAC concentrations. The MICs of NAC were >16 mg/ml for all tested strains, except for the two *H. influenzae* strains which showed MICs of 16 mg/ml. In the presence of either 10 or 50 mM of NAC, the MICs of most antibiotics remained within a single $\log_2$ dilution difference (i.e. the commonly accepted range of experimental reproducibility), with the notable exception of carbapenems

(Figure 9). Indeed, a clear dose-dependent inhibition of carbapenem activity by NAC was observed with all tested isolates, with imipenem being the most affected drug compared to meropenem and ertapenem (i.e. the activity of the two last carbapenems was overall preserved at 10 mM NAC) (Figure 9). With other antibiotics, 10 mM NAC had no major effects, while 50 mM NAC sporadically decreased (ceftriaxone and aminoglycosides) or increased (penicillins) antibiotic activity (Figure 9). Time-kill assays confirmed a dose-dependent inhibition by NAC of the bactericidal activity of imipenem against the reference strain *E. coli* ATCC 25922 (Figure 10).

Moreover, carbapenems stability were consistently affected in PBS or in CAMHB in the presence of 10 or 50 mM NAC (Table 5). Notably, imipenem was less stable than meropenem or ertapenem in all tested conditions (Table 5). Temperature and medium impacted on NAC-mediated carbapenem inactivation, with a more rapid inactivation observed at 37 °C *vs.* 25 °C, and in CAMHB *vs.* PBS (Table 5). Overall, these data were consistent with the impact of NAC on carbapenem MIC values (Figure 9).

In conclusion, results demonstrated that high NAC concentrations (possibly reached in the airways following topical administration) overall do not interfere with the activity of the most commonly used antibiotics, with the exception of carbapenems. However, considering that the MICs of meropenem and ertapenem for susceptible strains mostly remained below the susceptibility breakpoints even in the presence of 50 mM NAC, the negative interaction of NAC with these drugs might not be clinically relevant and warrants further evaluation. Some modulatory effect on the activity of other beta-lactams and aminoglycosides was also observed at the highest NAC concentration tested with some strains, resulting in either a synergistic or antagonistic interaction.

Table 4. Origin and main features of the 40 strains included in the study.

Strain	Origin and main features
E. coli ATCC 25922	ATCC reference strain
E. coli Z21	Cystic fibrosis (2-year lung colonization), ESBL-positive, ST131 clinical isolate
E. coli Z24	Cystic fibrosis clinical isolate
E. coli Z25	Low respiratory tract infection, ESBL-positive, KPC-positive clinical isolates
K. pneumoniae ATCC 700603	ATCC ESBL-positive reference strain
K. pneumoniae NTUH-K2044	Liver abscess and meningitis, capsular serotype K1, hypermucoviscous [Wu KM, 2009]
K. pneumoniae CIP 52.145	CIP reference strain, capsular serotype K2, hypermucoviscous
K. pneumoniae Z4	Cystic fibrosis (1-year lung colonization), ESBL-positive, AmpC-positive clinical isolate
K. pneumoniae Z11	Low respiratory tract infection, KPC-positive clinical isolate
K. oxytoca CCUG 15717^{T}	CCUG type strain
E. cloacae CIP 6085^{T}	CIP type strain
E. cloacae Z16	Cystic fibrosis, ESBL-positive clinical isolates
E. cloacae Z17	Lower respiratory tract infection clinical isolate
E. cloacae Z18	Lower respiratory tract infection clinical isolate
E. cloacae Z19	Lower respiratory tract infection clinical isolate
P. aeruginosa ATCC 27853	ATCC reference strain
P. aeruginosa PAO-1	*P. aeruginosa* reference strain [Stover CK, 2000]
P. aeruginosa Z32	Lower respiratory tract infection clinical isolate
P. aeruginosa Z34	Cystic fibrosis (3-year lung colonization) clinical isolate
P. aeruginosa Z38	Acute bacterial rhinosinusitis clinical isolate
A. baumannii ATCC 17978	ATCC reference strain
A. baumannii RUH 134	Reference strain for the global clone 2 [Diancourt L, 2010]
M. catarrhalis Z72	Lower respiratory tract infection clinical isolate
M. catarrhalis Z73	Lower respiratory tract infection clinical isolate
H. influenzae ATCC 49247	ATCC reference strain
H. influenzae Z83	Lower respiratory tract infection clinical isolate
S. aureus ATCC 25923	ATCC reference MSSA strain
S. aureus ATCC 6538	ATCC reference MSSA strain
S. aureus ATCC 43300	ATCC reference MRSA strain
S. aureus MRSA-IT1	Bloodstream infection, MRSA, hVISA [Landini G, 2015]
S. aureus Z57	Acute bacterial rhinosinusitis, MSSA clinical isolate
S. aureus Z61	Community-acquired pneumonia, MSSA clinical isolate
S. pyogenes ATCC 12344^{T}	ATCC type strain
S. pyogenes Z90	Lower respiratory tract infection clinical isolate
S. pyogenes Z91	Cellulitis clinical isolate
S. pneumoniae ATCC 49619	ATCC reference strain
S. pneumoniae Z104	Lower respiratory tract infection clinical isolate
S. pneumoniae Z105	Lower respiratory tract infection clinical isolate
C. striatum Z114	Lower respiratory tract infection clinical isolate
C. striatum Z115	Lower respiratory tract infection clinical isolate

When available, main features concerning resistance determinants and molecular typing were reported. ATCC, American Type Culture Collection; CIP, Collection Institute Pasteur; CCUG, Culture Collection University of Goteborg; ESBL, extended-spectrum beta-lactamase; KPC, KPC type beta-lactamase; AmpC, AmpC-like beta lactamase; MSSA, methicillin-susceptible *S. aureus*; MRSA, methicillin-resistant *S. aureus*; hVISA, heterogeneous vancomycin-intermediate *S. aureus*.

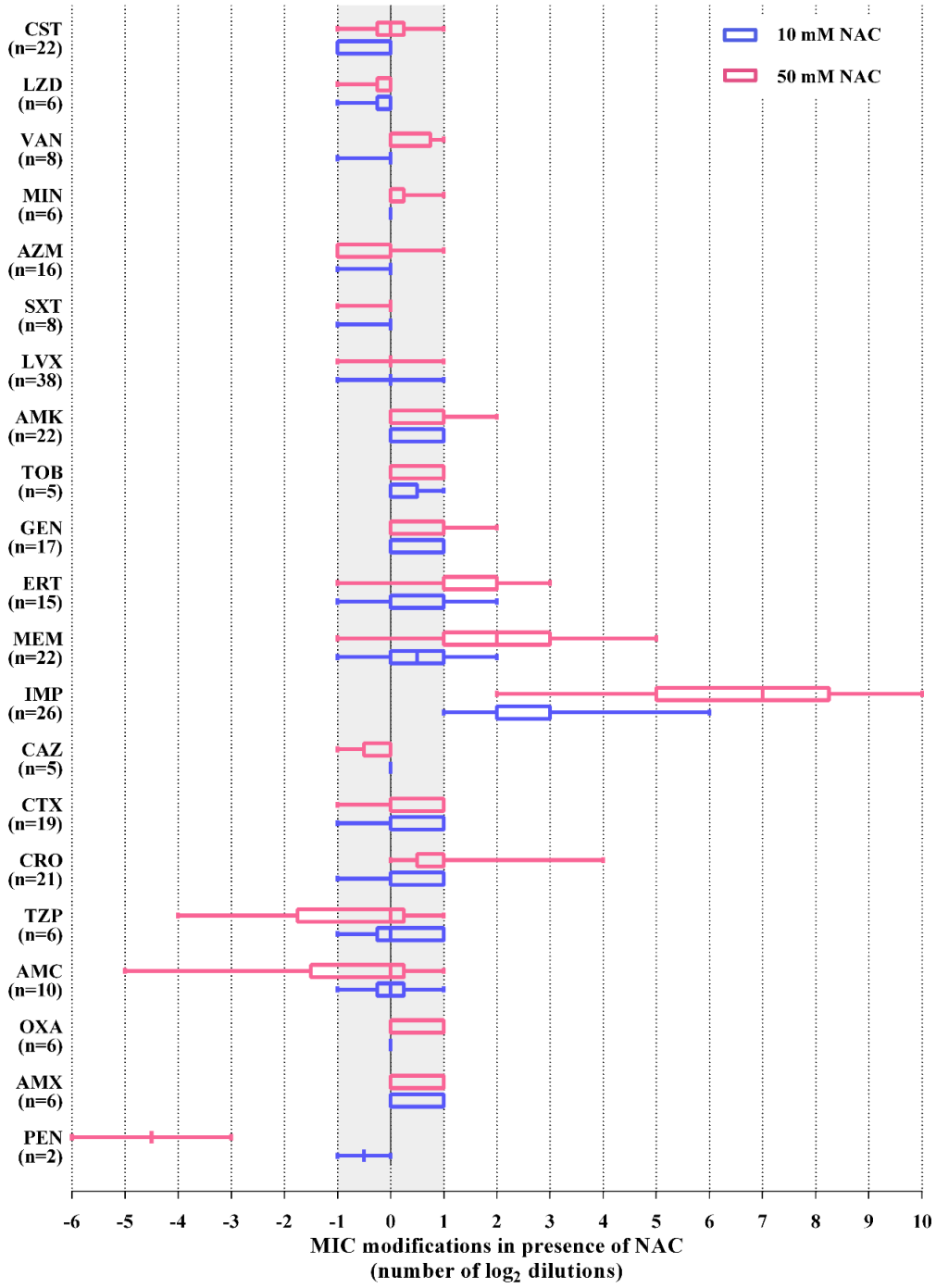

Figure 9. Schematic representation of the effect of two high NAC concentrations (10 mM and 50 mM) on antibiotic activity against a collection of respiratory pathogens. A modulatory effect on antibiotic activity was defined as a MIC modification of at least 2 $\log_2$ dilutions. The number of strains tested for each antibiotic is indicated in brackets. In order to express the results as $\log_2$ dilution variations, a value corresponding to the lowest or to twice that of the highest antibiotic concertation tested was assigned to MICs that could not be determined because of out of range of antibiotic concentrations used. This is particularly relevant for MICs of imipenem in the presence of 50 mM NAC, which was >64 µg/ml for the majority of isolates tested. PEN, penicillin; AMX, amoxicillin; OXA, oxacillin; AMC, amoxicillin clavulanic acid; TZP, piperacillin-tazobactam; CRO, ceftriaxone; CTX, cefotaxime; CAZ, ceftazidime; IMP, imipenem; MEM, meropenem; ERT, ertapenem; GEN, gentamicin; AMK, amikacin; TOB, tobramycin; LVX, levofloxacin; SXT, trimethoprim-sulfamethoxazole; AZM, azithromycin; MIN, minocycline; VAN, vancomycin; LZD, linezolid; CST, colistin. The box-and-whiskers plot (i.e. box extended from 25th to 75th percentiles, and whiskers indicating the minimum and maximum values) was generated by GraphPad Prism 5 (GraphPad, La Jolla, CA).

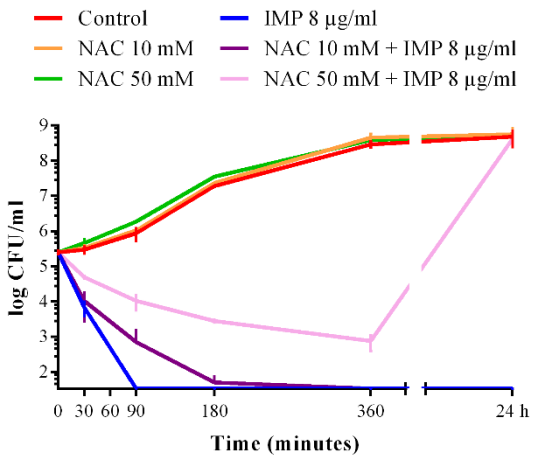

Figure 10. Time-kill curves of imipenem (8 µg/ml) alone and in combination with 10 and 50 mM NAC against *E. coli* ATCC 25922. The *x* axis has been set at the experimental detection limit (1.5 log CFU/ml).

Table 5. Stability of carbapenems in the presence of NAC.

Compound (experimental conditions)	Antibiotic $t_{1/2}$ (min)		
	Imipenem	Meropenem	Ertapenem
None (PBS, 25°C)	>1000	>1000	>1000
10 mM NAC (PBS, 25°C)	580 ± 9	>1000	>1000
50 mM NAC (PBS, 25°C)	160 ± 2	500 ± 8	>1000
None (PBS, 37°C)	>1000	>1000	>1000
10 mM NAC (PBS, 37°C)	550 ± 30	>1000	>1000
50 mM NAC (PBS, 37°C)	66 ± 5	220 ± 30	530 ± 40
None (CAMHB, 37°C)	>1000	>1000	>1000
10 mM NAC (CAMHB, 37°C)	200 ± 40	670 ± 160	>1000
50 mM NAC (CAMHB, 37°C)	52 ± 6	145 ± 15	225 ± 20

The half-life ($t_{1/2}$) of antibiotics was computed from the pseudo-first order rate constant for carbapenem beta-lactam ring opening, measured by following the time-dependence variation of absorbance at 300 nm (values are the mean of four independent experiments), followed in both PBS buffer and in cation-adjusted Mueller-Hinton Broth (CAMHB) and at 25 or 37 °C.

3

Highly antimicrobial nanoparticle films obtained by supersonic cluster beam engineering

Related Publications:

- Cavaliere E, De Cesari S, Landini G, Riccobono E, Pallecchi L, Rossolini GM, and Gavioli L. 2015. Highly bactericidal Ag nanoparticle films obtained by cluster beam deposition. *Nanomedicine: Nanotechnology, Biology and Medicine*, 11(6), 1417-1423.

- Benetti G, Cavaliere E, Canteri A, Landini G, Rossolini GM, Pallecchi L, Chiodi M, Van Bael MJ, Winckelmans N, Bals S, Gavioli L. 2016. Direct synthesis of antimicrobial coatings based on tailored bi-elemental nanoparticles. *Nanomedicine: Nanotechnology, Biology and Medicine*. Under submission.

Contamination of environmental surfaces with microbial pathogens has been recognized as a major vehicle for transmission of several key healthcare-associated pathogens [Humphreys H, 2014; Quinn MM, 2015]. The hospital surfaces closest to patients are the most heavily contaminated (bed rails, nurse call buttons, bedside/overbed tables), but the range of surfaces involved in the pathogens dissemination is wide (sinks, doors, towel dispensers) [Oberauner L, 2013]. In fact, the risk of acquiring a nosocomial pathogen by a single room occupant is significantly increased if the previous occupant was infected or colonized [Quinn MM, 2015; Weber DJ, 2010; Otter JA, 2011]. In this perspective, reduction of microbial load in hospital surfaces through a rigorous environmental cleaning procedures and the employment of antimicrobial surfaces are being crucial to implement effective control measures to reduce healthcare-associated infections (HAIs) [Quinn MM, 2015; Weber DJ, 2013]. Nanoparticles coatings were being exploited as a powerful weapon against the indirect transmission of nosocomial pathogens, among the large number of nanoparticles investigated so far for antimicrobial coatings, silver nanoparticles (Ag NPs) have been considered the most promising ones for potential medical applications [Seil JT, 2012]. To date, the synthesis of Ag NPs is largely based on wet chemical reduction methods which allow a great control over size and shape of the Ag NPs but pose several problems such as the use of colloidal stabilizers, the presence of impurities [Cavaliere E, 2015]. Moreover, the mere synthesis of the Ag NPs does not imply a good adhesion of the obtained NPs to the substrate of need.

The purpose of this project was to evaluate the antimicrobial effect of characterized NPs films, synthesized by a supersonic cluster source (SCBD), which produces NPs without chemical synthesis

and generates monolayers stable and well bonded to substrate. First of all, we determined the antimicrobial effect of pure Ag NPs coating deposited on microscope slide against a wide panel of clinically relevant microorganisms (Table 6), representative of both Gram negative and Gram positive bacteria, and yeasts. Then we scaled up to the application and deepened the bactericidal activity of bi-metal nanoparticles (i.e. 50% of silver and 50% of titanium nanoparticles – AgTi5050) on commercial chrome-plated supports against a selection of 6 clinical isolates (Table 6).

Table 6. Main features of clinical isolates included in the study.

Strain	Mean features
Gram negatives	
Escherichia coli ATCC 25922 [a]	Reference strain
Escherichia coli CVB-1	XDR clinical isolate producing the carbapenemase NDM-1 [D'Andrea MM, 2011]
Klebsiella pneumoniae FIPP-1	XDR epidemic ST258 clone producing the carbapenemase KPC-3 [Giani T, 2009]
Klebsiella pneumoniae KKBO-4	XDR epidemic ST258 clone producing the carbapenemase KPC-3 and resistant also to colistin [Cannatelli A, 2013]
Pseudomonas aeruginosa PAO-1 [a]	Reference strain
Pseudomonas aeruginosa VR-143/97	XDR epidemic clone producing the carbapenemase VIM-1 [Riccio ML, 2005]
Pseudomonas aeruginosa Z33 [a]	MDR isolate from persistent cystic fibrosis 2-year lung colonization
Acinetobacter baumannii ATCC 17978	Reference strain
Acinetobacter baumannii RUH 134	Reference strain for the global clone 2 [Diancourt L, 2010]
Acinetobacter baumannii AB06C13 [a]	XDR clinical isolate belonging to global clone 2 and producing the carbapenemases OXA-23 and OXA-58 [Principe L, 2014]
Gram positives	
Staphylococcus aureus ATCC 6538	Reference strain
Staphylococcus aureus MRSA-IT16	Methicillin-resistant clinical isolate from biofilm-associated infection [Landini G, 2015]
Staphylococcus aureus MRSA-IT1 [a]	Methicillin-resistant clinical isolate from biofilm-associated infection and exhibiting hVISA and daptomycin resistance phenotype [Landini G, 2015]
Enterococcus faecalis ATCC 29212 [a]	Reference strain
Enterococcus faecium FI2013	Glycopeptides-resistant isolate from bloodstream infection
Yeasts	
Candida albicans ATCC 10231	Reference strain
Candida albicans EMO1303	Clinical isolate from bloodstream infection

MDR, multidrug resistant isolates exhibiting a resistance phenotype including aminoglycosides, fluoroquinolones, and beta-lactams (excluding carbapenems); XDR, extensively drug resistant isolates exhibiting a resistance phenotype including aminoglycosides, fluoroquinolones, and beta-lactams (including also carbapenems); hVISA, heterogeneous vancomycin-intermediate *Staphylococcus aureus*.

[a] strains selected to evaluate the antimicrobial activity of bi-metal nanoparticles (AgTi5050).

- **Highly antimicrobial Ag nanoparticle films obtained by supersonic cluster beam deposition**

The antimicrobial activity of pure Ag NPs on microscope slides was evaluated against a wide panel of clinically relevant microorganisms (Table 6). The Microbicidal Effect (i.e. ME = $\log N_C$ - $\log N_E$; where N_C and N_E represented the number of CFU obtained with control slides and slides coated of Ag NPs, respectively) were determined after 24 hours of incubation at 25°C in damp environment [Pallavicini P, 2010]. Ag NP films were found to exert a broad-spectrum bactericidal activity. In particular, after 24 hours of exposure to Ag NP films, a reduction of viable bacterial loads by more than 3 log (compared to controls) was observed with 10 of the 14 bacterial strains tested, including representatives of both Gram positive and Gram negative pathogenic species (Figure 11). Members of the family *Enterobacteriaceae*, showed a consistently very high susceptibility to Ag NP films (i.e. ME >5) (Table 7). Interestingly, Ag NP films could almost completely sterilize a high inoculum of extensively drug-resistant clinical strains producing two of the most worrisome resistance mechanisms recently emerged in enterobacteria and capable of pandemic dissemination, such as the carbapenemases NDM-type and KPC-type. An overall strong bactericidal activity (i.e. ME range >5.7 – 2.6) was also demonstrated with reference and clinical strains of *P. aeruginosa* and *A. baumannii*, including representative of extensively drug-resistant high-risk clones (Table 7). Those microorganisms are major opportunistic pathogens in the hospital setting, with a high propensity to evolve extensively drug-resistance and even totally drug-resistance phenotypes and to survive for long periods in the hospital environment (accounting for the occurrence of nosocomial epidemics through, for example, contaminated taps, sinks or even antiseptic solutions). The finding of a lower susceptibility to Ag NP films of the clinical *P. aeruginosa* VR-143/97 strain compared to the other four Gram negative non-fermenters tested, could suggest that this extensively drug-resistant strain might have evolved some resistance mechanism also to Ag NP (e.g. by chromosomal mutations or horizontal gene transfer). Concerning Gram positive bacteria, high susceptibility to Ag NP films was demonstrated with 2 of the 3 *S. aureus* tested (ME >3), including a reference strain and a methicillin-resistant strain isolated from a biofilm-related infection (i.e. naive valve endocarditis) (Table 7). The *S. aureus* MRSA-IT1 exhibiting a reduced susceptibility to Ag NP (i.e. ME = 2), besides being isolated from a biofilm-associated infection (i.e. post-surgical wound infection), was characterized by a very rare and worrisome resistance phenotype extended also to daptomycin (one of the most recent antibiotic class entered the clinical practice). It could be hypothesized that the overall reduction of anionic surface charge that has been associated to daptomycin resistance in *S. aureus* might have contributed to the reduced susceptibility to Ag NP, by impairing the interaction with the positively charged silver ions, a fact that would worth further investigation. Finally, *Enterococcus* spp. strains exhibited a relatively low susceptibility to Ag NP films (ME range 0.9 - 1.7), as well as the two *C. albicans* strains (ME range 0.7 - 1) (Table 7). The poor activity of Ag

NP against the latter microorganisms is an intriguing phenomenon, and the reasons accounting for this will deserve further attention.

In conclusion we have demonstrated the realization of a uniform Ag NP film with extremely controlled thickness and NP size directly on a substrate surface through a simple and scalable technique, SCBD. We have proven that such films present a relevant and broad-spectrum bactericidal activity.

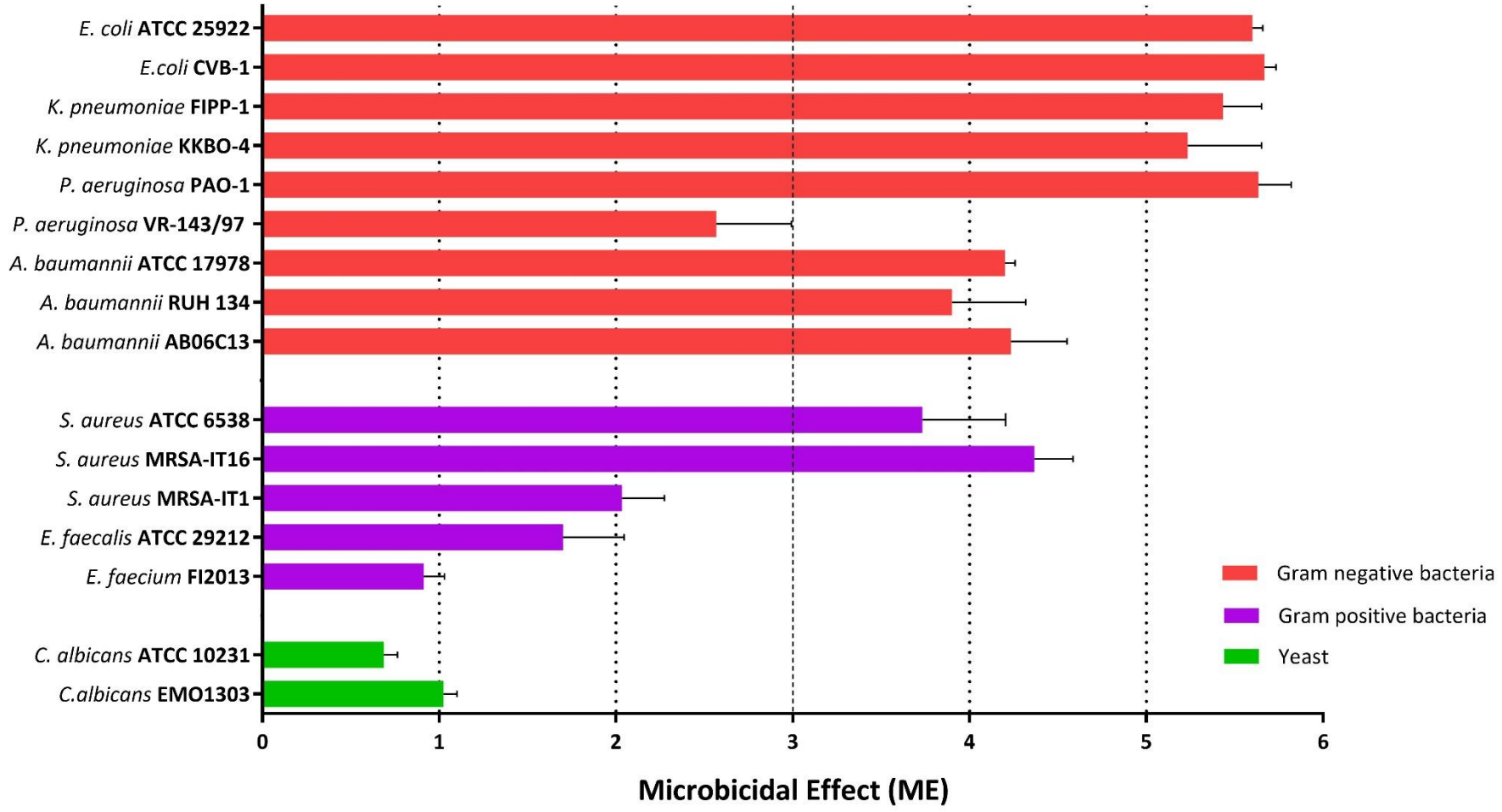

Figure 11. The microbicidal effect of Ag NP films calculated as log reduction of viable cells compared to control, after 24 hours of exposure. ME over 3 corresponds to a reduction of viable bacterial loads by more than 3 log (i.e. bactericidal activity).

Table 7. Microbicidal Effect (ME) of Ag NP films against clinically relevant microorganisms after 24 hours of exposure.

Strain	$logN_C$ [CFU ± SD]	$logN_E$ [CFU ± SD]	ME [$logN_C$ - $logN_E$]
Gram negatives			
Escherichia coli ATCC 25922	7.2 ± 0.1	1.6 ± 0.0▼	≥ 5.6 ± 0.1
Escherichia coli CVB-1	7.3 ± 0.1	1.6 ± 0.0▼	≥ 5.7 ± 0.1
Klebsiella pneumoniae FIPP-1	7.3 ± 0.1	1.9 ± 0.4►	5.4 ± 0.4
Klebsiella pneumoniae KKBO-4	7.3 ± 0.0	2.0 ± 0.7►	5.2 ± 0.7
Pseudomonas aeruginosa PAO-1	7.3 ± 0.3	1.6 ± 0.0▼	≥ 5.7 ± 0.3
Pseudomonas aeruginosa VR-143/97	5.4 ± 0.4	2.8 ± 1.0▲	2.6 ± 0.8
Acinetobacter baumannii ATCC 17978	6.9 ± 0.1	2.7 ± 0.1	4.2 ± 0.1
Acinetobacter baumannii RUH 134	6.0 ± 0.1	2.1 ± 0.7▲	3.9 ± 0.7
Acinetobacter baumannii AB06C13	6.1 ± 0.1	1.9 ± 0.5►	4.2 ± 0.5
Gram positives			
Staphylococcus aureus ATCC 6538	6.5 ± 0.1	2.8 ± 0.9	3.7 ± 0.8
Staphylococcus aureus MRSA-IT16	6.0 ± 0.4	1.6 ± 0.0►	4.4 ± 0.4
Staphylococcus aureus MRSA-IT1	6.8 ± 0.0	4.8 ± 0.4	2.0 ± 0.4
Enterococcus faecalis ATCC 29212	6.1 ± 0.0	4.4 ± 0.6	1.7 ± 0.6
Enterococcus faecium FI2013	6.1 ± 0.0	5.1 ± 0.2	0.9 ± 0.2
Yeasts			
Candida albicans ATCC 10231	6.2 ± 0.0	5.5 ± 0.2	0.7 ± 0.1
Candida albicans EMO1303	6.0 ± 0.1	5.1 ± 0.1	1.0 ± 0.1

CFU, colony forming unit; SD, standard deviation; N_C, CFU obtained with the control slide (average of three independent experiments); N_E, CFU obtained with the Ag NP films (average of three independent experiments). The detection limit of viable cells count was 4.2 x 10^1 CFU. When after Ag NPs challenge no viable cells were counted in one (▲), two (►) or three (▼) independent experiments, the arbitrary value of 4.2 x 10^1 CFU (representing the detection limit) was used for calculating N_E and ME.

- **Antibacterial activity of bi-element nanoparticle films (AgTi5050) obtained by supersonic cluster beam deposition**

Bi-metal NP AgTi5050 were found stable and strongly bonded to commercial chrome-plated supports. To verify the bactericidal activity AgTi5050, we incubated a standardized bacteria suspension of 6 selected strains at 25°C in dark and damp environment for 3 hours (extended to 24 hours for Gram positive strains, and including additional measurements at 15, 45 and 90 minutes for the *A. baumannii* strain) (Table 6). We performed the antimicrobial activity test in dark environment in order to evaluate the microbicidal effect of Ag NP and to avoid the photo-activation of Ti NP (i.e. exploiting just the stabilizer proprieties of titanium). AgTi5050 film was found to be extremely effective against all the Gram negative bacterial pathogens tested, being able to almost completely sterilize a high bacterial inoculum, in 3 hours (Figure 12a). Shorter exposure times were tested against the extensively drug resistant *A. baumannii* AB06C13, and revealed a detectable decrease of viable cells already after 15 minutes of exposure, with a bactericidal effect (i.e. usually defined as a 3 log reduction of viable cell count) achieved in 90 minutes (Figure 12b). Considering that environmental surfaces are thought to be contaminated with a much lower bacterial inoculum [Otter JA, 2011] than that used in the present study, and the very low quantity of Ag present in this coating, our results are extremely promising and suggest that AgTi5050 NP coatings could represent highly effective antimicrobial surfaces for limiting the indirect transmission of Gram negative pathogens. An overall lower and slower bactericidal activity was instead observed against the two Gram positive strains tested (Table 6). In particular, while a sizable reduction of viable cells was obtained with the *S. aureus* strain after a longer exposition time on the AgTi5050 NP films, the *E. faecalis* strain remained substantially unaffected (Figure 12c).

Overall, the microbicidal activity of AgTi5050 NP films was found to be similar to that of pure Ag NP films synthetized by the same methodology [Cavaliere E, 2015]. Indeed, although a direct comparison was not possible due to different substrate types and revised microbiological procedures, a similar reduction in the number of viable bacterial cells was observed with strains tested in both studies, using comparable bacterial inocula for surface contamination. These results encourage further studies to integrate other antimicrobial metals with activity against Gram positive bacteria.

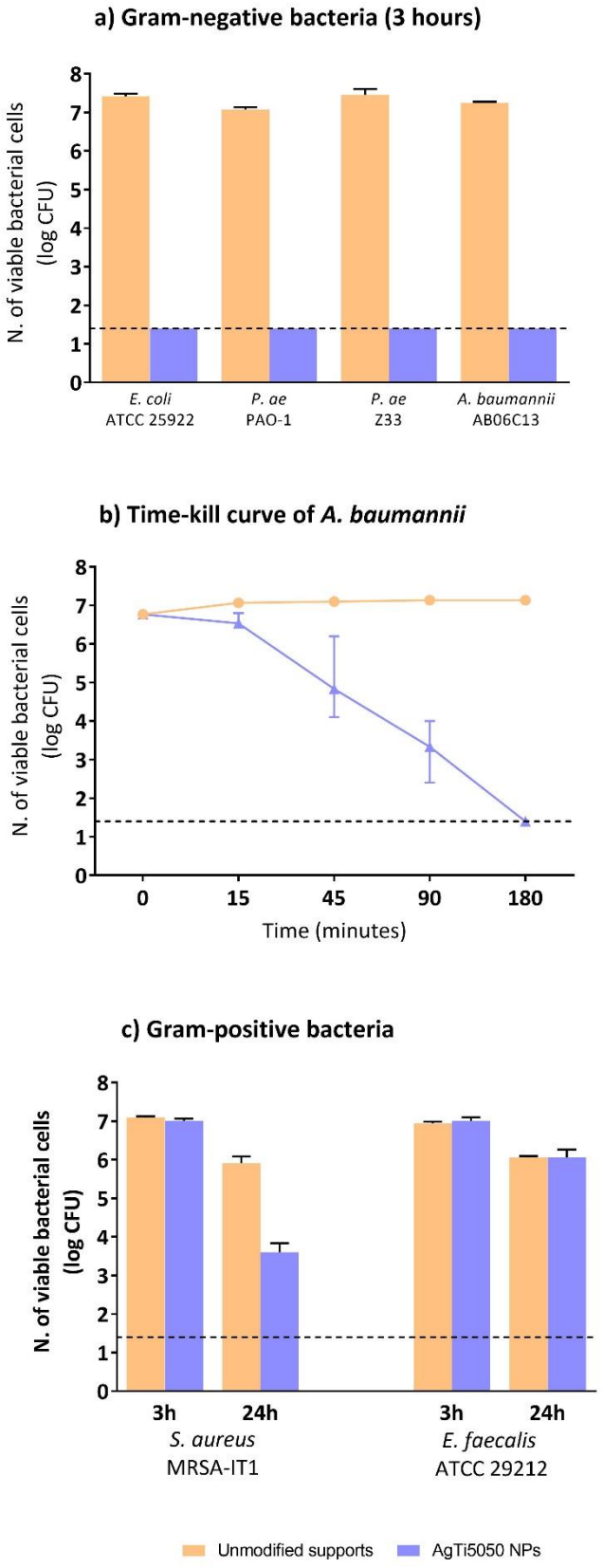

Figure 12. Antibacterial features of AgTi5050 NP films: a) antibacterial activity against Gram negative pathogens (3 hours of exposure); b) Time-kill curve of *A. baumannii* AB06C13; c) antibacterial activity against Gram positive pathogens (3 and 24 hours of exposure). CFU – Colony Forming Unit; P. ae, *P. aeruginosa*. Dotted lines indicate the detection limit of viable cell count (1.4 log CFU).

4

Differential features of the two clades of ST258 KPC-producing *Klebsiella pneumoniae* caused by different expression of the Mrk fimbrial system

Related Publications:

- Arena F, Landini G, Cannatelli A, D'Andrea MM, Giani T, Di Pilato V, Henrici De Angelis L, Pallecchi L, Rossolini GM. 2016. Differential features of the two clades of ST258 kpc-producing *Klebsiella pneumoniae* caused by different expression of the Mrk fimbrial system. Manuscript in preparation.

KPC-type carbapenemase-producing *Klebsiella pneumoniae* (KPC-KP) emerged in 1996 in the USA and since then have disseminated globally, becoming endemic in some countries including Italy [Munoz-Price LS, 2013; Giani T, 2013]. The rapid, widespread dissemination of KPC-KP is largely attributed to the clonal expansion of a single dominant strain, sequence type (ST) 258, a member of the recently designated clonal complex (CC) 258 [Bialek-Davenet S, 2014]. CC258 comprises several other sequence types linked to outbreaks, suggesting that these strains may share genetic features that predispose them to pathogenicity or to increased transmissibility. KPC-KP behave as opportunistic pathogens, able to cause all types of infections in hospitalized patients, including biofilm associated infections (e.g. catheter-associated infections or ventilator-associated pneumonia) [Jones RN, 2010; Ronald A, 2002]. Despite previous genomic analyses of ST258 [D'Andrea MM, 2014; Gaiarsa S, 2015], an explanation for its pathogenic success in the healthcare system remains unclear. Recent comparative genomic studies revealed that ST258 comprises at least two different lineages, namely clade I and clade II, which differ by a chromosomal region of ≈215 Kbp carrying the capsular polysaccharide (CPS) gene cluster [Chen L, 2014]. Strains belonging to clade II are more prevalent, in settings of high-level endemicity of KPC-KP strains of CC258, more geographically disseminated and less virulent in the animal model [Arena F, 2016; D'Andrea MM, 2014; Diago-Navarro E, 2014]. The reasons underlying the epidemiological success of clade II isolates remain largely unknown. However, a different attitude to colonize the human gut and/or persist in abiotic surfaces could be involved.

In order to further investigate the differential widespread dissemination of clade I and clade II, we performed a genome comparison of two strains, representative of the two clades, KK207/1 and

KKBO-1 (clade I and clade II, respectively). Results obtained enabled us to identify an adjunctive difference between the two clades in the *mrk* mannose-resistant fimbrial gene cluster. Since *mrkABCDF* genes (including determinants encoding the major fimbrial subunit MrkA), are important virulence factors in *K. pneumoniae* pathogenesis [Alcántar-Curiel MD, 2013], we further analyzed the presence of a functional Mrk system in relationship with biofilm formation ability of KK207/1 and KKBO-1 strains.

Sequences analysis showed that in KKBO-1 (clade II) the *mrkABCDFHIJ* genes cluster is intact, while in the KK207/1 genome (clade I), the *mrkH* positive transcriptional regulator is disrupted by an IS*Ec21*-like element, at nucleotide 207, which determine a truncated, likely non-functional protein (Figure 13). MrkH is a transcriptional activator that responds to the second messenger, c-di-GMP, and regulates the expression of the *mrkABCDF* cluster [Yang J, 2016]. From a screening of the NCBI database we found that this alteration is a typical feature of ST258 clade I genomes. Based on results obtained, we evaluated the expression of the *mrkA* gene by quantitative real-time PCR both in KKBO-1, in KK207/1 and in KK207/1 strain cloned with wilde-type *mrkH* gene (KK207/1_pACYC-*mrkH*). *mrkA* expression was significantly higher in the KKBO-1 than in KK207/1 (6.2 ± 0.7 fold**,** *p* value <0.0005) in agreement with the disruption of the positive regulator, and a further proof was obtained by evaluating the *mrkA* gene expression in KK207/1_pACYC-*mrkH*. MrkA was increased 675.5 ± 0.8 fold as compared to the parental strain after growth under conditions for optimal type 3 fimbriae formation (*p* value <0.0005). Biofilm assays were performed with Calgary Biofilm Device in order to evaluate the differential capabilities of the three strains to produce biofilm on abiotic surfaces, since hyperfimbriate *K. pneumoniae* strains has been demonstrated better biofilm producer compared to non-fimbriate ones [Johnson JG, 2010]. Results were consistent with previous studies, indeed KK207/1 showed a significantly decreased ability to form biofilm *in vitro* (3.3 log ± 0.3 CFU/peg) compared to KKBO-1 (5.4 log ± 0.4 CFU/peg) (*p* value ≤ 0.05). In agreement with the role of *mrkH* gene in biofilm formation, the KK207/1 strain with the cloned wild type *mrkH* gene showed a significantly increased ability to form biofilm compared to KK207/1 strain with interrupted *mrkH* gene (5.69 ± 0.06 log CFU/peg) (Figure 14).

In conclusion, with these preliminary results we partially explain the restricted geographic dissemination of clade I KPC-KP compared to clade II KPC-KP isolates, by detecting non-silent mutation in *mrkABCDFHIJ* genes cluster which leads to reduced biofilm formation capability on abiotic surfaces. Further studies will be needed to investigate the implication of MrkH alteration in adherence to biotic surfaces (e.g. intestinal cell model).

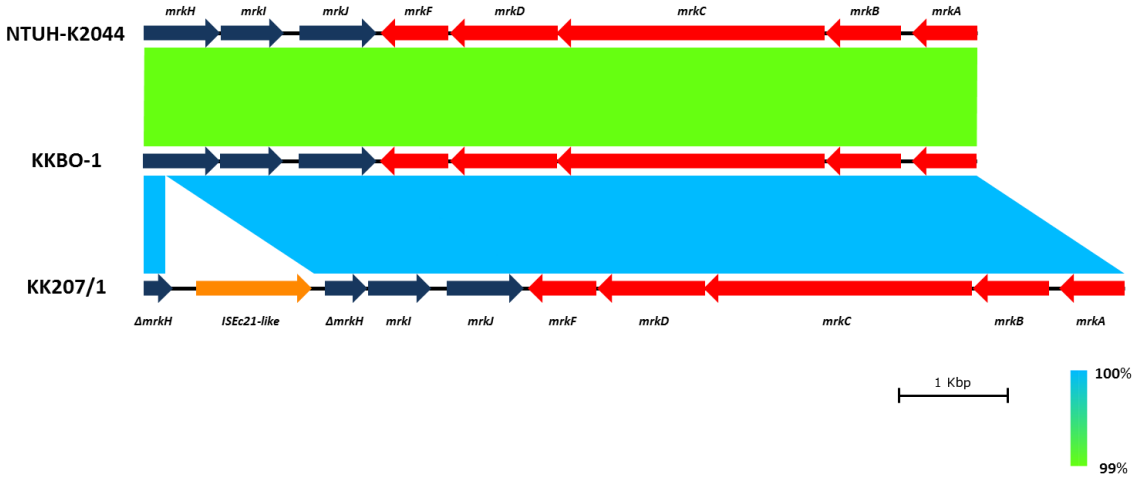

Figure 13. Genetic organization of the *mrkABCDF* and *mrkHIJ* gene clusters from *K. pneumoniae* strains, NTUH-K2044 (GenBank Ref: AP006725), KKBO-1 (GenBank Ref: AVFC01000000) and 207/1 (GenBank Ref: LJOO01000000).

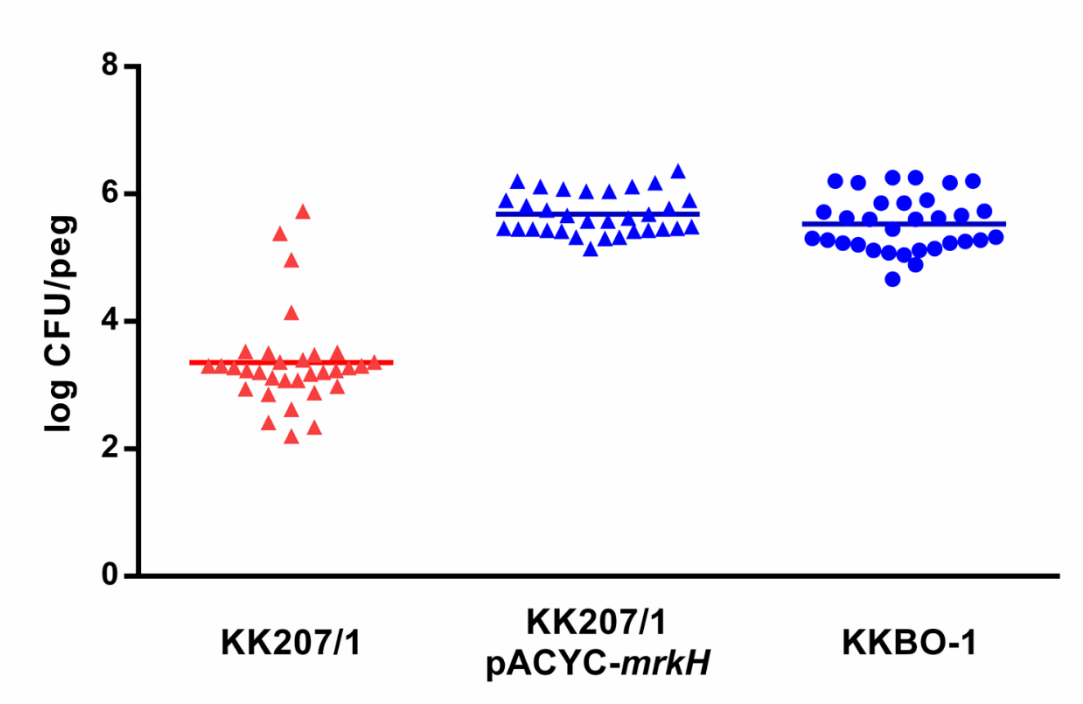

Figure 14. Biofilm formation of *K. pneumoniae* KK207/1 (interrupted *mrkH* gene), KK207/1_pACYC-*mrkH* (complemented strain with *mrkH* wild type gene) and KKBO-1 (*mrkH* wild type gene).

5

The effects of diode laser on *Staphylococcus aureus* biofilm grown on titanium oxide surface of dental implants

Related Publications:

- Giannelli M, Landini G, Materassi F, Chellini F, Antonelli A, Tani A, Zecchi-Orlandini S, Rossolini GM, and Bani D. 2016. The effects of diode laser on *Staphylococcus aureus* biofilm and *Escherichia coli* lipopolysaccharide adherent to titanium oxide surface of dental implants. An *in vitro* study. *Lasers in Medical Science*, 31(8), 1613-1619.

Upon completion of hard and soft tissue integration following implant placement, peri-implant diseases have been defined as i) development of mucosal inflammation around implants without loss of supporting bone (i.e. peri-implant mucositis), and ii) presence of inflammation with additional loss of supporting bone (i.e. peri-implantitis) [Zitzmann NU, 2008]. It has been extensively shown that bacterial pathogens and their pro-inflammatory products could play a role in pathogenesis of peri-implantitis and failing implants [Nouneh RA, 2001; Zhuang LF, 2016]. A cluster of bacteria including *Staphylococcus aureus* has been associated with peri-implantitis [Persson GR, 2014]. In particular, the colonization of dental implant and subsequent infection mediated by *S. aureus* could be linked to its ability to adhere to titanium surfaces and to its known biofilm-producing capability [Harris LG, 2004; Zhao B, 2014; Thurnheer T, 2015]. Several methods of implant decontamination have been proposed for the treatment of peri-implantitis, including air-powered abrasive treatments, citric acid, mechanical cleaning with metal and plastic curettes or ultrasonic scalers [Suarez F, 2013; Sahrmann P, 2015], in combination with local and systemic antibiotic therapy [Javed F, 2013]. However, none of these methods gave satisfactory results in terms of eradication of bacteria from the contaminated implant surfaces [Mouhyi J, 2000]. In the last decade, the positive effects of laser irradiation in cleaning and decontaminating the implant surfaces have been reported [Roncati M, 2013; Aoki A, 2015]. Despite the numerous reports in the literature on the clinical use of lasers in implantology, little is known about the mechanisms by which lasers exert their effects on dental implant surfaces. Moreover, considering that the physical characteristics of implants vary greatly among different producers, there is no consensus on a standard laser-aided treatment for peri-implantitis. In the present *in vitro* study, we investigated the effects of diode laser (λ 808 nm) in non-contact-mode and in continuous or pulsed wave emission on *S. aureus* biofilm grown on titanium discs.

S. aureus ATCC 25925 biofilms were grown for 48 hours on titanium discs, with the same surface finish as the osseous inferface (TiUnite) of dental implants (Nobel Biocare Services AG, Zürich, Switzerland) and analyzed by viable cell count and by scanning electron microscope (SEM). Mature biofilms (reaching 7.3 ± 0.1 log CFU/disc) (Figure 15) were treated with diode laser (λ 808 nm) in both pulsed and continuous mode, for one minute per side of exposition. Laser treatment induced a statistically significant reduction of viable cells in comparison with the untreated biofilm (1.5 and 2.2 log CFU/disc reduction, respectively; *p* value <0.01) (Figure 15). To note, the irradiation in continuous mode appeared to have a higher efficacy in terms of viable cell count reduction, even if the comparison between the two treatments did not reach statistical significance (*p* value >0.05). Moreover, the diode laser treatment of *S. aureus* biofilms was evaluated by SEM. Figure 16 shows the structure of TiUnite surfaces before and after staphylococcal infection and laser treatment (Figure 16). As depicted in Figure 16a, the uninfected surface of the TiUnite discs was characterized by a titanium oxide layer with numerous micro-cavities. Mature staphylococcal biofilm colonization caused the presence of an adherent layer of closely packed bacteria embedded in an amorphous substance (Figure 16b). The laser treatment both in continuous (Figure 16c) and pulsed (Figure 16d) wave mode, caused a sharp reduction of the amount of adherent bacteria. No clear differences were observed between the continuous and pulsed wave mode of irradiation.

In conclusion, even if eradication of mature staphylococcal biofilm grown on titanium discs were not achieved at the tested conditions, the λ 808-nm diode laser can be considered a valuable tool for increasing the odds of successful control of peri-implant disease, indeed a significant reduction of microbial load were highlighted by both viable cell count and SEM observation.

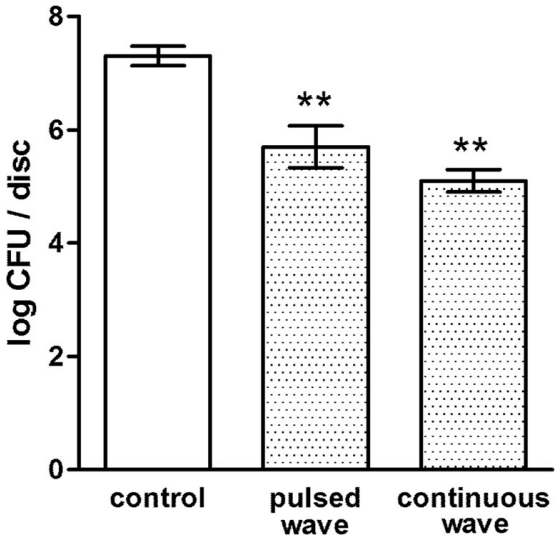

Figure 15. Effect of the different laser treatments on decontamination of the titanium surface coated with *S. aureus* ATCC 25923 biofilm evaluated by viable cell count. Values are means ± s.e.m. ***p* value <0.01 *vs.* controls.

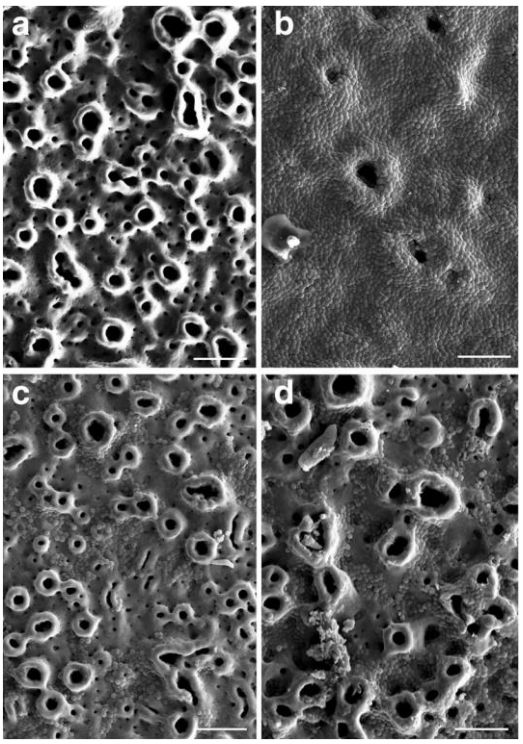

Figure 16. Representative scanning electron micrographs of uncoated (a) and biofilm-coated titanium discs (b) from untreated control, showing a dense bacterial layer masking the roughness of the titanium oxide surface, and pulsed (c) and continuous (d) wave laser irradiation, showing an almost complete removal of the biofilm coating and few residual bacteria. Bars = 10 µm.

Part IV

APPENDIX

SELECTED BIBLIOGRAPHY

Alcántar-Curiel MD, Blackburn D, Saldaña Z, Gayosso-Vázquez C, Iovine N, De la Cruz MA, and Giron JA. Multi-functional analysis of *Klebsiella pneumoniae* fimbrial types in adherence and biofilm formation. Virulence. 2013;**4**(2):129-138.

Alfredsson H, Malmborg AS, and Strandvik B. N-acetylcysteine and 2-mercaptoethane sulphonate inhibit anti-pseudomonas activity of antibiotics *in vitro*. Eur J Respir Dis. 1987;**70**:213-217.

Aoki A, Mizutani K, Schwarz F, Sculean A, Yukna RA, Takasaki AA, Romanos GE, *et al.* Periodontal and peri-implant wound healing following laser therapy. Periodontol. 2015;**68**:217–269.

Arena F, Henrici De Angelis L, Cannatelli A, Di Pilato V, Amorese M, D'Andrea MM, *et al.* Colistin resistance caused by inactivation of the MgrB regulator is not associated with decreased virulence of ST258 KPC carbapenemase-producing *Klebsiella pneumoniae*. Antimicrobial Agents and Chemotherapy. 2016;**60**(4):2509-2512.

Aslam S, and Darouiche RO. Role of antibiofilm-antimicrobial agents in control of device-related infections. The International journal of artificial organs. 2011;**34**(9):752.

Aslam S, Trautner BW, Ramanathan V, and Darouiche RO. Combination of tigecycline and N-acetylcysteine reduces biofilm-embedded bacteria on vascular catheters. Antimicrobial agents and chemotherapy. 2007;**51**(4):1556-1558.

Barber KE, Werth BJ, McRoberts JP, and Rybak MJ. A novel approach utilizing biofilm time-kill curves to assess the bactericidal activity of Ceftaroline combinations against biofilm-producing methicillin-resistant *Staphylococcus aureus*. Antimicrob Agents Chemother. 2014;**58**:2989-92.

Bialek-Davenet S, Criscuolo A, Ailloud F, Passet V, Jones L, Delannoy-Vieillard AS, *et al*. Genomic definition of hypervirulent and multidrug-resistant *Klebsiella pneumoniae* clonal groups. Emerging infectious diseases. 2014;**20**(11):1812-20.

Bjarnsholt T, Ciofu O, Molin S, Givskov M, and Høiby N. Applying insights from biofilm biology to drug development - can a new approach be developed? Nat Rev Drug Discov 2013;**12**:791-808.

Blasi F, Pave C, Rossolini GM, Pallecchi L, Matera MG, Rogliani P, and Cazzola M. The effect of N-acetylcysteine on biofilms: implications for the treatment of respiratory tract infections. Respir Med. 2016;**117**:190-197.

Cannatelli A, D'Andrea MM, Giani T, Di Pilato V, Arena F, Ambretti S, Gaibani P, and Rossolini GM. *In vivo* emergence of colistin resistance in *Klebsiella pneumoniae* producing KPC-type carbapenemases mediated by insertional inactivation of the PhoQ/PhoP mgrB regulator. Antimicrob Agents Chemother. 2013;**57**:5521-6.

Cavaliere E, De Cesari S, Landini G, Riccobono E, Pallecchi L, Rossolini GM, and Gavioli L. Highly bactericidal Ag nanoparticle films obtained by cluster beam deposition. Nanomedicine: Nanotechnology, Biology and Medicine. 2015;**11**(6):1417-1423.

Cazzola M, Calzetta L, Page C, Jardim J, Chuchalin AG, Rogliani P, and Matera MG. Influence of N-acetylcysteine on chronic bronchitis or COPD exacerbations: a meta-analysis. Eur Respir Rev. 2015;**24:**451-461.

Chen L, Mathema B, Pitout JD, DeLeo FR, and Kreiswirth BN. Epidemic *Klebsiella pneumoniae* ST258 is a hybrid strain. MBio. 2014;**5**(3):e01355-14.

Chiodi M, Cheney CP, Vilmercati P, Cavaliere, E, Mannella N, Weitering HH, and Gavioli L. Enhanced dopant solubility and visible-light absorption in Cr–N codoped TiO2 nanoclusters. The Journal of Physical Chemistry C. 2012;**116**(1): 311-318.

Clinical and Laboratory Standards Institute. Methods for determining bactericidal activity of antimicrobial agents; approved guidelines (M26-A). Clinical and Laboratory Standards Institute, Wayne, PA. 1999.

Clinical and Laboratory Standards Institute. Methods for dilution antimicrobial susceptibility tests for bacteria that grow aerobically: approved standard – tenth edition (M07-A10). Clinical and Laboratory Standards Institute, Wayne, PA. 2015.

Conlon BP, Nakayasu ES, Fleck LE, LaFleur MD, Isabella VM, Coleman K, *et al*. Activated ClpP kills persisters and eradicates a chronic biofilm infection. Nature 2013;**503**:365-70.

D'Andrea MM, Amisano F, Giani T, Conte V, Ciacci, N., Ambretti S, *et al*. Diversity of capsular polysaccharide gene clusters in Kpc-producing *Klebsiella pneumoniae* clinical isolates of sequence type 258 involved in the Italian epidemic. PloS one. 2014;**9**(5):e96827.

D'Andrea MM, Venturelli C, Giani T, Arena F, Conte V, Bresciani P, Rumpianesi F, Pantosti A, Narni F, Rossolini GM. Persistent carriage and infection by multidrug-resistant *Escherichia coli* ST405 producing NDM-1 carbapenemase: report on the first Italian cases. J Clin Microbiol. 2011;**49**:2755-2758.

Diago-Navarro E, Chen L, Passet V, Burack S, Ulacia-Hernando A, Kodiyanplakkal RP, *et al.* Carbapenem-resistant *Klebsiella pneumoniae* exhibit variability in capsular polysaccharide and capsule associated virulence traits. The Journal of Infectious Diseases. 2014;**210**(5):803–813.

Diancourt L, Passet V, Nemec A, Dijkshoorn L, Brisse S. The population structure of Acinetobacter baumannii: expanding multiresistant clones from an ancestral susceptible genetic pool. PLoS One. 2010;**5**:e10034.

El-Baky RMA, Dalia MMAE, and Gamal FMG. N-acetylcysteine inhibits and eradicates *Candida albicans* biofilms. American Journal of Infectious Diseases and Microbiology. 2014;**2**(5):122-130.

El-Feky MA, El-Rehewy MS, Hassan MA, Abolella HA, Abd El-Baky RM, and Gad GF. Effect of ciprofloxacin and N-acetylcysteine on bacterial adherence and biofilm formation on ureteral stent surfaces. Pol J Microbiol. 2009;**58**(3):261-7.

Gaiarsa S, Comandatore F, Gaibani P, Corbella M, Dalla Valle C, Epis S, ***et al***. Genomic epidemiology of *Klebsiella pneumoniae* in Italy and novel insights into the origin and global evolution of its resistance to carbapenem antibiotics. Antimicrobial agents and chemotherapy. 2015;**59**(1):389-396.

Giani T, D'Andrea MM, Pecile P, Borgianni L, Nicoletti P, Tonelli F, Bartoloni A, Rossolini GM. Emergence in Italy of *Klebsiella pneumoniae* sequence type 258 producing KPC-3 carbapenemase. J Clin Microbiol. 2009;**47**:3793-3794.

Giani T, Pini B, Arena F, Conte V, Bracco S, and Migliavacca R. Epidemic diffusion of KPC carbapenemase-producing *Klebsiella pneumoniae* in Italy: results of the first countrywide survey. Eurosurveillance. 2013.

Goswami M, Jawali N. 2010. N-acetylcysteine-mediated modulation of bacterial antibiotic susceptibility. Antimicrob Agents Chemother. 2010;**54**:3529-3350.

Hall-Stoodley L, Costerton JW, Stoodley P. Bacterial biofilms: from the natural environment to infectious diseases. Nat Rev Microbiol 2004;**2**:95-108.

Harmsen D, Claus H, Witte W, Rothgänger J, Claus H, Turnwald D, *et al*. Typing of methicillin-resistant *Staphylococcus aureus* in a university hospital setting by using novel software for *spa* repeat determination and database management. J Clin Microbiol. 2003;**41**:5442–8.

Harris LG, Richards RG. *Staphylococcus aureus* adhesion to different treated titanium surfaces. J Mater Sci Mater Med. 2004;**15**:311–314.

Harrison JJ, Stremick CA, Turner RJ, Allan ND, Olson ME, Ceri H. Microtiter susceptibility testing of microbes growing on peg lids: a miniaturized biofilm model for high-throughput screening. Nat Protoc 2010;**5**:1236-54.

Høiby N, Bjarnsholt T, Moser C, Bassi GL, Coenye T, Donelli G, *et al.* ESCMID guideline for the diagnosis and treatment of biofilm infections 2014. Clinical microbiology and infection. 2015;**21**:S1-S25.

Humphreys H. Self-disinfecting and microbiocide-impregnated surfaces and fabrics: what potential in interrupting the spread of healthcare-associated infection? Clin Infect Dis. 2014;**58**:848–53.

Hurst GA, Shaw PB, LeMaistre CA. Laboratory and clinical evaluation of the mucolytic properties of acetylcysteine. Am Rev Respir Dis. 1967;**96:**962-970.

Javed F, Alghamdi AS, Ahmed A, Mikami T, Ahmed HB, Tenenbaum HC. Clinical efficacy of antibiotics in the treatment of peri-implantitis. Int Dent J. 2013;**63**:169–176.

Johnson JG, and Clegg S. Role of MrkJ, a phosphodiesterase, in type 3 fimbrial expression and biofilm formation in *Klebsiella pneumoniae*. J. Bacteriol. 2010;**192**:3944–3950.

Jones RN. Microbial etiologies of hospital-acquired bacterial pneumonia and ventilator-associated bacterial pneumonia. Clin. Infect. Dis. 2010;**51**(Suppl. 1):S81–S87.

Kiedrowski MR, Horswill AR. New approaches for treating staphylococcal biofilm infections. Ann N Y Acad Sci 2011;**1241**:104-21.

Kondo Y, Ito T, Ma XX, Watanabe S, Kreiswirth BN, Etienne J, *et al.* Combination of multiplex PCRs for staphylococcal cassette chromosome *mec* type assignment: rapid identification system for *mec*, *ccr*, and major differences in junkyard regions. Antimicrob Agents Chemother 2007;**51**:264–74.

Landini G, Riccobono E, Giani T, Arena F, Rossolini GM, Pallecchi L. Bactericidal activity of ceftaroline against mature *Staphylococcus aureus* biofilms. Int J Antimicrob Agents. 2015;**45**:551-553.

Lewis K. Persister cells, dormancy and infectious disease. Nat Rev Microbiol 2007;**5**:48-56.

Mansouri MD, Hull RA, Stager CE, Cadle RM, and Darouiche RO. *In vitro* activity and durability of a combination of an antibiofilm and an antibiotic against vascular catheter colonization. Antimicrobial agents and chemotherapy. 2013;**57**(1):621-625.

Moon JH, Choi YS, Lee HW, Heo JS, Chang SW, and Lee JY. Antibacterial effects of N-acetylcysteine against endodontic pathogens. Journal of Microbiology. 2016;**54**(4):322-329.

Moon JH, Jang EY, Shim KS, and Lee JY. *In vitro* effects of N-acetyl cysteine alone and in combination with antibiotics on *Prevotella intermedia*. Journal of Microbiology. 2015;**53**(5):321-329.

Mouhyi J, Sennerby L, Van Reck J. The soft tissue response to contaminated and cleaned titanium surfaces using CO_2 laser, citric acid and hydrogen peroxide. An experimental study in the rat abdominal wall. Clin Oral Implants Res.2000;**11**:93–98.

Munoz-Price LS, Poirel L, Bonomo RA, Schwaber MJ, Daikos GL, Cormican M, *et al*. Clinical epidemiology of the global expansion of *Klebsiella pneumoniae* carbapenemases. The Lancet Infectious Diseases. 2013;**13**(9):785–796.

Nouneh RA, Wataha JC, Hanes PJ, Lockwood PE. Effect of lipopolysaccharide contamination on the attachment of osteoblastlike cells to titanium and titanium alloy *in vitro*. J Oral Implantol. 2001;**27**:174–179.

Oberauner L, Zachow C, Lackner S, Högenauer C, Smolle KH, and Berg G. The ignored diversity: complex bacterial communities in intensive care units revealed by 16S pyrosequencing. Scientific reports. 2013;**3**.

Olofsson AC, Hermansson M, and Elwing H. N-acetyl-L-cysteine affects growth, extracellular polysaccharide production, and bacterial biofilm formation on solid surfaces. Applied and environmental microbiology. 2003;**69**(8):4814-4822.

Olsen L. Biofilm-specific antibiotic tolerance and resistance. Eur. J. Clin. Microbiol. Infect. Dis. 2015;**34**(5):877-886.

Otter JA, Yezli S, and French GL. The role played by contaminated surfaces in the transmission of nosocomial pathogens. Infection Control & Hospital Epidemiology. 2011;**32**(07):687-699.

Pallavicini P, Taglietti A, Dacarro G, Diaz-Fernandez Y A, Galli M, Grisoli P, Patrini M, Santucci De Magistris G, Zanoni R. Self-assembled monolayers of silver nanoparticles firmly grafted on glass surfaces: Low Ag^+ release for an efficient antibacterial activity. J Coll Interf Sci 2010;**350**:110-116.

Parry MF, Neu HC. Effect of N-acetylcysteine on antibiotic activity and bacterial growth *in vitro*. J Clin Microbiol. 1977;**5**:58-61.

Perez-Giraldo C, Rodriguez-Benito A, Moran FJ, Hurtado C, Blanco MT, and Gomez-Garcia AC. Influence of N-acetylcysteine on the formation of biofilm by *Staphylococcus epidermidis*. Journal of Antimicrobial Chemotherapy. 1997;**39**(5):643-646.

Persson GR, and Renvert S. Cluster of Bacteria Associated with Peri-Implantitis. Clinical implant dentistry and related research. 2014;**16**(6):783-793.

Principe L, Piazza A, Giani T, Bracco S, Caltagirone MS, Arena F, Nucleo E, Tammaro F, Rossolini GM, Pagani L, Luzzaro F; AMCLI-CRAb Survey Participants. Epidemic diffusion of OXA-23-producing *Acinetobacter baumannii* isolates in Italy: results of the first cross-sectional countrywide survey. J Clin Microbiol. 2014;**52**:3004-10.

Quinn MM, Markkanen PK, Galligan CJ, Sama SR, Kriebel D, Gore RJ, *et al.* Occupational health of home care aides: results of the safe home care survey. Occupational and environmental medicine, 2016;**73**(4):237-245.

Riccio ML, Pallecchi L, Docquier JD, Cresti S, Catania MR, Pagani L, Lagatolla C, Cornaglia G, Fontana R, Rossolini GM. Clonal relatedness and conserved integron structures in epidemiologically unrelated *Pseudomonas aeruginosa* strains producing the VIM-1 metallo-beta-lactamase from different Italian hospitals. Antimicrob Agents Chemother. 2005;**49**:104-110.

Rodríguez-Beltrán J, Cabot G, Valencia EY, Costas C, Bou G, Oliver A, Blázquez J. N-acetylcysteine selectively antagonizes the activity of imipenem in Pseudomonas aeruginosa by an OprD-mediated mechanism. Antimicrob Agents Chemother. 2015;**59**:3246-3251.

Ronald A. The etiology of urinary tract infection: traditional and emerging pathogens. Am. J. Med. 2002;**113**(Suppl. 1A):14S–19S.

Roncati M, Lucchese A, Carinci F. Non-surgical treatment of peri-implantitis with the adjunctive use of an 810-nm diode laser. J Indian Soc Periodontol. 2013;**17**:812–815.

Rossolini GM, Arena F, Pecile P, Pollini S. Update on the antibiotic resistance crisis. Curr Opin Pharmacol. 2014;**18**:56-60.

Rushworth GF, Megson IL. Existing and potential therapeutic uses for N-acetylcysteine: the need for conversion to intracellular glutathione for antioxidant benefits. Pharmacol Ther. 2014;**141:**150-159.

Sahrmann P, Ronay V, Hofer D, Attin T, Jung RE, Schmidlin PR. *In vitro* cleaning potential of three different implant debridement methods. Clin Oral Implants Res. 2015;**26**:314–319.

Samuni Y, Goldstein S, Dean OM, Berk M. The chemistry and biological activities of N-acetylcysteine. Biochim Biophys Acta. 2013;**1830:**4117-4129.

Saravolatz LD, Stein GE, Johnson LB. Ceftaroline: a novel cephalosporin with activity against methicillin-resistant *Staphylococcus aureus*. Clin Infect Dis 2011;**52**:1156-63.

Seil JT, Webster TJ. Antimicrobial applications of nanotechnology: methods and literature. Int J Nanomedicine. 2012;**7**:2767-81.

Skov M, Pressler T, Lykkesfeldt J, Poulsen HE, Jensen PØ, Johansen HK, Qvist T, Kræmer D, Høiby N, Ciofu O. The effect of short-term, high-dose oral N-acetylcysteine treatment on oxidative stress markers in cystic fibrosis patients with chronic *P. aeruginosa* infection - a pilot study. J Cyst Fibros. 2015;**14:**211-218.

Stover CK, Pham XQ, Erwin AL, Mizoguchi SD, Warrener P, Hickey MJ, *et al.* Complete genome sequence of *Pseudomonas aeruginosa* PAO1, an opportunistic pathogen. Nature. 2000;**406**:959-964.

Suarez F, Monje A, Galindo-Moreno P, Wang HL. Implant surface detoxification: a comprehensive review. Implant Dent. 2013;**22**:465–473.

Szkudlarek U, Zdziechowski A, Witkowski K, Kasielski M, Luczyńska M, Luczyński R, Sarniak A, Nowak D. Effect of inhaled N-acetylcysteine on hydrogen peroxide exhalation in healthy subjects. Pulm Pharmacol Ther. 2004;**17**:155-162.

Thurnheer T, Belibasakis GN. Incorporation of staphylococci into titanium-grown biofilms: an *in vitro* "submucosal" biofilm model for peri-implantitis. Clin Oral Implants Res. 2015.

Weber DJ, Rutala WA. Self-disinfecting surfaces: review of current methodologies and future prospects. Am J Infect Control. 2013;**41**:S31–5.

Wootton M, Howe RA, Hillman R, Walsh TR, Bennett PM, MacGowan AP. A modified population analysis profile (PAP) method to detect hetero-resistance to vancomycin in *Staphylococcus aureus* in a UK hospital. J Antimicrob Chemother 2001;**47**:399–403.

World Health Organization. Antimicrobial resistance: global report on surveillance. 2014; (http://www.who.int/drugresistance/documents/survsurveillancere/en/).

Wu KM, Li LH, Yan JJ, Tsao N, Liao TL, Tsai HC, *et al.* Genome sequencing and comparative analysis of *Klebsiella pneumoniae* NTUH-K2044, a strain causing liver abscess and meningitis. J Bacteriol. 2009;**191**:4492-4501.

Yang F, Liu LH, Li XP, Luo JY, Zhang Z, Yan ZT, Zhang SD, Li HS. Short communication: N-Acetylcysteine-mediated modulation of antibiotic susceptibility of bovine mastitis pathogens. J Dairy Sci. 2016;**99**:4300-4302.

Yang J, Wilksch JJ, Tan JW, Hocking DM, Webb CT, Lithgow T, *et al.* Transcriptional activation of the mrkA promoter of the Klebsiella pneumoniae type 3 fimbrial operon by the c-di-GMP-dependent MrkH protein. PloS one. 2016;**8**(11):e79038. 10.

Yokoe DS, Anderson DJ, Berenholtz SM, Calfee DP, Dubberke ER, Ellingson KD, *et al.* A compendium of strategies to prevent healthcare-associated infections in acute care hospitals: 2014 updates. Infect Control Hosp Epidemiol. 2014;**35**:S21-31.

Zhao B, van der Mei HC, Subbiahdoss G, de Vries J, Rustema-Abbing M, Kuijer R, Busscher HJ, Ren Y. Soft tissue integration versus early biofilm formation on different dental implant materials. Dent Mater. 2014;**30**:716–727.

Zhao T, and Liu Y. N-acetylcysteine inhibit biofilms produced by *Pseudomonas aeruginosa*. BMC microbiology. 2010;**10**(1):1.

Zhuang LF, Watt RM, Mattheos N, Si MS, Lai HC, and Lang NP. Periodontal and peri-implant microbiota in patients with healthy and inflamed periodontal and peri-implant tissues. Clinical oral implants research. 2016;**27**(1), 13-21.

Zitzmann NU, Berglundh T. Definition and prevalence of peri-implant diseases. J Clin Periodontol. 2008;**35**:286–29.

RELATED PUBBLICATIONS

International Journal of Antimicrobial Agents xxx (2015) xxx–xxx

Contents lists available at ScienceDirect

International Journal of Antimicrobial Agents

journal homepage: http://www.elsevier.com/locate/ijantimicag

Letter to the Editor

Bactericidal activity of ceftaroline against mature *Staphylococcus aureus* biofilms☆

Sir,

Staphylococcus aureus biofilms represent a major clinical challenge in some infections, including those of artificial devices (and related bloodstream infections), osteomyelitis, endocarditis and complicated skin and soft-tissue infections [1]. Following the ever-increasing prevalence of meticillin-resistant *S. aureus* (MRSA) worldwide, the activity of anti-MRSA agents against staphylococcal biofilms is a matter of increasing interest [1].

Ceftaroline, the active metabolite of ceftaroline fosamil, is a new cephalosporin antibiotic exhibiting bactericidal activity against *S. aureus* isolates, including MRSA [2]. Recently, ceftaroline combinations with either daptomycin or vancomycin were found to be bactericidal (>3 log reduction in viable cell count) against 1-day-old MRSA biofilms after 24 h of exposure, although exposure to ceftaroline alone did not result in sustained killing [3].

Here we investigated the activity of ceftaroline against mature (4-day-old) staphylococcal biofilms and demonstrated that after prolonged exposure times ceftaroline exhibited a remarkable bactericidal activity both against MRSA and meticillin-susceptible *S. aureus* (MSSA) biofilms at notably low concentrations.

The study was performed with five *S. aureus* strains, including ATCC 6538 (MSSA reference strain), ATCC 43300 (MRSA reference strain) and three MRSA strains isolated from biofilm-associated infections and exhibiting different resistance phenotypes (Supplementary Table S1) and ceftaroline minimum inhibitory concentrations (MICs): MRSA-IT1 (ceftaroline MIC = 0.5 μg/mL); and MRSA-IT16 and MRSA-IT23 (ceftaroline MIC = 2 μg/mL). Biofilm susceptibility testing was performed using the Calgary Biofilm Device (MBEC High-Throughput Assay; Innovotech Inc., Edmonton, Alberta, Canada) as previously described [4]. Briefly, 4-day-old biofilms were challenged with daily refreshed antibiotic for up to 6 days using ceftaroline concentrations achievable in vivo (range 0.03–16 μg/mL) [2]. The MICB (MIC of planktonic cells shed from biofilms), MBEC (minimum biofilm eradication concentration) and MVCC (mean viable cell count per peg) were determined at Days 1, 2, 3 and 6 of exposure. For biofilm time–kill curves, MSSA ATCC 6538 was used as a model and was tested with ten ceftaroline concentrations (range 0.03–16 μg/mL). For all other strains, time–kill curves were determined using ceftaroline 2 μg/mL and 8 μg/mL, plus a third concentration equal to the respective MIC values for MRSA ATCC 43300 and MRSA-IT1. In addition, vancomycin (Sigma–Aldrich, Milan, Italy) was also used as a comparator in time–kill curves with MSSA ATCC 6538 using concentrations corresponding to 1× and 8× susceptibility breakpoints (i.e. vancomycin 2 μg/mL and 16 μg/mL and ceftaroline 1 μg/mL and 8 μg/mL). Further experimental details are reported in the Supplementary Methods. Ceftaroline powder was provided by AstraZeneca (Milan, Italy).

Mature biofilms were formed by a mean of 6.3 ± 0.2, 7.3 ± 0.3, 6.2 ± 0.3, 4.1 ± 0.4 and 4.2 ± 0.3 log CFU/peg for MSSA ATCC 6538, MRSA ATCC 43300, MRSA-IT1, MRSA-IT16 and MRSA-IT23, respectively. MICBs ranged within one doubling dilution of the respective MICs and were stable over the 6-day challenge experiment, demonstrating that no resistant mutants were selected under these conditions (Supplementary Table S1). MBECs remained above the maximum ceftaroline concentration tested (i.e. >16 μg/mL) for all tested strains (Supplementary Table S1). However, despite the lack of complete biofilm eradication, time–kill curves of MSSA ATCC 6538 revealed a bactericidal activity already after 24 h of exposure at a ceftaroline concentration achievable in vivo (16 μg/mL) (Fig. 1A). Starting from Day 2, a bactericidal effect was already observed at concentrations as low as the MIC (0.25 μg/mL), and the MVCC fell below the limit of detection (1.1 log CFU/peg) at concentrations ≥8 μg/mL and ≥1 μg/mL after 3 days and 6 days of exposure, respectively. In agreement with the known time-dependent activity of ceftaroline [2], no concentration-dependent effect was observed (Fig. 1A). At the tested concentrations, vancomycin appeared to be significantly less effective than ceftaroline against mature biofilms of MSSA ATCC 6538 (Fig. 1B), in agreement with the lower antibiofilm activity of vancomycin compared with another anti-MRSA cephalosporins recently demonstrated in a similar experimental model [5]. Time–kill curves of the four MRSA strains were overall in agreement with those of MSSA ATCC 6538 (Fig. 1C–F). In particular, MRSA ATCC 43300 and MRSA-IT1 showed similar time–kill curves characterised by absence of killing at ceftaroline concentrations equal to MICs and lack of a concentration-dependent effect at concentrations higher than the MIC (Fig. 1C, D). Despite the clinical strains MRSA-IT16 and MRSA-IT23 producing a less abundant and less homogeneous biofilm, the overall response to ceftaroline was coherent. Indeed, whilst fluctuating results were obtained with ceftaroline 2 μg/mL (corresponding to the MIC), a bactericidal activity was evident starting from Day 2 of exposure at ceftaroline 8 μg/mL (Fig. 1E, F).

In conclusion, using a consolidated method for in vitro biofilm susceptibility testing (the Calgary Biofilm Device), we demonstrated that, following prolonged exposure times, ceftaroline exerted a bactericidal activity both against MSSA and MRSA biofilms. These results reinforce previous findings on the in vitro efficacy of ceftaroline combinations against staphylococcal biofilms [3] and encourage further studies on the role of ceftaroline for the treatment of biofilm-associated staphylococcal infections.

☆ Part of the results of this study were presented at the 54th Interscience Conference on Antimicrobial Agents and Chemotherapy (ICAAC), 5–9 September 2014, Washington, DC.

http://dx.doi.org/10.1016/j.ijantimicag.2015.01.001
0924-8579/© 2015 Elsevier B.V. and the International Society of Chemotherapy. All rights reserved.

Please cite this article in press as: Landini G, et al. Bactericidal activity of ceftaroline against mature *Staphylococcus aureus* biofilms. Int J Antimicrob Agents (2015), http://dx.doi.org/10.1016/j.ijantimicag.2015.01.001

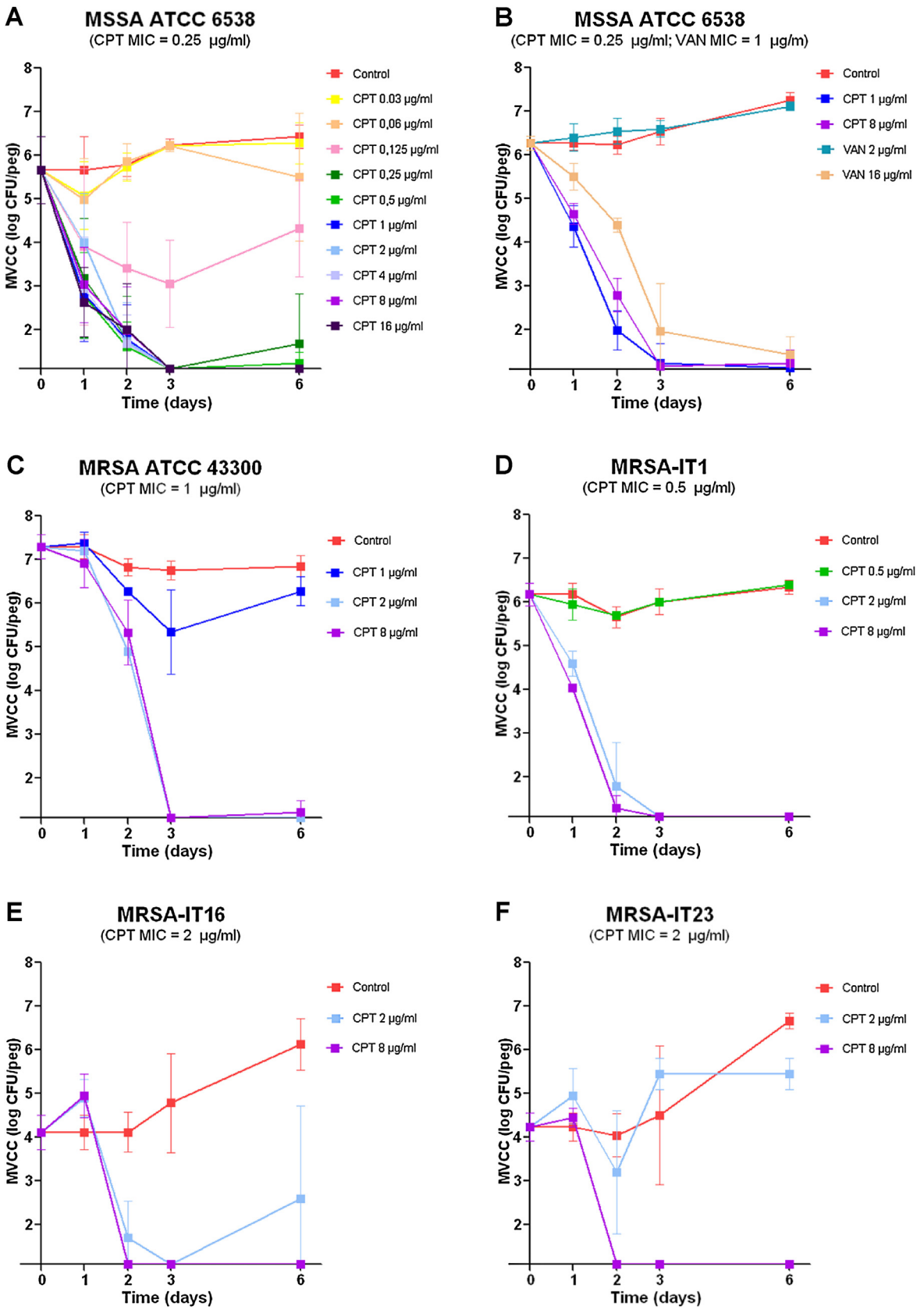

Fig. 1. Time–kill curves of *Staphylococcus aureus* biofilms exposed to ceftaroline (CPT). (A) Meticillin-susceptible *S. aureus* (MSSA) reference strain ATCC 6538 exposed to ten CPT concentrations achievable in vivo. (B) MSSA reference strain ATCC 6538 exposed to CPT or vancomycin (VAN) at 1× and 8× the susceptibility breakpoints. (C–F) Meticillin-resistant *S. aureus* (MRSA) reference strain ATCC 43300 and three MRSA clinical strains exposed to ceftaroline ≥MICs. The *x*-axis is set at the limit of detection. Error bars represent standard deviations. MVCC, mean viable cell count.

Please cite this article in press as: Landini G, et al. Bactericidal activity of ceftaroline against mature *Staphylococcus aureus* biofilms. Int J Antimicrob Agents (2015), http://dx.doi.org/10.1016/j.ijantimicag.2015.01.001

Funding: This study was supported by a research grant from AstraZeneca.
Competing interests: None declared.
Ethical approval: Not required.

Appendix A. Supplementary data

Supplementary data associated with this article can be found, in the online version, at http://dx.doi.org/10.1016/j.ijantimicag.2015.01.001.

References

[1] Kiedrowski MR, Horswill AR. New approaches for treating staphylococcal biofilm infections. Ann N Y Acad Sci 2011;1241:104–21.
[2] Saravolatz LD, Stein GE, Johnson LB. Ceftaroline: a novel cephalosporin with activity against methicillin-resistant *Staphylococcus aureus*. Clin Infect Dis 2011;52:1156–63.
[3] Barber KE, Werth BJ, McRoberts JP, Rybak MJ. A novel approach utilizing biofilm time–kill curves to assess the bactericidal activity of ceftaroline combinations against biofilm-producing methicillin-resistant *Staphylococcus aureus*. Antimicrob Agents Chemother 2014;58:2989–92.
[4] Harrison JJ, Stremick CA, Turner RJ, Allan ND, Olson ME, Ceri H. Microtiter susceptibility testing of microbes growing on peg lids: a miniaturized biofilm model for high-throughput screening. Nat Protoc 2010;5:1236–54.
[5] Abbanat D, Shang W, Amsler K, Santoro C, Baum E, Crespo-Carbone S, et al. Evaluation of the in vitro activities of ceftobiprole and comparators in staphylococcal colony or microtitre plate biofilm assays. Int J Antimicrob Agents 2014;43:32–9.

Giulia Landini
Eleonora Riccobono
Tommaso Giani
Fabio Arena
Department of Medical Biotechnologies, University of Siena, Santa Maria alle Scotte University Hospital, Viale Bracci, Siena, Italy

Gian Maria Rossolini [a,b,c]
[a] *Department of Medical Biotechnologies, University of Siena, Santa Maria alle Scotte University Hospital, Viale Bracci, Siena, Italy*
[b] *Department of Experimental and Clinical Medicine, University of Florence, Careggi University Hospital, Largo Brambilla, Florence, Italy*
[c] *Clinical Microbiology and Virology Unit, Careggi University Hospital, Largo Brambilla, Florence, Italy*

Lucia Pallecchi *
Department of Medical Biotechnologies, University of Siena, Santa Maria alle Scotte University Hospital, Viale Bracci, Siena, Italy

* Corresponding author. Present address: Department of Medical Biotechnologies, University of Siena, Santa Maria alle Scotte University Hospital, Viale Bracci, Siena 53100, Italy.
Tel.: +39 0577 233 855; fax: +39 0577 233 870.
E-mail address: lucia.pallecchi@unisi.it (L. Pallecchi)

5 January 2015

Supplementary methods: biofilm susceptibility testing

Biofilms were grown in daily refreshed brain–heart infusion broth (Oxoid, Milan, Italy) containing 0.5% glucose at 35 °C and 150 rpm for 4 days. Mature biofilms were challenged with daily refreshed antibiotic-containing cation-adjusted Mueller–Hinton broth (Oxoid) at 35 °C under static conditions for up to 6 days at ceftaroline concentrations achievable in vivo (range 0.03–16 μg/mL). The MICB (minimum inhibitory concentration of planktonic cells shed from biofilms), MBEC (minimum biofilm eradication concentration) and MVCC (mean viable cell count per peg) were determined at Days 1, 2, 3 and 6 of exposure. For MBEC and MVCC determination, biofilm cells were removed from pegs by sonication for 30 min (Elma Transsonic T 460; Elma Schmidbauer GmbH, Singen, Germany) in 200 μL of tryptic soy broth (Oxoid) supplemented with 0.1% Tween 20 (Sigma-Aldrich, Milan, Italy) (the recovery medium). The MBEC was defined as the lowest drug concentration able to prevent visible growth occurring in the recovery medium after 48 h of incubation at 35 °C. For the MVCC, 15 μL of appropriate dilutions of the recovery medium were plated onto tryptic soy agar (Oxoid) and were incubated at 35 °C for 48 h (detection limit 1.1 log CFU/peg). For each time point, positive growth controls were provided by the MVCC of at least 8 pegs (range 8–12) grown in the absence of antibiotic. Data were obtained in two independent experiments, with at least two replicates per condition per experiment.

Supplementary Table S1

Features of the *Staphylococcus aureus* isolates investigated and antibiofilm activity of ceftaroline

Strain	Origin	Antibiotic susceptibility of planktonic cells										Ceftaroline activity against mature biofilms							
		MIC [a,b]										Day 1		Day 2		Day 3		Day 6	
		CPT	ERY	CLI	CN	LEV	VAN	TEI	LZD	TGC	DPC	MICB [b]	MBEC [b]	MICB	MBEC	MICB	MBEC	MICB	MBEC
ATCC 6538	ATCC	0.25	0.25	<0.12	0.25	0.25	1	0.25	1	0.12	0.5	0.25	>16	0.25	>16	0.25	>16	0.25	>16
ATCC 43300	ATCC	1	>16	>4	>4	0.25	1	0.5	4	0.12	0.5	1	>16	1	>16	1	>16	1	>16
MRSA-IT1 [c,d]	Blood	0.5	0.5	0.25	2	8	2	4	2	0.25	4	1	>16	1	>16	1	>16	1	>16
MRSA-IT16 [d]	Wound	2	>16	>4	>4	>16	1	2	4	>1	1	2	>16	2	>16	2	>16	2	>16
MRSA-IT23 [d]	CSF	2	>16	>4	>4	>16	1	2	2	0.5	1	2	>16	2	>16	2	>16	2	>16

MIC, minimum inhibitory concentration; CPT, ceftaroline; ERY, erythromycin; CLI, clindamycin; CN, gentamicin; LEV, levofloxacin; VAN, vancomycin; TEI, teicoplanin; LZD, linezolid; TGC, tigecycline; DPC, daptomycin; MICB, minimum inhibitory concentration of planktonic cells shed from biofilms; MBEC, minimum biofilm eradication concentration; MRSA, meticillin-resistant *S. aureus*; CSF, cerebrospinal fluid.

[a] MICs were determined in triplicate using a commercial kit (TREK BMD custom panel; Thermo Fisher Scientific, Oakwood Village, OH).

[b] MICs, MICBs and MBECs are expressed in μg/mL.

[c] *Staphylococcus aureus* MRSA-IT1 was categorised as heterogeneous vancomycin-intermediate *S. aureus* (hVISA) based on the population analysis profile–area under the curve (PAP-AUC) method [1].

[d] By characterisation of staphylococcal cassette chromosome *mec* (SCC*mec*) elements [2] and staphylococcal protein A (*spa*) typing [3], the MRSA clinical strains were assigned to non-typeable *spa* type/SCC*mec* IV (MRSA-IT1), t041/SCC*mec* I (MRSA-IT16) and t288/SCC*mec* I (MRSA-IT23).

References

[1] Wootton M, Howe RA, Hillman R, Walsh TR, Bennett PM, MacGowan AP. A modified population analysis profile (PAP) method to detect hetero-resistance to vancomycin in *Staphylococcus aureus* in a UK hospital. J Antimicrob Chemother 2001;47:399–403.

[2] Kondo Y, Ito T, Ma XX, Watanabe S, Kreiswirth BN, Etienne J, et al. Combination of multiplex PCRs for staphylococcal cassette chromosome *mec* type assignment: rapid identification system for *mec*, *ccr*, and major differences in junkyard regions. Antimicrob Agents Chemother 2007;51:264–74.

[3] Harmsen D, Claus H, Witte W, Rothgänger J, Claus H, Turnwald D, et al. Typing of methicillin-resistant *Staphylococcus aureus* in a university hospital setting by using novel software for *spa* repeat determination and database management. J Clin Microbiol 2003;41:5442–8.

AAC Accepted Manuscript Posted Online 10 October 2016
Antimicrob. Agents Chemother. doi:10.1128/AAC.01334-16
Copyright © 2016 Landini et al.
This is an open-access article distributed under the terms of the Creative Commons Attribution 4.0 International license.

Accepted Manuscript Posted Online
Antimicrobial Agents and Chemotherapy
AAC
Antimicrobial Agents and Chemotherapy

Downloaded from http://aac.asm.org/ on November 24, 2016 by guest

Effect of high N-acetylcysteine concentrations on antibiotic activity against a large collection of respiratory pathogens

Giulia Landini,[1] Tiziana Di Maggio,[1] Francesco Sergio[2], Jean-Denis Docquier[1], Gian Maria Rossolini,[1,3,4,5] and Lucia Pallecchi[1#]

Department of Medical Biotechnologies, University of Siena, Siena, Italy[1]; Corporate Respiratory Medical Affairs, Zambon S.p.A., Bresso, Italy[2]; Department of Experimental and Clinical Medicine, University of Florence, Florence, Italy[3]; Clinical Microbiology and Virology Unit, Florence Careggi University Hospital, Florence, Italy[4]; Don Carlo Gnocchi Foundation, Florence, Italy[5]

Running Head: Effect of high NAC dosages on antibiotic activity

#Address correspondence to Lucia Pallecchi, lucia.pallecchi@unisi.it

Accepted Manuscript Posted Online

16 **Abstract**

17 The effect of high NAC concentrations (10 and 50 mM) on antibiotic activity against 40 strains of
18 respiratory pathogens was investigated. NAC compromised carbapenem activity (mostly imipenem
19 and, to a lesser extent, meropenem and ertapenem) in a dose-dependent fashion. Chemical
20 instability of carbapenems in the presence of NAC was demonstrated. With other antibiotics, 10
21 mM NAC had no major effects, while 50 mM NAC sporadically decreased (ceftriaxone and
22 aminoglycosides) or increased (penicillins) antibiotic activity.

Antimicrobial Agents and Chemotherapy

AAC

Antimicrobial Agents and Chemotherapy

Downloaded from http://aac.asm.org/ on November 24, 2016 by guest

Accepted Manuscript Posted Online

Antimicrobial Agents and Chemotherapy

AAC

Antimicrobial Agents and Chemotherapy

Downloaded from http://aac.asm.org/ on November 24, 2016 by guest

N-acetylcysteine (NAC) is a mucolytic agent with antioxidant and anti-inflammatory properties (1-3). Accumulating evidence points also to an intrinsic antimicrobial and anti-biofilm activity in some cases (4). Due to its properties, NAC is commonly administered together with antibiotics for the treatment of lower respiratory tract infections, and there is a growing interest in evaluating its role also in the management of cystic fibrosis (CF) and other chronic respiratory diseases (2, 5, 6).

In this perspective, it is crucial to elucidate any potential modulatory effect of NAC on antibiotic activity, which has been a matter of debate (7-12). In particular, discordant results were recently reported in two studies which investigated the effect of 10 mM NAC (i.e. 1.6 mg/ml) on the activity of some antibiotics against a few Gram-negative pathogens (including *Escherichia coli*, *Klebsiella* spp., *Pseudomonas aeruginosa*, and *Acinetobacter baumannii*). Indeed, the modulatory effect observed by Goswami *et al*. (i.e. synergism with ampicillin; antagonism with fluoroquinolones, aminoglycosides and macrolides) (10) was not confirmed by Rodríguez-Beltrán *et al*. (11), who demonstrated that the modulation of activity of fluoroquinolones and aminoglycosides was actually related to the low pH of pure NAC powder solutions and not to NAC by itself, suggesting that pH-related issues had likely contributed to the inconsistency of data from previous studies (11). In their work, Rodríguez-Beltrán *et al*. found that only the activity of imipenem was significantly affected by NAC, and proposed that for *P. aeruginosa* this antagonism was due to competitive inhibition of imipenem uptake through OprD by NAC (11).

Considering the relevance of a potential antagonistic effect of NAC on antibiotic activity, especially in case of long-term high-dosage topical administration (as should be the case for chronic respiratory diseases [4]), we performed a study to evaluate the effect of high NAC concentrations on the activity of several antibiotics against a large collection of respiratory pathogens. In this study we used both 10 and 50 mM NAC concentrations, representing the concentration tested in previous studies and a 5-fold higher concentration, respectively. The latter concentration was used since it has been suggested that concentrations of active NAC as high as 29 mM could be achieved after a

Accepted Manuscript Posted Online

Antimicrobial Agents and Chemotherapy

AAC

Antimicrobial Agents and Chemotherapy

Downloaded from http://aac.asm.org/ on November 24, 2016 by guest

single topical administration of 10% NAC (13), and even higher concentrations could be achieved by multiple-dosing regimens, by using 20% NAC for nebulization, or following direct instillation.

A total of 40 reference and clinical strains of the major bacterial species responsible for respiratory tract infections were analyzed (Table 1). MICs of the most relevant therapeutic options for the different pathogens (Table 2 and Supplemental Tables S1-S6) were determined in the absence or presence of 10 and 50 mM NAC, using the reference broth microdilution method (14). All experiments were carried out at least in duplicate. NAC stock solutions (100 mg/ml) were prepared immediately before use, by dissolving air-protected samples of NAC powder (Zambon, Bresso, Italy) in sterile double-distilled water, followed by pH adjustment at 6.5 with NaOH, and filtering through a 0.22-µm membrane filter. The stability of 200 µM imipenem, meropenem, and ertapenem solutions in the absence or presence of NAC was investigated in phosphate-buffered saline (PBS, pH 7.4) at 25°C and 37°C, and in cation-adjusted Mueller-Hinton broth (CAMHB) at 37°C. For this purpose, absorbance (wavelength, 300 nm) was recorded for up to 6 hours using an Envision microplate reader (Perkin-Elmer, Waltham, MA, USA). L-cysteine, a thiol compound known to promote carbapenem hydrolysis (14, 15), was used as a comparator in experiments performed in PBS at 25°C, and tested at the same molar concentrations. The effect of NAC on the bactericidal activity of carbapenems was investigated by time-kill assays (16), using *E. coli* ATCC 25922 as a test strain and imipenem at a concentration of 8 µg/ml.

The MICs of NAC were >16 mg/ml for all tested strains, except for the two *Haemophilus influenzae* strains which showed MICs of 16 mg/ml. In the presence of either 10 or 50 mM NAC, the MICs of most antibiotics remained within a single $\log_2$ dilution difference (i.e. the commonly accepted range of experimental reproducibility), with the notable exception of carbapenems (Fig. 1, Table 2 and Supplemental Tables S1-S6). Indeed, a clear dose-dependent inhibition of carbapenem activity by NAC was observed with all tested isolates, with imipenem being the most affected drug compared to meropenem and ertapenem (i.e. the activity of the two last carbapenems was overall preserved at 10 mM NAC) (Fig. 1 and Table 2). At the higher concentration (50 mM), NAC was

Accepted Manuscript Posted Online

Antimicrobial Agents and Chemotherapy

AAC

Antimicrobial Agents and Chemotherapy

Downloaded from http://aac.asm.org/ on November 24, 2016 by guest

also found to occasionally increase the MICs of ceftriaxone, gentamicin, and amikacin for some enterobacterial strains (Fig. 1 and Supplemental Table S1). On the other hand, 50 mM NAC was found to decrease the MICs of penicillin and amoxicillin-clavulanic acid for both *Corynebacterium striatum* strains, and the MIC of piperacillin-tazobactam for one *Klebsiella pneumoniae* strain (Fig. 1 and Supplemental Tables S1 and S6). Time-kill assays confirmed a dose-dependent inhibition by NAC of the bactericidal activity of imipenem against *E. coli* ATCC 25922 (Fig. 2).

Although carbapenems were significantly more stable in the presence of NAC (in which the nucleophilicity of the thiol group is reduced by the addition of an N-acetyl substituent) than of L-cysteine (Supplemental Table S7), their stability in PBS or in CAMHB was consistently affected in the presence of 10 or 50 mM NAC (Table 2 and Supplemental Table S7). Notably, imipenem was less stable than meropenem or ertapenem in all tested conditions (Table 2 and Supplemental Table S7). Temperature and medium impacted on NAC-mediated carbapenem inactivation, with a more rapid inactivation observed at 37°C *vs.* 25°C, and in CAMHB *vs.* PBS (Supplemental Table S7). Overall, these data were consistent with the impact of NAC on carbapenem MIC values (Fig. 1 and Table 2). Nonetheless, some heterogeneity in the antagonistic effect of NAC for carbapenems was observed among tested strains, suggesting that additional mechanisms could contribute to the observed NAC-mediated increase of carbapenem MICs, including issues related to carbapenems permeability, as previously suggested for *P. aeruginosa* (11).

In conclusion, the results of the present study demonstrated that high NAC concentrations (possibly reached in the airways following topical administration) overall do not interfere with the activity of the most commonly used antibiotics, with the exception of carbapenems. The instability of imipenem and, to a lesser extent, of meropenem and ertapenem in the presence of high NAC concentrations was found to be a major mechanism accounting for the antagonistic interaction with carbapenems. However, considering that the MICs of meropenem and ertapenem for susceptible strains mostly remained below the susceptibility breakpoints even in the presence of 50 mM NAC, the negative interaction of NAC with these drugs might not be clinically relevant and warrants

Accepted Manuscript Posted Online

further evaluation. Some modulatory effect on the activity of other beta-lactams and aminoglycosides was also observed at the highest NAC concentration tested with some strains, resulting in either a synergistic or antagonistic interaction. Interestingly, NAC showed an intrinsic antimicrobial activity against *H. influenzae*, which would deserve further investigation.

Downloaded from http://aac.asm.org/ on November 24, 2016 by guest

Antimicrobial Agents and Chemotherapy
AAC
Antimicrobial Agents and Chemotherapy

Accepted Manuscript Posted Online

Acknowledgments

This work was funded by a research grant from Zambon S.p.A.. We thank Pei-Fang Hsieh and Jin-Town Wang for providing us with the *K. pneumoniae* NTUH-K2044 strain.

Downloaded from http://aac.asm.org/ on November 24, 2016 by guest

Antimicrobial Agents and Chemotherapy
AAC
Antimicrobial Agents and Chemotherapy

Accepted Manuscript Posted Online

Antimicrobial Agents and Chemotherapy

AAC

Antimicrobial Agents and Chemotherapy

Downloaded from http://aac.asm.org/ on November 24, 2016 by guest

References

1. **Hurst GA, Shaw PB, LeMaistre CA.** 1967. Laboratory and clinical evaluation of the mucolytic properties of acetylcysteine. Am Rev Respir Dis **96:**962-970.
2. **Rushworth GF, Megson IL.** 2014. Existing and potential therapeutic uses for N-acetylcysteine: the need for conversion to intracellular glutathione for antioxidant benefits. Pharmacol Ther **141:**150-159.
3. **Samuni Y, Goldstein S, Dean OM, Berk M.** 2013. The chemistry and biological activities of N-acetylcysteine. Biochim Biophys Acta **1830:**4117-4129.
4. **Blasi F, Pave C, Rossolini GM, Pallecchi L, Matera MG, Rogliani P, Cazzola M.** 2016. The effect of N-acetylcysteine on biofilms: implications for the treatment of respiratory tract infections. Respir Med **117**:190-197.
5. **Cazzola M, Calzetta L, Page C, Jardim J, Chuchalin AG, Rogliani P, Matera MG.** 2015. Influence of N-acetylcysteine on chronic bronchitis or COPD exacerbations: a meta-analysis. Eur Respir Rev **24:**451-461.
6. **Skov M, Pressler T, Lykkesfeldt J, Poulsen HE, Jensen PØ, Johansen HK, Qvist T, Kræmer D, Høiby N, Ciofu O.** 2015. The effect of short-term, high-dose oral N-acetylcysteine treatment on oxidative stress markers in cystic fibrosis patients with chronic *P. aeruginosa* infection - a pilot study. J Cyst Fibros **14:**211-218.
7. **Parry MF, Neu HC.** 1977. Effect of N-acetylcysteine on antibiotic activity and bacterial growth *in vitro*. J Clin Microbiol **5**:58-61.
8. **Roberts D, Cole P.** 1981. N-acetylcysteine potentiates the anti-pseudomonas activity of carbenicillin *in vitro*. J Infect **3**:353-359.
9. **Alfredsson H, Malmborg AS, Strandvik B.** 1987. N-acetylcysteine and 2-mercaptoethane sulphonate inhibit anti-pseudomonas activity of antibiotics *in vitro*. Eur J Respir Dis **70**:213-217.

Accepted Manuscript Posted Online

10. **Goswami M, Jawali N.** 2010. N-acetylcysteine-mediated modulation of bacterial antibiotic susceptibility. Antimicrob Agents Chemother **54:**3529-3350.

11. **Rodríguez-Beltrán J, Cabot G, Valencia EY, Costas C, Bou G, Oliver A, Blázquez J.** 2015. N-acetylcysteine selectively antagonizes the activity of imipenem in *Pseudomonas aeruginosa* by an OprD-mediated mechanism. Antimicrob Agents Chemother **59:**3246-3251.

12. **Yang F, Liu LH, Li XP, Luo JY, Zhang Z, Yan ZT, Zhang SD, Li HS.** 2016. Short communication: N-Acetylcysteine-mediated modulation of antibiotic susceptibility of bovine mastitis pathogens. J Dairy Sci **99**:4300-4302.

13. **Szkudlarek U, Zdziechowski A, Witkowski K, Kasielski M, Luczyńska M, Luczyński R, Sarniak A, Nowak D.** 2004. Effect of inhaled N-acetylcysteine on hydrogen peroxide exhalation in healthy subjects. Pulm Pharmacol Ther **17:**155-162.

14. **Clinical and Laboratory Standards Institute**. 2015 Methods for dilution antimicrobial susceptibility tests for bacteria that grow aerobically: approved standard – tenth edition (M07-A10). Clinical and Laboratory Standards Institute, Wayne, PA.

15. **Jones RN, Critchley IA, Whittington WL, Janjic N, Pottumarthy S.** 2005. Activity of faropenem tested against *Neisseria gonorrhoeae* isolates including fluoroquinolone-resistant strains. Diagn Microbiol Infect Dis **53:**311-317.

16. **Clinical and Laboratory Standards Institute**. 1999. Methods for determining bactericidal activity of antimicrobial agents; approved guidelines (M26-A). Clinical and Laboratory Standards Institute, Wayne, PA.

17. **Wu KM, Li LH, Yan JJ, Tsao N, Liao TL, Tsai HC, Fung CP, Chen HJ, Liu YM, Wang JT, Fang CT, Chang SC, Shu HY, Liu TT, Chen YT, Shiau YR, Lauderdale TL, Su IJ, Kirby R, Tsai SF.** 2009. Genome sequencing and comparative analysis of *Klebsiella pneumoniae* NTUH-K2044, a strain causing liver abscess and meningitis. J Bacteriol **191:**4492-4501.

Antimicrobial Agents and Chemotherapy

AAC

Antimicrobial Agents and Chemotherapy

Downloaded from http://aac.asm.org/ on November 24, 2016 by guest

Accepted Manuscript Posted Online

18. **Stover CK, Pham XQ, Erwin AL, Mizoguchi SD, Warrener P, Hickey MJ, Brinkman FS, Hufnagle WO, Kowalik DJ, Lagrou M, Garber RL, Goltry L, Tolentino E, Westbrock-Wadman S, Yuan Y, Brody LL, Coulter SN, Folger KR, Kas A, Larbig K, Lim R, Smith K, Spencer D, Wong GK, Wu Z, Paulsen IT, Reizer J, Saier MH, Hancock RE, Lory S, Olson MV.** 2000. Complete genome sequence of *Pseudomonas aeruginosa* PAO1, an opportunistic pathogen. Nature **406:**959-964.

19. **Diancourt L, Passet V, Nemec A, Dijkshoorn L, Brisse S.** 2010. The population structure of *Acinetobacter baumannii*: expanding multiresistant clones from an ancestral susceptible genetic pool. PLoS One **5**:e10034. doi:10.1371/journal.pone.0010034.

20. **Landini G, Riccobono E, Giani T, Arena F, Rossolini GM, Pallecchi L.** 2015. Bactericidal activity of ceftaroline against mature *Staphylococcus aureus* biofilms. Int J Antimicrob Agents **45:**551-553.

Antimicrobial Agents and Chemotherapy
AAC
Antimicrobial Agents and Chemotherapy
Downloaded from http://aac.asm.org/ on November 24, 2016 by guest

Accepted Manuscript Posted Online

Antimicrobial Agents and Chemotherapy

AAC

Antimicrobial Agents and Chemotherapy

Downloaded from http://aac.asm.org/ on November 24, 2016 by guest

170 **Figure Legends**

171

172 **Figure 1.** Schematic representation of the effect of two high NAC concentrations (10 mM and 50
173 mM) on antibiotic activity against a collection of respiratory pathogens. A modulatory effect on
174 antibiotic activity was defined as a MIC modification of at least 2 $\log_2$ dilutions. The number of
175 strains tested for each antibiotic is indicated in brackets, while details on bacterial species and MIC
176 results are reported in Table 1, Table 2 and Supplemental Tables S1-S6. In order to express the
177 results as $\log_2$ dilution variations, a value corresponding to the lowest or to twice that of the highest
178 antibiotic concertation tested was assigned to MICs that could not be determined because of out of
179 range of antibiotic concentrations used. This is particularly relevant for MICs of imipenem in the
180 presence of 50 mM NAC, which was >64 µg/ml for the majority of isolates tested. PEN, penicillin;
181 AMX, amoxicillin; OXA, oxacillin; AMC, amoxicillin clavulanic acid; TZP, piperacillin-
182 tazobactam; CRO, ceftriaxone; CTX, cefotaxime; CAZ, ceftazidime; IMP, imipenem; MEM,
183 meropenem; ERT, ertapenem; GEN, gentamicin; AMK, amikacin; TOB, tobramycin; LVX,
184 levofloxacin; SXT, trimethoprim-sulfamethoxazole; AZM, azithromycin; MIN, minocycline; VAN,
185 vancomycin; LZD, linezolid; CST, colistin. The box-and-whiskers plot (i.e. box extended from 25th
186 to 75th percentiles, and whiskers indicating the minimum and maximum values) was generated by
187 GraphPad Prism 5 (GraphPad, La Jolla, CA).

188

189 **Figure 2.** Time-kill curves of imipenem (8 µg/ml) alone and in combination with 10 and 50 mM
190 NAC against *E. coli* ATCC 25922. The *x* axis has been set at the experimental detection limit (1.5
191 log CFU/ml).

Accepted Manuscript Posted Online

192 **TABLE 1** Origin and main features of the 40 strains included in the study

Strain	Origin and main features
E. coli ATCC 25922	ATCC reference strain
E. coli Z21	Cystic fibrosis (2-year lung colonization), ESBL-positive, ST131 clinical isolate
E. coli Z24	Cystic fibrosis clinical isolate
E. coli Z25	Lower respiratory tract infection, ESBL-positive, KPC-positive clinical isolate
K. pneumoniae ATCC 700603	ATCC ESBL-positive reference strain
K. pneumoniae NTUH-K2044	Liver abscess and meningitis, capsular serotype K1, hypermucoviscous (17)
K. pneumoniae CIP 52.145	CIP reference strain, capsular serotype K2, hypermucoviscous
K. pneumoniae Z4	Cystic fibrosis (1-year lung colonization), ESBL-positive, AmpC-positive clinical isolate
K. pneumoniae Z11	Lower respiratory tract infection, KPC-positive clinical isolate
K. oxytoca CCUG 15717^T	CCUG type strain
E. cloacae CIP 6085^T	CIP type strain
E. cloacae Z16	Cystic fibrosis, ESBL-positive clinical isolate
E. cloacae Z17	Lower respiratory tract infection clinical isolate
E. cloacae Z18	Lower respiratory tract infection clinical isolate
E. cloacae Z19	Lower respiratory tract infection clinical isolate
P. aeruginosa ATCC 27853	ATCC reference strain
P. aeruginosa PAO-1	*P. aeruginosa* reference strain (18)
P. aeruginosa Z32	Lower respiratory tract infection clinical isolate
P. aeruginosa Z34	Cystic fibrosis (3-year lung colonization) clinical isolate
P. aeruginosa Z38	Acute bacterial rhinosinusitis clinical isolate
A. baumannii ATCC 17978	ATCC reference strain
A. baumannii RUH 134	Reference strain for the global clone 2 (19)
M. catarrhalis Z72	Lower respiratory tract infection clinical isolate
M. catarrhalis Z73	Lower respiratory tract infection clinical isolate
H. influenzae ATCC 49247	ATCC reference strain
H. influenzae Z83	Lower respiratory tract infection clinical isolate
S. aureus ATCC 25923	ATCC reference MSSA strain
S. aureus ATCC 6538	ATCC reference MSSA strain
S. aureus ATCC 43300	ATCC reference MRSA strain
S. aureus MRSA-IT1	Bloodstream infection, MRSA, hVISA (20)
S. aureus Z57	Acute bacterial rhinosinusitis, MSSA clinical isolate
S. aureus Z61	Lower respiratory tract infection, MSSA clinical isolate
S. pyogenes ATCC 12344^T	ATCC type strain
S. pyogenes Z90	Lower respiratory tract infection clinical isolate
S. pyogenes Z91	Cellulitis clinical isolate
S. pneumoniae ATCC 49619	ATCC reference strain
S. pneumoniae Z104	Lower respiratory tract infection clinical isolate
S. pneumoniae Z105	Lower respiratory tract infection clinical isolate

Antimicrobial Agents and Chemotherapy
AAC
Antimicrobial Agents and Chemotherapy
Downloaded from http://aac.asm.org/ on November 24, 2016 by guest

Accepted Manuscript Posted Online

C. striatum Z114	Lower respiratory tract infection clinical isolate
C. striatum Z115	Lower respiratory tract infection clinical isolate

When available, main features concerning resistance determinants and molecular typing were reported. ATCC, American Type Culture Collection; CIP, Collection Institut Pasteur; CCUG, Culture Collection University of Goteborg; ESBL, extended-spectrum beta-lactamase; KPC, KPC-type beta-lactamase; AmpC, AmpC-like beta lactamase; MSSA, methicillin-susceptible *S. aureus*; MRSA, methicillin-resistant *S. aureus*; hVISA, heterogeneous vancomycin-intermediate *S. aureus*.

Antimicrobial Agents and Chemotherapy

AAC

Antimicrobial Agents and Chemotherapy

Downloaded from http://aac.asm.org/ on November 24, 2016 by guest

Accepted Manuscript Posted Online

199 **TABLE 2** MICs (μg/ml) of carbapenems in the absence and presence of NAC for a panel of
200 respiratory pathogens

Antibiotic	IMP			MEM			ERT		
NAC (mM)	0	10	50	0	10	50	0	10	50
$t_{1/2}$ value (min)	>1000	200 ± 40	52 ± 6	>1000	670 ± 160	145 ± 15	>1000	>1000	225 ± 20
E. coli ATCC 25922	0.125	2	>64	≤0.03	≤0.03	0.5	≤0.015	≤0.015	0.06
E. coli Z21	0.25	1	32	0.06	0.06	0.5	0.125	0.125	0.25
E. coli Z24	0.25	0.5	64	≤0.03	≤0.03	0.25	0.03	0.03	0.125
E. coli Z25	4	8	>64	4	2	2	4	4	2
K. pneumoniae ATCC 700603	0.25	1	>64	≤0.03	0.06	0.25	0.06	0.125	0.125
K. pneumoniae NTUHK2044	0.25	2	>64	≤0.03	0.06	0.25	≤0.015	0.03	0.06
K. pneumoniae CIP 52.145	0.5	2	64	≤0.03	0.06	0.25	≤0.015	0.03	0.125
K. pneumoniae Z4	0.25	2	>64	≤0.03	0.06	0.5	0.5	1	2
K. pneumoniae Z11	8	16	>64	8	4	4	>32	32	32
K. oxytoca CCUG 15717^T	0.5	2	>64	≤0.03	0.06	1	≤0.015	0.03	0.06
E. cloacae CIP 6085^T	0.5	2	>64	0.125	0.125	0.25	0.5	1	1
E. cloacae Z16	1	4	>64	0.25	0.25	0.5	2	4	4
E. cloacae Z17	1	4	32	0.125	0.125	0.25	0.06	0.25	0.25
E. cloacae Z18	1	2	>64	0.06	0.125	0.25	0.125	0.25	0.25
E. cloacae Z19	0.5	2	>64	0.125	0.125	0.5	2	2	4
P. aeruginosa PAO-1	2	16	64	1	2	4	nd	nd	nd
P. aeruginosa ATCC 27853	2	8	>64	1	1	2	nd	nd	nd
P. aeruginosa Z32	4	32	>64	32	32	64	nd	nd	nd
P. aeruginosa Z34	32	64	>64	8	16	32	nd	nd	nd
P. aeruginosa Z38	2	8	>64	≤0.03	0.06	0.5	nd	nd	nd
A. baumannii ATCC 17978	0.25	4	64	0.25	1	1	nd	nd	nd
A. baumannii RUH 134	0.5	8	>64	1	2	1	nd	nd	nd
S. aureus ATCC 25923	≤0.03	0.25	16	nd	nd	nd	nd	nd	nd
S. aureus ATCC 6538	≤0.03	0.5	16	nd	nd	nd	nd	nd	nd
C. striatum Z114	0.25	16	32	nd	nd	nd	nd	nd	nd
C. striatum Z115	8	64	>64	nd	nd	nd	nd	nd	nd

201

202 IMP, imipenem; MEM, meropenem; ERT, ertapenem; nd, not determined (the species is
203 intrinsically resistant, or breakpoints are lacking, or the drug is not a preferred option for that
204 species). MIC changes by more than one 2-fold dilution in the presence of NAC are shaded. Half-
205 life values [$t_{1/2}$] of carbapenems solutions in CAMHB (37°C) in the absence or presence of NAC
206 have also been reported.

Downloaded from http://aac.asm.org/ on November 24, 2016 by guest

Antimicrobial Agents and Chemotherapy
AAC
Antimicrobial Agents and Chemotherapy

Accepted Manuscript Posted Online
Antimicrobial Agents and Chemotherapy
AAC
Antimicrobial Agents and Chemotherapy

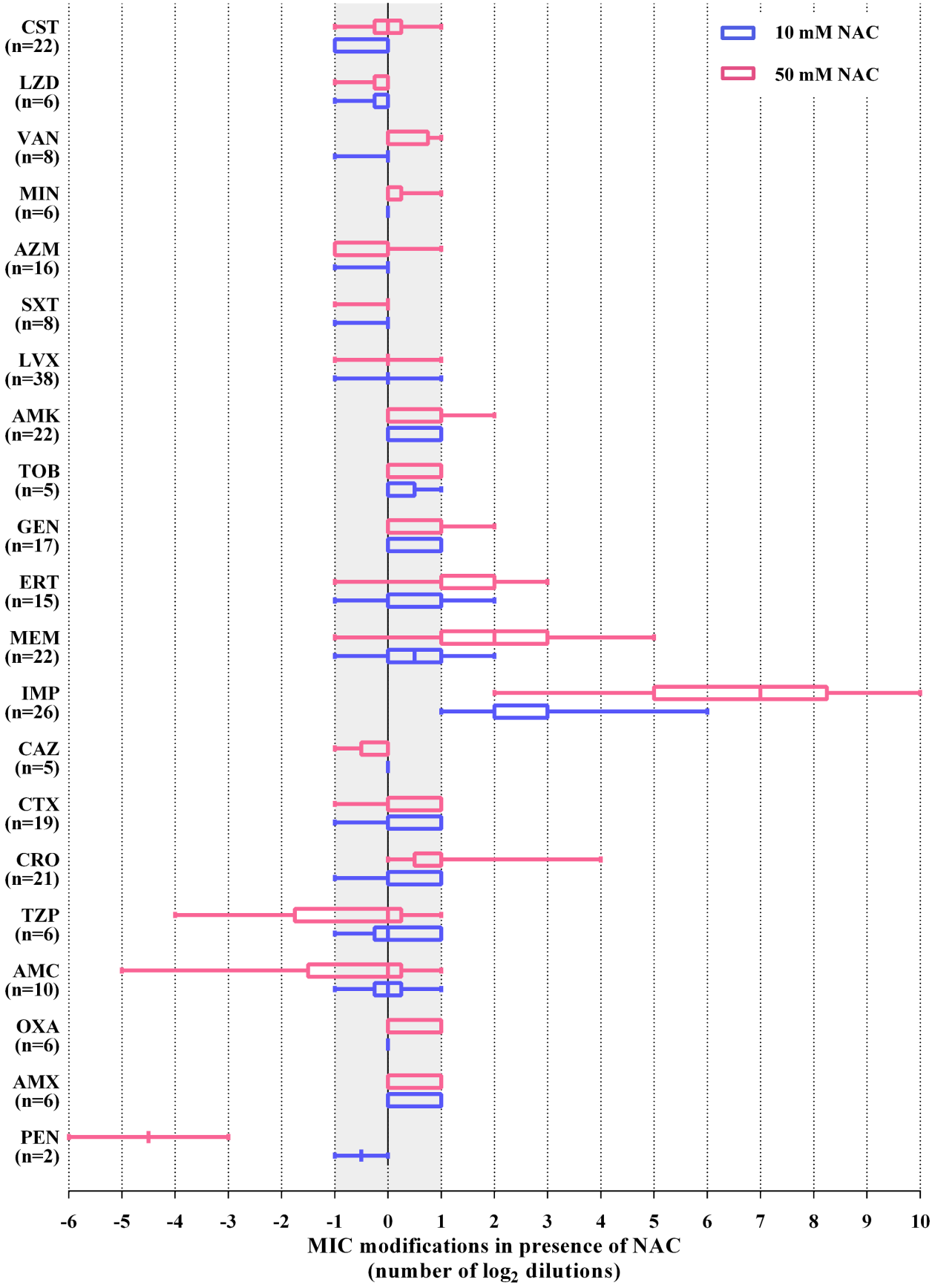

Downloaded from http://aac.asm.org/ on November 24, 2016 by guest

Accepted Manuscript Posted Online

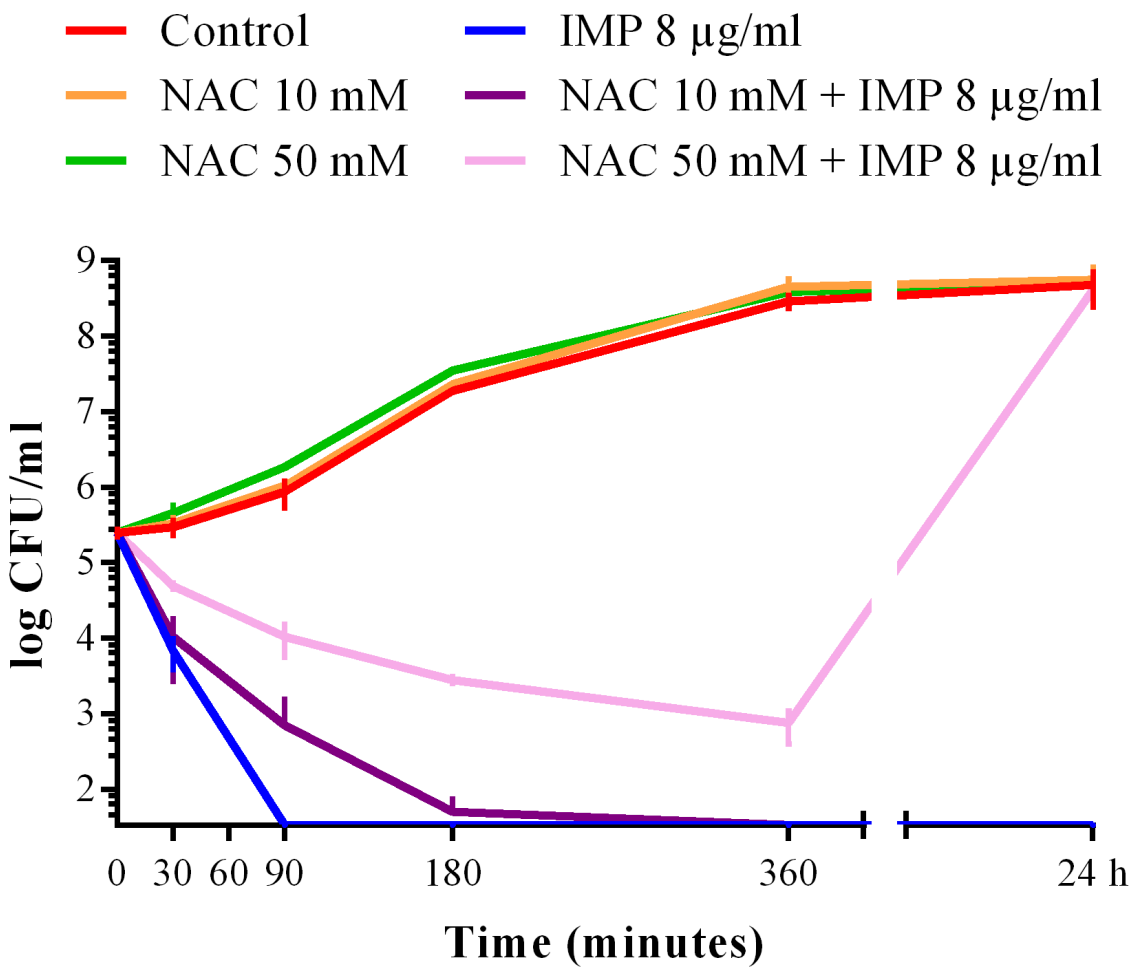

Downloaded from http://aac.asm.org/ on November 24, 2016 by guest

Antimicrobial Agents and Chemotherapy
AAC
Antimicrobial Agents and Chemotherapy

SUPPLEMENTAL TABLE S1 MICs (μg/ml) of antibiotics other than carbapenems, determined in absence and presence of two high NAC concentrations: *Enterobacteriaceae*

Antibiotic	AMC			TZP			CTX			CRO			GEN			AMK			LVX			CST		
NAC (mM)	0	10	50	0	10	50	0	10	50	0	10	50	0	10	50	0	10	50	0	10	50	0	10	50
E. coli ATCC 25922	8	16	16	nd	nd	nd	0.06	0.125	0.06	0.06	0.06	0.25	1	1	1	1	2	2	≤0.03	≤0.03	≤0.03	0.5	0.5	0.5
E. coli Z21	64	64	64	nd	nd	nd	>512	>512	>512	>512	>512	>512	2	4	4	16	32	32	64	64	32	1	0.5	0.5
E. coli Z24	8	8	8	nd	nd	nd	0.25	0.125	0.25	0.125	0.125	1	2	2	2	8	16	16	64	64	64	0.5	0.5	0.5
E. coli Z25	>64	64	>64	nd	nd	nd	>512	>512	>512	>512	>512	>512	>256	>256	>256	32	32	64	16	16	16	1	0.5	0.5
Kp ATCC 700603	nd	nd	nd	16	16	8	4	8	4	4	8	8	8	16	16	1	2	2	1	0.5	1	1	1	1
Kp NTUH-K2044	nd	nd	nd	2	4	2	0.06	0.06	0.125	0.06	0.06	0.125	0.25	0.5	1	2	2	4	0.06	0.125	0.06	0.5	0.5	1
Kp CIP 52.145	nd	nd	nd	2	2	2	0.06	0.06	0.06	0.06	0.06	0.25	0.25	0.5	1	1	2	4	0.06	0.06	0.06	0.5	0.5	1
Kp Z4	nd	nd	nd	64	128	128	512	>512	512	>512	>512	>512	>256	>256	>256	>64	>64	>64	1	1	1	0.5	0.5	1
Kp Z11	nd	nd	nd	>256	256	32	64	64	128	64	64	128	4	8	8	32	64	64	64	32	32	1	0.5	1
K. oxytoca CCUG 15717^T	nd	nd	nd	4	4	4	0.06	0.06	0.06	0.125	0.25	0.25	1	2	1	2	4	4	0.06	0.06	0.06	0.5	0.5	0.5
E. cloacae CIP 6085^T	nd	nd	nd	nd	nd	nd	8	8	4	8	4	16	0.5	1	1	1	2	2	≤0.03	≤0.03	≤0.03	64	64	64
E. cloacae Z16	nd	nd	nd	nd	nd	nd	256	512	512	512	>512	>512	>256	>256	>256	>64	>64	>64	0.5	0.5	0.5	1	0.5	2
E. cloacae Z17	nd	nd	nd	nd	nd	nd	0.06	0.125	0.125	0.06	0.125	1	0.5	0.5	1	0.5	1	1	≤0.03	≤0.03	≤0.03	64	64	32
E. cloacae Z18	nd	nd	nd	nd	nd	nd	0.25	0.25	0.125	0.5	0.5	1	0.5	1	2	2	2	4	0.06	0.06	0.06	0.5	0.5	0.5
E. cloacae Z19	nd	nd	nd	nd	nd	nd	256	256	128	512	>512	>512	256	>256	>256	1	2	2	32	32	32	0.5	0.5	1

Kp, *Klebsiella pneumoniae*; AMC, amoxicillin-clavulanic acid; TZP, piperacillin-tazobactam; CTX, cefotaxime; CRO, ceftriaxone; GEN, gentamicin; AMK, amikacin; LVX, levofloxacin; CST, colistin; nd, not determined. MIC changes by more than one 2-fold dilution in the presence of NAC are shaded.

SUPPLEMENTAL TABLE S2 MICs (μg/ml) of antibiotics other than carbapenems, determined in absence and presence of two high NAC concentrations: *Pseudomonas aeruginosa* and *Acinetobacter baumannii*

Antibiotic	CAZ			TOB			AMK			LVX			CST		
NAC (mM)	0	10	50	0	10	50	0	10	50	0	10	50	0	10	50
P. aeruginosa PAO-1	0.5	0.5	0.5	0.25	0.5	0.5	1	2	2	1	1	1	2	2	2
P. aeruginosa ATCC 27853	1	1	1	0.5	0.5	0.5	2	2	2	1	1	1	2	1	1
P. aeruginosa Z32	8	8	8	0.5	0.5	0.5	1	1	1	2	1	1	0.5	0.5	0.5
P. aeruginosa Z34	128	128	64	32	32	32	16	16	16	8	8	4	2	1	1
P. aeruginosa Z38	1	1	1	0.5	0.5	1	2	4	4	0.125	0.125	0.125	1	1	1
A. baumannii ATCC 17978	nd	nd	nd	nd	nd	nd	2	2	2	0.25	0.25	0.125	1	1	1
A. baumannii RUH 134	nd	nd	nd	nd	nd	nd	4	4	4	0.25	0.25	0.25	1	1	1

CAZ, ceftazidime; TOB, tobramycin; AMK, amikacin; LVX, levofloxacin; CST, colistin; nd, not determined.

SUPPLEMENTAL TABLE S3 MICs (µg/ml) of antibiotics determined in absence and presence of two high NAC concentrations: *Moraxella catarrhalis* and *Haemophilus influenzae*

Antibiotic	AMC			CTX			LVX			AZM			SXT		
NAC (mM)	0	10	50	0	10	50	0	10	50	0	10	50	0	10	50
M. catarrhalis Z72	0.5	0.5	1	0.5	0.5	0.5	0.06	0.06	0.06	0.06	0.06	0.03	nd	nd	nd
M. catarrhalis Z73	0.25	0.25	0.125	0.25	0.25	0.5	0.06	0.06	0.06	0.06	0.03	0.03	nd	nd	nd
H. influenzae ATCC 49247	8	8	8	0.5	0.5	1	0.03	0.03	0.03	nd	nd	nd	0.125	0.125	0.125
H. influenzae Z83	1	2	1	0.125	0.125	0.25	0.015	0.03	0.03	nd	nd	nd	>16	>16	>16

AMC, amoxicillin-clavulanic acid; CTX, cefotaxime; LVX, levofloxacin; AZM, azithromycin; SXT, trimethoprim-sulfamethoxazole; nd, not determined.

SUPPLEMENTAL TABLE S4 MICs (μg/ml) of antibiotics other than carbapenems, determined in absence and presence of two high NAC concentrations:

Staphylococcus aureus

Antibiotic	OXA			LVX			SXT			AZM			MIN			VAN			LZD		
NAC (mM)	0	10	50	0	10	50	0	10	50	0	10	50	0	10	50	0	10	50	0	10	50
S. aureus ATCC 6538	0.125	0.125	0.25	0.125	0.25	0.125	0.125	0.125	0.125	1	1	0.5	0.06	0.06	0.06	1	1	2	2	2	2
S. aureus ATCC 25923	0.25	0.25	0.25	0.25	0.25	0.25	0.125	0.06	0.06	1	1	0.5	0.125	0.125	0.125	2	2	2	2	2	2
S. aureus ATCC 43300	16	16	32	0.25	0.25	0.25	0.125	0.125	0.125	>256	>256	>256	0.06	0.06	0.06	1	1	2	2	2	2
S. aureus MRSA-IT1	8	8	8	8	8	8	0.125	0.125	0.125	2	2	1	0.06	0.06	0.06	2	2	2	4	2	2
S. aureus Z57	0.5	0.5	0.5	0.125	0.125	0.125	0.125	0.125	0.125	1	1	1	0.06	0.06	0.125	1	1	1	4	4	4
S. aureus Z61	0.5	0.5	0.5	0.125	0.125	0.125	0.125	0.125	0.125	2	2	2	0.125	0.125	0.125	2	1	2	4	4	4

OXA, oxacillin; LVX, levofloxacin; SXT, trimethoprim-sulfamethoxazole; AZM, azithromycin; MIN, minocycline; VAN, vancomycin; LZD, linezolid.

SUPPLEMENTAL TABLE S5 MICs (μg/ml) of antibiotics determined in absence and presence of two high NAC concentrations: *Streptococcus pyogenes* and *Streptococcus pneumoniae*

Antibiotic	AMX			CRO			LVX			AZM		
NAC (mM)	0	10	50	0	10	50	0	10	50	0	10	50
S. pyogenes ATCC 12344^T	0.03	0.03	0.03	0.03	0.03	0.03	0.5	0.5	0.5	0.125	0.125	0.125
S. pyogenes Z90	≤0.008	0.015	0.015	0.015	0.03	0.03	0.5	0.5	0.5	0.125	0.125	0.125
S. pyogenes Z91	0.015	0.03	0.015	0.015	0.03	0.03	0.5	0.5	0.5	0.25	0.125	0.25
S. pneumoniae ATCC 49619	0.06	0.125	0.125	0.125	0.125	0.125	0.5	0.5	0.5	0.06	0.06	0.125
S. pneumoniae Z104	0.015	0.03	0.03	0.03	0.06	0.06	1	1	1	32	32	32
S. pneumoniae Z105	≤0.008	≤0.008	0.015	0.06	0.06	0.125	1	1	1	32	32	32

AMX, amoxicillin; CRO, ceftriaxone; LVX, levofloxacin; AZM, azithromycin. MICs values were always confirmed by CFU count, required due to the alteration of culture medium (containing 5% lysed horse blood) color in the presence of high NAC concentrations.

SUPPLEMENTAL TABLE S6 MICs (µg/ml) of antibiotics other than carbapenems, determined in absence and presence of two high NAC concentrations: *Corynebacterium striatum*

Antibiotic	PEN			AMC			GEN			AZM			VAN		
NAC (mM)	0	10	50	0	10	50	0	10	50	0	10	50	0	10	50
C. striatum Z114	2	2	0.25	2	2	0.25	8	8	16	>32	>32	>32	0.5	0.5	0.5
C. striatum Z115	32	16	0.5	32	16	1	4	4	8	>32	>32	>32	0.5	0.5	0.5

PEN, penicillin; AMC, amoxicillin-clavulanic acid; GEN, gentamicin; AZM, azithromycin; VAN, vancomycin. MIC changes by more than one 2-fold dilution in the presence of NAC are shaded. MICs values were always confirmed by CFU count, required due to the alteration of culture medium (containing 5% lysed horse blood) color in the presence of high NAC concentrations.

SUPPLEMENTAL TABLE S7 Stability of carbapenems in the presence of NAC.

Compound (experimental conditions)	Antibiotic $t_{1/2}$ (min)		
	Imipenem	Meropenem	Ertapenem
None (PBS, 25°C)	>1000	>1000	>1000
10 mM L-cysteine (PBS, 25°C)	9.5 ± 0.1	10.4 ± 0.1	21.3 ± 0.5
50 mM L-cysteine (PBS, 25°C)	6.3 ± 0.4	3.8 ± 0.1	7.5 ± 0.7
10 mM NAC (PBS, 25°C)	580 ± 9	>1000	>1000
50 mM NAC (PBS, 25°C)	160 ± 2	500 ± 8	>1000
None (PBS, 37°C)	>1000	>1000	>1000
10 mM NAC (PBS, 37°C)	550 ± 30	>1000	>1000
50 mM NAC (PBS, 37°C)	66 ± 5	220 ± 30	530 ± 40
None (CAMHB, 37°C)	>1000	>1000	>1000
10 mM NAC (CAMHB, 37°C)	200 ± 40	670 ± 160	>1000
50 mM NAC (CAMHB, 37°C)	52 ± 6	145 ± 15	225 ± 20

The half-life ($t_{1/2}$) of antibiotics was computed from the pseudo-first order rate constant for carbapenem beta-lactam ring opening, measured by following the time-dependence variation of absorbance at 300 nm (values are the mean of four independent experiments), followed in both PBS buffer and in cation-adjusted Mueller-Hinton Broth (CAMHB) and at 25 or 37 °C. L-cysteine was tested as a comparator in experiments performed at 25°C in PBS.

Nanomedicine: Nanotechnology, Biology, and Medicine
11 (2015) 1417–1423

nanomedicine
Nanotechnology, Biology, and Medicine

nanomedjournal.com

Highly bactericidal Ag nanoparticle films obtained by cluster beam deposition

Emanuele Cavaliere, Ph.D.[a], Sebastiano De Cesari, M.S.[a], Giulia Landini, MS[b], Eleonora Riccobono, Ph.D.[b], Lucia Pallecchi, Ph.D.[b], Gian Maria Rossolini, M.D.[b,c], Luca Gavioli, Ph.D. Physics[a,*]

[a]*Interdisciplinary Laboratories for Advanced Material Physics (i-LAMP) & Dipartimento di Matematica e Fisica, Università Cattolica del Sacro Cuore di Brescia, Brescia, Italy*

[b]*Dipartimento di Biotecnologie Mediche, Università degli Studi di Siena, Policlinico Santa Maria alle Scotte, Siena, Italy*

[c]*Dipartimento di Medicina Sperimentale e Clinica, Università di Firenze & SOD Microbiologia e Virologia, Azienda Ospedaliera Universitaria Careggi, Firenze, Italy*

Received 4 December 2014; accepted 28 February 2015

Abstract

The recent emergence of bacterial pathogens resistant to most or all available antibiotics is among the major global public health problems. As indirect transmission through contaminated surfaces is a main route of dissemination for most of such pathogens, the implementation of effective antimicrobial surfaces has been advocated as a promising approach for their containment, especially in the hospital settings. However, traditional wet synthesis methods of nanoparticle-based antimicrobial materials leave a number of key points open for metal surfaces: such as adhesion to the surface and nanoparticle coalescence. Here we demonstrate an alternative route, i.e. supersonic cluster beam deposition, to obtain antimicrobial Ag nanoparticle films deposited directly on surfaces. The synthesized films are simple to produce with controlled density and thickness, are stable over time, and are shown to be highly bactericidal against major Gram positive and Gram negative bacterial pathogens, including extensively drug-resistant strains.

© 2015 The Authors. Published by Elsevier Inc. This is an open access article under the CC BY-NC-ND license (http://creativecommons.org/licenses/by-nc-nd/4.0/).

Key words: Ag nanoparticle-based antimicrobial films; Supersonic cluster beam deposition; Atomic force microscopy; Electron spectroscopies; Bactericidal activity; Extensively drug-resistant bacteria

Backgrounds

Nanoparticles (NPs) are promising alternatives to conventional materials in many branches of science and technology[1-3] since the nanoscale allows to access physical properties and functionalities that often differ significantly from their bulk counterparts. As an example, the antimicrobial activity of nanomaterials such as fullerenes, TiO_2, and Ag NPs has a wide range of important applications in medicine, water disinfection, and consumer products (e.g. cosmetics, laundry detergents, toys, accessories).[3-6] In this scenario, a current challenge is the synthesis and application of NPs[7-9] to implement effective control measures to reduce the incidence of healthcare-associated infections (HAIs). HAIs have become a global threat due to the emergence and dissemination of microbial pathogens that are resistant to most or even all antimicrobial agents available for their treatment (extensively drug-resistant or totally drug-resistant phenotypes).[10,11] HAIs are in fact a major cause of patient morbidity and mortality.[12] Most of the principal nosocomial pathogens can asymptomatically colonize the human host, with colonization representing either a risk factor for infection or a key step for their dissemination. Indeed,

Abbreviations: NP, nanoparticle; HAI, healthcare-associated infection; SCBD, supersonic cluster beam deposition; AFM, atomic force microscopy; XPS, X-ray photoemission spectroscopy; XRD, X-ray diffraction; CFU, colony forming units; ME, microbicidal effect.

The authors declare no competing financial interests.

The authors disclose any commercial associations, current and within the past five years, that might pose a potential, perceived or real conflict of interest to this work. This research was supported in part by Università Cattolica del Sacro Cuore through D2.2 grants.

Acknowledgment: We thank Mirco Chiodi for performing XRD measurements.

*Corresponding author. Interdisciplinary Laboratories for Advanced Material Physics (i-LAMP) & Dipartimento di Matematica e Fisica, Università Cattolica del Sacro Cuore di Brescia, Brescia, Italy.

E-mail address: luca.gavioli@unicatt.it (L. Gavioli).

http://dx.doi.org/10.1016/j.nano.2015.02.023

1549-9634/© 2015 The Authors. Published by Elsevier Inc. This is an open access article under the CC BY-NC-ND license (http://creativecommons.org/licenses/by-nc-nd/4.0/).

an estimated 20% to 40% of HAIs have been attributed to cross infection via the hands of healthcare personnel, who may become contaminated indirectly by touching contaminated environmental surfaces.[13] Besides the strict adhesion to hand-hygiene practices and classical environmental cleaning procedures, the development of antimicrobial surfaces/coatings characterized by a long-lasting microbicidal effect to be applied in high-touch hospital devices (e.g. buttons or handles), has been advocated as a promising approach.[11,13] Some of the challenging aspects concerning fabrication of antimicrobial films are the adhesion to metal surfaces, determined by the NP–surface interactions, the ability to maintain the microbicidal effect over time and the lack of non-wet synthesis methods.

Among the large number of NPs investigated so far for antimicrobial features, Ag NPs have been considered the most promising ones for potential medical applications.[5] Ag NPs exert an antibacterial activity through a multifactorial process which has not been clearly elucidated, and involving either damaging of bacterial cell wall and plasma membrane, or inhibition of DNA replication and protein synthesis.[14] NP morphological characteristics (i.e. shape, size) have been proven to affect antibacterial efficacy of Ag NPs, with a recent work demonstrating that this could be related to a differential release of Ag^+ ions (i.e. the actual effectors of bactericidal activity).[8]

To date, the synthesis of Ag NPs is largely based on wet chemical reduction starting from a molecular precursor containing Ag in an oxidized state.[15] Such methods allow a great control over size and shape of the Ag NPs, but pose several problems such as the use of colloidal stabilizers, the presence of impurities, the solvents and synthesis process costs to reduce or avoid the problem of NP aggregation in solution.[16,17] Moreover, the mere synthesis of the Ag NPs does not imply a good adhesion of the obtained NPs to the substrate of need. The layer-by-layer approach[16] has been proposed to obtain surfaces on which thin films/layers of Ag NPs are deposited or formed as a molecular self-assembled monolayer, while pre-functionalization of glass has been used to stabilize the Ag NPs on the surface, further complicating the synthesis and deposition process.[17]

A so far unexplored alternative route to Ag NP wet synthesis is provided by the supersonic cluster beam deposition (SCBD).[18,19] The source is based on the pulsed plasma ablation of the material to be deposited and the subsequent formation of an NP beam. The method, which is intrinsically environmentally-friendly since it does not employ solvents, has also been shown to produce NPs with mixed chemical composition,[19] hence allowing the possibility of combining different elements to engineer the material properties. To our knowledge, this method has not been applied yet to synthesize Ag NP films with antimicrobial properties. In the present work, we obtain for the first time Ag NP films via SCBD directly on the surface of microscope slides, with an easy control over film thickness and density. The films are extremely uniform and composed of pure Ag NPs with an average diameter of 8 nm. Data show that the NP oxidation state is Ag_2O and the films present a high bactericidal activity against a wide range of clinically relevant pathogens (including extensively drug-resistant Gram positive and Gram negative strains).

Methods

NP film synthesis and characterization

Nanostructured Ag films were deposited at room temperature (RT) in medium vacuum (base pressure 1×10^{-6} mbar) conditions by SCBD based on the pulsed microplasma cluster source (see Figure S1 of Supplementary Materials)[18-20] directly on the surface of soda lime glass (SLG) microscope slides (electron microscopy sciences). The nominal film thickness and deposition rate were measured during deposition by a quartz microbalance, while film physical properties where obtained *ex situ* by atomic force microscopy (AFM) (Solver-pro NT-MDT), X-Ray photoemission spectroscopy (XPS), Auger Spectroscopy, X-Ray diffraction (XRD) and optical absorption spectroscopy. Once deposited in the vacuum chamber, the films are extracted to air and either transferred to the measurement apparatus or left exposed to the environment. More details on the experimental characterization procedures can be found in Supplementary Materials.

Antimicrobial activity of Ag NP films

Antimicrobial activity of Ag NP films was investigated against a panel of clinically relevant microorganisms, representative of both Gram negative and Gram positive bacteria, and yeasts. They included six reference strains (i.e. *Escherichia coli* ATCC 25922, *Pseudomonas aeruginosa* PAO-1, *Acinetobacter baumannii* ATCC 17978, *Staphylococcus aureus* ATCC 6538, *Enterococcus faecalis* ATCC 29212, *Candida albicans* ATCC 10231) and ten clinical strains exhibiting antimicrobial resistance phenotypes of concern and/or being recognized as members of high-risk epidemic clones (see Table 1 and references therein[21-27] for clinical strains characteristics).

Antimicrobial activity testing was performed using the procedure proposed by Pallavicini et al,[28] with some minor modifications. Briefly, 1 ml of an overnight culture was washed twice with Phosphate Buffered Saline (PBS) pH 7.4, and 10 μl of microorganism suspension (i.e. range 5.4-7.3 log Colony Forming Units [CFU], see Table T1 of Supplementary Materials for details) was deposited both in a glass slide containing the Ag NP film (challenge slide) and in an unmodified glass slide (control slide), and a glass coverslip was applied (20 × 20 mm). After 24 h of incubation at 25 °C in damp environment, microorganisms were suspended in 10 ml of PBS, appropriately diluted, and 240 μl of each dilution was plated for viable cell count (i.e. enumeration of CFU). The log reduction rate was expressed as Microbicidal Effect (ME), following the formula: $ME = \log N_C - \log N_E$ (where N_C and N_E represented the number of CFU obtained with control slides and challenge slides, respectively). The detection limit of viable cell count was 4.2×10^1 CFU. All microorganisms were tested in three independent experiments and results were averaged. In order to calculate standard deviations (SDs), when no viable cells were counted, the result was arbitrary assumed as 4.2×10^1 CFU, representing the detection limit value. All microorganisms were grown aerobically at 37 °C in a shaker incubator (200 rpm) in Mueller–Hinton II broth (BD, Becton, Dickinson and Company, Sparks, MD, USA), except for *Enterococcus* spp. and *C.*

Table 1
Microbicidal Effect (ME) of Ag NP films against clinically relevant microorganisms after 24 h of exposure.

Strain	ME (log CFU ± SD)	Strain features
Gram negatives		
Escherichia coli ATCC 25922	≥5.6 ± 0.1	Reference strain
Escherichia coli CVB-1	≥5.7 ± 0.1	XDR clinical isolate producing the carbapenemase NDM-1[21]
Klebsiella pneumoniae FIPP-1	5.4 ± 0.4	XDR epidemic ST258 clone producing the carbapenemase KPC-3[22]
Klebsiella pneumoniae KKBO-4	5.2 ± 0.7	XDR epidemic ST258 clone producing the carbapenemase KPC-3 and resistant also to colistin[23]
Pseudomonas aeruginosa PAO-1	≥5.7 ± 0.3	Reference strain
Pseudomonas aeruginosa VR-143/97	2.6 ± 0.8	XDR epidemic clone producing the carbapenemase VIM-1[24]
Acinetobacter baumannii ATCC 17978	4.2 ± 0.1	Reference strain
Acinetobacter baumannii RUH 134	3.9 ± 0.7	Reference strain for the global clone 2[25]
Acinetobacter baumannii AB06C13	4.2 ± 0.5	XDR clinical isolate belonging to global clone 2 and producing the carbapenemases OXA-23 and OXA-58[26]
Gram positives		
Staphylococcus aureus ATCC 6538	3.7 ± 0.8	Reference strain
Staphylococcus aureus MRSA-IT16	4.4 ± 0.4	Methicillin-resistant clinical isolate from biofilm-associated infection[27]
Staphylococcus aureus MRSA-IT1	2.0 ± 0.4	Methicillin-resistant clinical isolate from biofilm-associated infection and exhibiting hVISA and daptomycin resistance phenotype[27]
Enterococcus faecalis ATCC 29212	1.7 ± 0.6	Reference strain
Enterococcus faecium FI2013	0.9 ± 0.2	Glycopeptide-resistant clinical isolate from bloodstream infection
Yeasts		
Candida albicans ATCC 10231	0.7 ± 0.1	Reference strain
Candida albicans EMO1303	1.0 ± 0.1	Clinical isolate from bloodstream infection

CFU, colony forming unit; SD, standard deviation; XDR, extensively drug resistant isolates exhibiting a resistance phenotype including aminoglycosides, fluoroquinolones, and β-lactams (including also carbapenems); hVISA, heterogeneous vancomycin-intermediate *Staphylococcus aureus*.

albicans for which Brain-Heart-Infusion broth (BD) and Yeast Extract-Peptone-Dextrose broth (BD) were used, respectively. Viable cell count was performed in Sabouraud-Dextrose agar (Oxoid, Milan, Italy) for *C. albicans*, and in Luria-Bertani Agar (LBA) (Oxoid) for all other microorganisms.

Results

A representative atomic force microscopy (AFM) image of the as-deposited NP films synthesized in the present work is shown in Figure 1, *A*. The NPs exhibit no signs of fragmentation and present a very homogeneous distribution (rms roughness < 1 nm) with no coarsening over the entire covered area (about 15 cm^2). This is a common feature in SCBD films due to the NP soft landing, regardless of the type of compound deposited.[18,19] The average NP size obtained from the AFM data is around 20 nm (see inset of Figure 1, *A*). However, this has to be taken as an upper limit due to the convolution of the NP shape with the AFM tip (nominal radius 10 nm). X-ray diffraction data (see Figure S2 of Supplementary Materials) indicate that the NPs are partly crystalline and have an average crystallographic domain size of 3.2 ± 0.1 nm, which has to be taken as lower limit (see description of Figure S2 of Supplementary Materials). Since the film thickness measured by AFM is 7.8 ± 0.6 nm and the average height obtained from a statistical analysis of the AFM images is 3.8 (see Figure S3 of Supplementary Materials), it is reasonable to consider an average diameter of 7.8 ± 0.6 nm. Hence the film thickness chosen in the present work corresponds to a single layer of NPs i.e. 8 nm, with an NP density 70 ± 2 NPs on an area of 6.25×10^4 nm^2, i.e. $1.15 \pm 0.04 \times 10^{11}$ NPs/cm^2, as deduced from the AFM data. Since the film density depends on the deposition time, it can be easily tuned from a very low coverage (few percent of the surface area) up to a single layer and beyond.

The chemical state of the NP film has been investigated using XPS and Auger. The Ag Auger line shape is very sensitive to the Ag oxidation state.[29-31] A comparison of normalized MNN Auger spectra, obtained from the 8 nm Ag NP film deposited on the SLG substrate (curve b) and from a polycrystalline, metallic Ag reference (curve a), is shown in Figure 1, *B* together with their difference (curve (b − a)). Spectrum b) presents a broader line shape, reflected in the difference peak at 351 ± 0.5 eV, while the feature at 357 ± 0.5 eV is due to the appearance of a new structure: both consistent with the presence of Ag^+ ions.[31] The oxidation of the as-deposited NP film is confirmed by the XPS data shown in Figure 1, *C*, where the normalized O1s core levels obtained from the as-deposited Ag NPs (curve b) and from the clean SLG substrate (curve a) are shown, together with their difference (curve (b − a)). A least square fitting procedure (see Figure S4 of Supplementary Materials) shows that the clean SLG spectrum presents the SiO_2 peak at 531.6 eV ± 0.5 eV, and a shoulder at 530.1 ± 0.5 eV, due to contributions of Na_2O and CaO.[32] The data taken on the Ag NP film show an intensity increase of the shoulder at 530.1 ± 0.5 eV, due to the appearance of a peak at 530.2 ± 0.5 eV, typical of Ag_2O.[32] Although a possible core-shell structure of NPs with an oxidized shell surrounding a metallic core cannot be ruled out, the data indicate that in the synthesized film the NPs are in a Ag_2O oxidation state. This is a required condition for NPs to release Ag^+ ions, process recently proposed as the more relevant mechanism with respect to the role of the NP size giving rise to the bactericidal activity of the NPs.[8]

Since the typical time elapsed between film synthesis and an antimicrobial activity test was within 15 days, we have analyzed

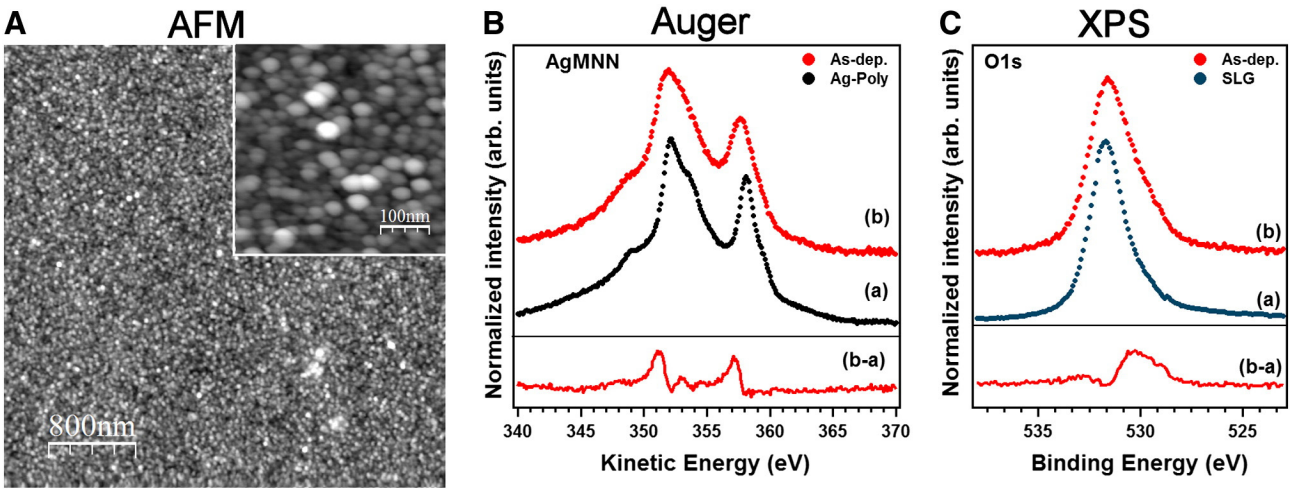

Figure 1. **(A)** AFM image of the as-deposited Ag NP film, showing the uniformity at microscopic scale. Inset: high resolution image where the NP size can be observed. **(B)** Auger spectra of the as-deposited NP film (curve **(b)**, red dots) and metallic polycrystalline Ag reference (curve **(a)**, black dots), with the difference spectrum shown in the bottom to highlight the oxidation state of the NP film. **(C)** XPS spectra of the O1s core level for the as-deposited NP film (curve **(b)**, red dots) and for the clean microscope slide (curve **(a)**, blue dots), with the difference spectrum shown in the bottom to highlight the oxidation state of the NP film.

the NP films as a function of time. After 15 days we observe only a slight increase of the average NP size, as quantified in Figure 2, *C*, showing that the density and the Ag NP size are basically unchanged. In Figure 2, *E* we report the Auger data taken at increasing time intervals that are compared to the as deposited curve through the difference spectra in the bottom panel. We can note only a slight intensity increase of the Ag_2O component, suggesting that just after the synthesis some of the NPs (less than 2% according to the intensity variation) are not completely oxidized. Such increase is also reflected in a sharpening of the plasmon resonance observed in the optical absorption spectra shown in Figure 2, *D*. The broad feature around 480 nm is consistent with the fact that the NPs are in contact with each other, hence giving rise to different resonances related to different NP sizes. The fact that film morphology is not modified as a function of time, in particular the NP diameter, markedly differentiates this type of NP films from previously observed backward/forward reactions observed in colloidal suspensions.[33] The overall emerging picture is that the synthesized films have a very good stability with respect to coarsening and oxidation state.

Ag NP films were found to exert a broad-spectrum bactericidal activity, which was demonstrated both with reference strains and with a collection of clinical strains that exhibited extensively drug-resistant phenotypes and/or belonged to high-risk hyperepidemic clones (see Table 1 and references therein for strains characteristics).[21-27] In particular, after 24 h of exposure to Ag NP films, a reduction of viable bacterial loads by more than 3 log (compared to controls) was observed with 10 of the 14 bacterial strains tested, including representatives of both Gram positive and Gram negative pathogenic species (Tables 1 and T1 of Supplementary Materials). Members of the family Enterobacteriaceae (i.e. *E. coli* and *K. pneumoniae*), which are normal constituents of the intestinal microbiota and among the most common causes of HAIs[12] showed a consistently very high susceptibility to Ag NP films (i.e. ME > 5 log CFU) (Tables 1 and T1 of Supplementary Materials). Interestingly, Ag NP films could almost completely sterilize a high inoculum (i.e. $\sim 1 \times 10^7$ CFU) of extensively drug-resistant clinical strains producing two of the most worrisome resistance mechanisms recently emerged in enterobacteria and capable of pandemic dissemination, such as the carbapenemases NDM-type and KPC-type.[21-23] An overall strong bactericidal activity (i.e. ME range > 5.7-2.6 log CFU) was also demonstrated with reference and clinical strains of *P. aeruginosa* and *A. baumannii*, including representative of extensively drug-resistant high-risk clones (Tables 1 and T1 of Supplementary Materials). Those microorganisms are major opportunistic pathogens in the hospital setting, with a high propensity to evolve extensively drug-resistant and even totally drug-resistant phenotypes and to survive for long periods in the hospital environment (accounting for the occurrence of nosocomial epidemics through, for example, contaminated taps, sinks or even antiseptic solutions).[13] The finding of a lower susceptibility to Ag NP films of the clinical *P. aeruginosa* VR-143/97 strain compared to the other four Gram negative non-fermenters tested, could suggest that this extensively drug-resistant strain might have evolved some resistance mechanism also to Ag NPs (e.g. by chromosomal mutations or horizontal gene transfer). Concerning Gram positive bacteria, high susceptibility to Ag NP films was demonstrated with two of the three *S. aureus* tested (ME > 3 log CFU), including a reference strain and a methicillin-resistant strain isolated from a biofilm-related infection (i.e. naive valve endocarditis) (Tables 1 and T1 of Supplementary Materials). Biofilm-forming bacteria are a major challenge in nosocomial settings, due to their tolerance to antiseptic and antimicrobial agents, and have been estimated to be responsible for more than 60% of HAIs, mainly associated to the presence of artificial medical devices (e.g. mechanical ventilators, central venous catheters, prosthetic devices etc.).[34] The *S. aureus* strain exhibiting a reduced susceptibility to Ag NPs (i.e. ME = 2 log CFU), was also isolated from a biofilm-associated infection (i.e. post-surgical wound infection) and was characterized by an uncommon resistance phenotype extended also to daptomycin (one of the most recent antibiotic class entered the clinical practice). It could be hypothesized that the overall reduction of anionic surface charge

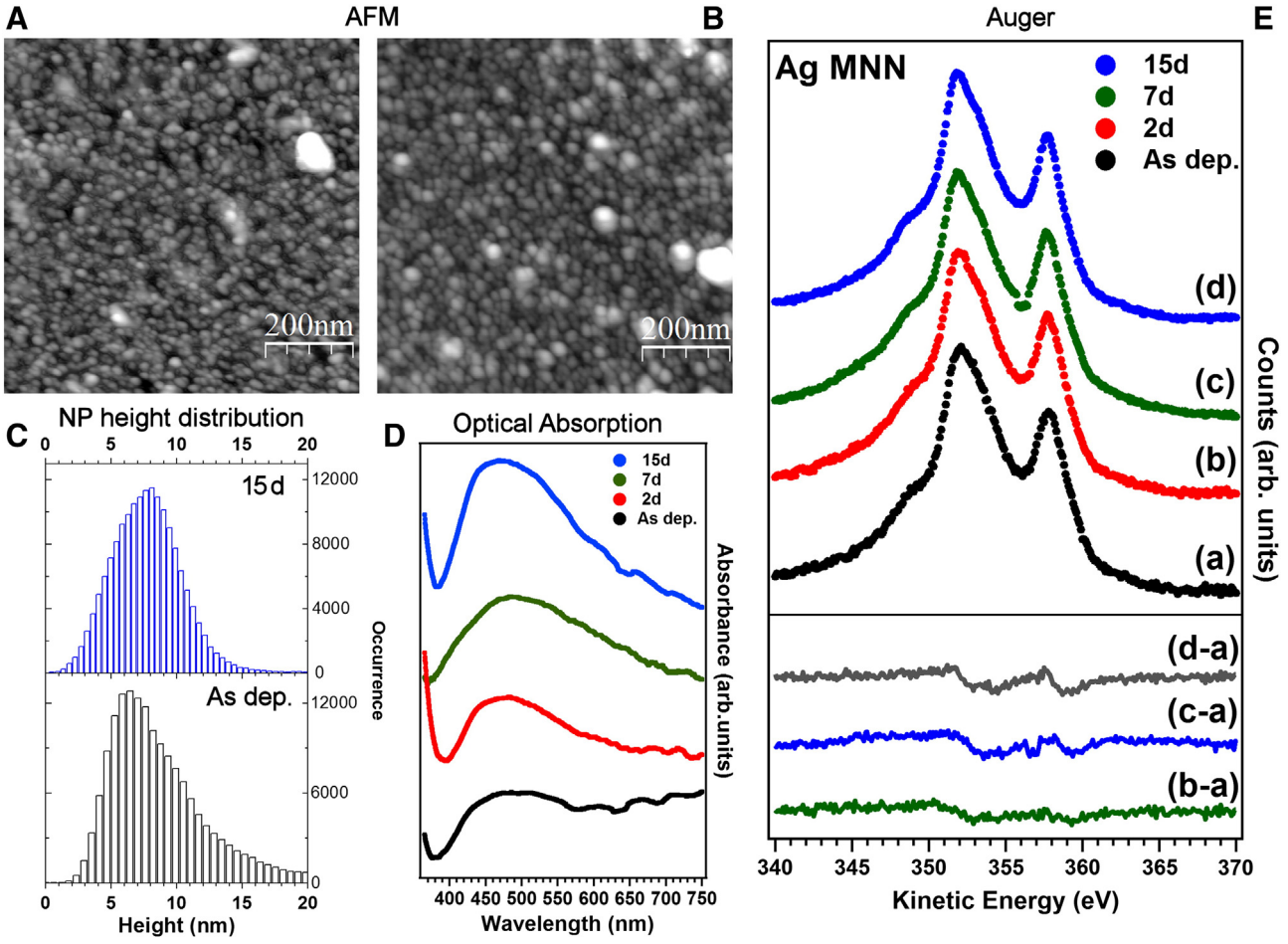

Figure 2. **(A)** AFM image of the as-deposited film; **(B)** AFM image of the same film after 15 days of exposure to air. **(C)** NP height distribution obtained from **(a)** (bottom) and **(b)** (top), respectively. **(D)** Optical absorption spectra as a function of elapsed time after deposition. **(E)** Auger spectra taken at different time intervals, with the difference curves in the bottom panel.

that has been associated to daptomycin resistance in *S. aureus*[35] might have contributed to the reduced susceptibility to Ag NPs, by impairing the interaction with the positively charged silver ions, a fact that would worth further investigation. Finally, *Enterococcus* spp. strains exhibited a relatively low susceptibility to Ag NP films (ME range 0.9-1.7 log CFU), as well as the two *C. albicans* strains (ME range 0.7-1 log CFU) (Tables 1 and T1 of Supplementary Materials). The poor activity of Ag NPs against the latter microorganisms is an intriguing phenomenon, and the reasons accounting for this will deserve further attention. The possibility to use the flexibility of the SCBD for generating NPs with mixed chemical composition will allow investigating antimicrobial features of diverse NP films, with the aim of implementing antimicrobial surfaces which could include also those important nosocomial pathogens.

Discussion

The Ag antimicrobial properties have been known for long time, although the synthesis of Ag NPs as antimicrobial material is relatively recent.[15] This has brought to include Ag NPs in a wide variety of applications[14] but also to propose their use as coatings. However, the transfer from the synthesized NPs from solutions onto the substrate has evidenced the NP coarsening effect and the weak bound formed between the NPs and the substrate.[16,17] Recently, for wet-synthesized Ag NPs transferred on glass, an amino-silanization treatment of the surface has been proposed[17] to increase the adhesion of the coating. The results presented here demonstrate a completely different route to synthesize Ag NPs as compared to the wet chemistry approach. The use of SCBD allows the immediate and direct deposition of the coating on virtually any substrate, with a perfect control over the coating thickness and density that are dependent only on deposition time. Moreover, the synthesis process is completely free of solvents and produces ultrapure Ag NPs, while it does not require any pretreatment or formation of a siloxane sol as mandatory prerequisite to stabilize the Ag NPs obtained by wet chemistry. The film deposited by SCBD on soda lime glass substrates presented here have a good stability also with respect to time (see Figure S5 of Supplementary Materials): it is worth noting that the exposure to air of the SCBD film does not alter its morphology apart from a very slight coarsening of the NPs, while the percent of NPs that are oxidized is even improved. Moreover, the observed film stability with respect to time is comparable to that of the Ag NP films deposited on amino-silanized surfaces as

reported by Taglietti et al.[17] Concerning the film adhesion to the SLG surface, we have compared the behavior of the SCBD films on plane glass and on amino-silanized glass.[17] The adhesion of the film has been tested by employing a home-made scratching test and subsequently measuring the optical transmission of the film, as described in the Supplementary Materials. The main result is that the SCBD film is indeed able to persist after the scratch test, although the presence of the silanization layer improves the wear resistance by about 15 %, as indicated by the intensity variation of the optical transmission (See Figure S5 of Supplementary Materials). These data confirm that on glass the silanization pretreatment is able to improve the adhesion, but is however not necessary in our case to obtain a fairly stable film.

Considering the dimension of the covered area reported in this experiment it is possible to envisage a scalability of this technique to larger surfaces and to surfaces of metals without modification of the proposed synthesis process. It is also worth noting that the SCBD approach has a large development potential in terms of control of the Ag NP surface adhesion through the formation of NPs alloyed with other biocompatible metals. Such potential has been already suggested by synthesis of a 95%–5% Ti–Cr alloy where Cr is located in substitutional sites of the Ti lattice.[19]

As far as the antimicrobial activity is concerned, the effectiveness of the film prepared here is relevant and with a broad spectrum. Indeed, after 24 h of exposure a bactericidal activity (i.e. decrease in viable cell count $\geq$99.9%) was observed with most tested bacterial strains, including representatives of the major clinically relevant Gram negative and Gram positive pathogens. The notable lower antimicrobial activity of the Ag NP films obtained in this study against *Enterococcus* spp. and *C. albicans*, and the observation of reduced susceptibility in some extensively drug-resistant *P. aeruginosa* and *S. aureus* clinical strains, represent a limitation that will be addressed in future studies through the implementation of NP films with mixed chemical composition.

In perspective, the ability to modify the NP chemical composition provided by the SCBD method will open large possibilities for tailoring the active material in order to: optimize the precious metal amount; expand the spectrum of antimicrobial activity; reduce the risk for resistance development; tailor the adhesion to surfaces to obtain a long lasting, low cost antimicrobial film, in particular for metal surfaces.

In conclusion we have demonstrated the realization of a uniform Ag NP film with extremely controlled thickness and NP size directly on a substrate surface through a simple and scalable technique, SCBD. The Ag_2O oxidation state of the NPs and the film morphology are stable in time. We have demonstrated that such films present a relevant and broad-spectrum bactericidal activity that could be related to the oxidation state of the Ag NPs. This work opens the way for exploring the potential of supersonic beams as alternative method for antibacterial coating synthesis.

Appendix A. Supplementary data

Supplementary data to this article can be found online at http://dx.doi.org/10.1016/j.nano.2015.02.023.

References

1. Boisselier E, Astruc D. Gold nanoparticles in nanomedicine: preparations, imaging, diagnostics, therapies and toxicity. *Chem Soc Rev* 2009;**38**:1759-82.
2. Liu C, Burghaus U, Besenbacher F, Wang ZL. Preparation and characterization of nanomaterials for sustainable energy production. *ACS Nano* 2010;**4**:5517-26.
3. Li Q, Mahendra S, Lyon DY, Brunet L, Liga MV, Li D, et al. Antimicrobial nanomaterials for water disinfection and microbial control: potential applications and implications. *Water Res* 2008;**42**:4591-602.
4. Badireddy AR, Hotze EM, Chellam S, Alvarez PJJ, Wiesner MR. Inactivation of bacteriophages via photosensitization of fullerol nanoparticles. *Environ Sci Technol* 2007;**41**:6627-32.
5. Seil JT, Webster TJ. Antimicrobial applications of nanotechnology: methods and literature. *Int J Nanomedicine* 2012;**7**:2767-81.
6. Tolaymat TM, El Badawy AM, Genaidy A, Scheckel KG, Luxton TP, Suidan M. An evidence-based environmental perspective of manufactured silver nanoparticle in syntheses and applications: a systematic review and critical appraisal of peer-reviewed scientific papers. *Sci Total Environ* 2010;**408**:999-1006.
7. Seo YI, Hong KH, Kim DG, Kim YD. $Ag/Al(OH)_3$ mesoporous nanocomposite film as antibacterial agent. *Colloids Surf B Biointerfaces* 2010;**81**:369-73.
8. Xiu ZM, Zhang QB, Puppala HL, Colvin VL, Alvarez PJJ. Negligible particle-specific antibacterial activity of silver nanoparticles. *Nano Lett* 2012;**12**:4271-5.
9. Guzman M, Dille J, Godet S. Synthesis and antibacterial activity of silver nanoparticles against gram-positive and gram-negative bacteria. *Nanomedicine* 2012;**8**:37-45.
10. Boucher HW, Talbot GH, Bradley JS, Edwards JE, Gilbert D, Rice LB, et al. Bad bugs, no drugs: no ESKAPE! An update from the Infectious Diseases Society of America. *Clin Infect Dis* 2009;**48**:1-12.
11. Weber DJ, Rutala WA. Self-disinfecting surfaces: review of current methodologies and future prospects. *Am J Infect Control* 2013;**41**:S31-5.
12. European Centre for Disease Prevention and Control. Point prevalence survey of healthcare-associated infections and antimicrobial use in European acute care hospitals 2011-2012. , http://www.ecdc.europa.eu/en/publications/Publications/healthcare-associated-infections-antimicrobial-use-PPS.pdf2013.
13. Weber DJ, Anderson D, Rutala WA. The role of the surface environment in healthcare-associated infections. *Curr Opin Infect Dis* 2013;**26**:338-44.
14. Chaloupka K, Malam Y, Seifalian AM. Nanosilver as a new generation of nanoproduct in biomedical applications. *Trends Biotechnol* 2010;**28**:580-8.
15. Rycenga M, Cobley CM, Zeng J, Li W, Moran CH, Zhang Q, et al. Controlling the synthesis and assembly of silver nanostructures for plasmonic applications. *Chem Rev* 2011;**111**:3669-712.
16. Yliniemi K, Vahvaselka M, Van Ingelgem Y, Baert K, Wilson BP, Terryn H, et al. The formation and characterisation of ultra-thin films containing Ag nanoparticles. *J Mater Chem* 2008;**18**:199-206.
17. Taglietti A, Arciola CR, D'Agostino A, Dacarro G, Montanaro L, Campoccia D, et al. Antibiofilm activity of a monolayer of silver nanoparticles anchored to an amino-silanized glass surface. *Biomaterials* 2014;**35**:1779-88.
18. Barborini E, Kholmanov IN, Piseri P, Ducati C, Bottani CE, Milani P. Engineering the nanocrystalline structure of TiO2 films by aerodynamically filtered cluster deposition. *Appl Phys Lett* 2002;**81**:3052-4.
19. Chiodi M, Parks Cheney C, Vilmercati P, Cavaliere E, Mannella N, Weitering HH, et al. Enhanced dopant solubility and visible-light absorption in Cr-N co-doped TiO_2 nanoclusters. *J Phys Chem C* 2012;**116**:311-8.
20. Chiodi M, Cavaliere E, Kholmanov IN, de Simone M, Sakho O, Cepek C, et al. Nanostructured TiO_x film on Si substrate: room temperature formation of $TiSi_x$ nanoclusters. *J Nanopart Res* 2010;**12**:2645-53.
21. D'Andrea MM, Venturelli C, Giani T, Arena F, Conte V, Bresciani P, et al. Persistent carriage and infection by multidrug-resistant *Escherichia coli*

ST405 producing NDM-1 carbapenemase: report on the first Italian cases. *J Clin Microbiol* 2011;**49**:2755-8.
22. Giani T, D'Andrea MM, Pecile P, Borgianni L, Nicoletti P, Tonelli F, et al. Emergence in Italy of *Klebsiella pneumoniae* sequence type 258 producing KPC-3 carbapenemase. *J Clin Microbiol* 2009;**47**:3793-4.
23. Cannatelli A, D'Andrea MM, Giani T, Di Pilato V, Arena F, Ambretti S, et al. *In vivo* emergence of colistin resistance in *Klebsiella pneumoniae* producing KPC-type carbapenemases mediated by insertional inactivation of the PhoQ/PhoP *mgrB* regulator. *Antimicrob Agents Chemother* 2013;**57**:5521-6.
24. Riccio ML, Pallecchi L, Docquier JD, Cresti S, Catania MR, Pagani L, et al. Clonal relatedness and conserved integron structures in epidemiologically unrelated *Pseudomonas aeruginosa* strains producing the VIM-1 metallo-beta-lactamase from different Italian hospitals. *Antimicrob Agents Chemother* 2005;**49**:104-10.
25. Diancourt L, Passet V, Nemec A, Dijkshoorn L, Brisse S. The population structure of *Acinetobacter baumannii*: expanding multiresistant clones from an ancestral susceptible genetic pool. *PLoS One* 2010;**5**:e10034.
26. Principe L, Piazza A, Giani T, Bracco S, Caltagirone MS, Arena F, et al. Epidemic diffusion of OXA-23-producing *Acinetobacter baumannii* isolates in Italy: results of the first cross-sectional countrywide survey. *J Clin Microbiol* 2014;**52**:3004-10.
27. Landini L, Riccobono E, Giani T, Arena F, Rossolini GM, Pallecchi L. Bactericidal activity of ceftaroline against mature *Staphylococcus aureus* biofilms. *Int J Antimicrob Agents* 2015, http://dx.doi.org/10.1016/j.ijantimicag.2015.01.001.
28. Pallavicini P, Taglietti A, Dacarro G, Diaz-Fernandez YA, Galli M, Grisoli P, et al. Self-assembled monolayers of silver nanoparticles firmly grafted on glass surfaces: low Ag^+ release for an efficient antibacterial activity. *J Colloid Interface Sci* 2010;**350**:110-6.
29. Waterhouse GIN, Bowmaker GA, Metson JB. Oxidation of a polycrystalline silver foil by reaction with ozone. *Appl Surf Sci* 2001;**183**:191-204.
30. Wagner CD. Auger lines in x-ray photoelectron spectrometry. *Anal Chem* 1972;**44**:967-73.
31. Giallongo G, Pilot R, Durante C, Rizzi GA, Signorini R, Bozio R, et al. Silver nanoparticle arrays on a DVD-derived template: an easy & cheap SERS Substrate. *Plasmonics* 2011;**6**:725-33.
32. Miura Y, Kusano H, Nanba T, Matsumoto S. X-ray photoelectron spectroscopy on sodium borosilicate glasses. *J Non-Cryst Solids* 2001;**290**:1-14.
33. Douglas Gallardo OA, Moiraghi R, Macchione MA, Godoy JA, Perez MA, Coronado EA, et al. Silver oxide particles/silver nanoparticles interconversion: susceptibility of forward/backward reactions to the chemical environment at room temperature. *RSC Adv* 2012;**2**:2923-9.
34. Costerton JW, Stewart PS, Greenberg EP. Bacterial biofilms: a common cause of persistent infections. *Science* 1999;**284**:1318-22.
35. Humphries RM, Pollett S, Sakoulas G. A current perspective on daptomycin for the clinical microbiologist. *Clin Microbiol Rev* 2013;**26**:759-80.

Supplementary Materials

Highly bactericidal Ag nanoparticle films obtained by cluster beam deposition

Emanuele Cavaliere, Sebastiano De Cesari, Giulia Landini, Eleonora Riccobono, Lucia Pallecchi, Gian Maria Rossolini and Luca Gavioli*

Experimental methods

Supersonic Cluster Beam Deposition

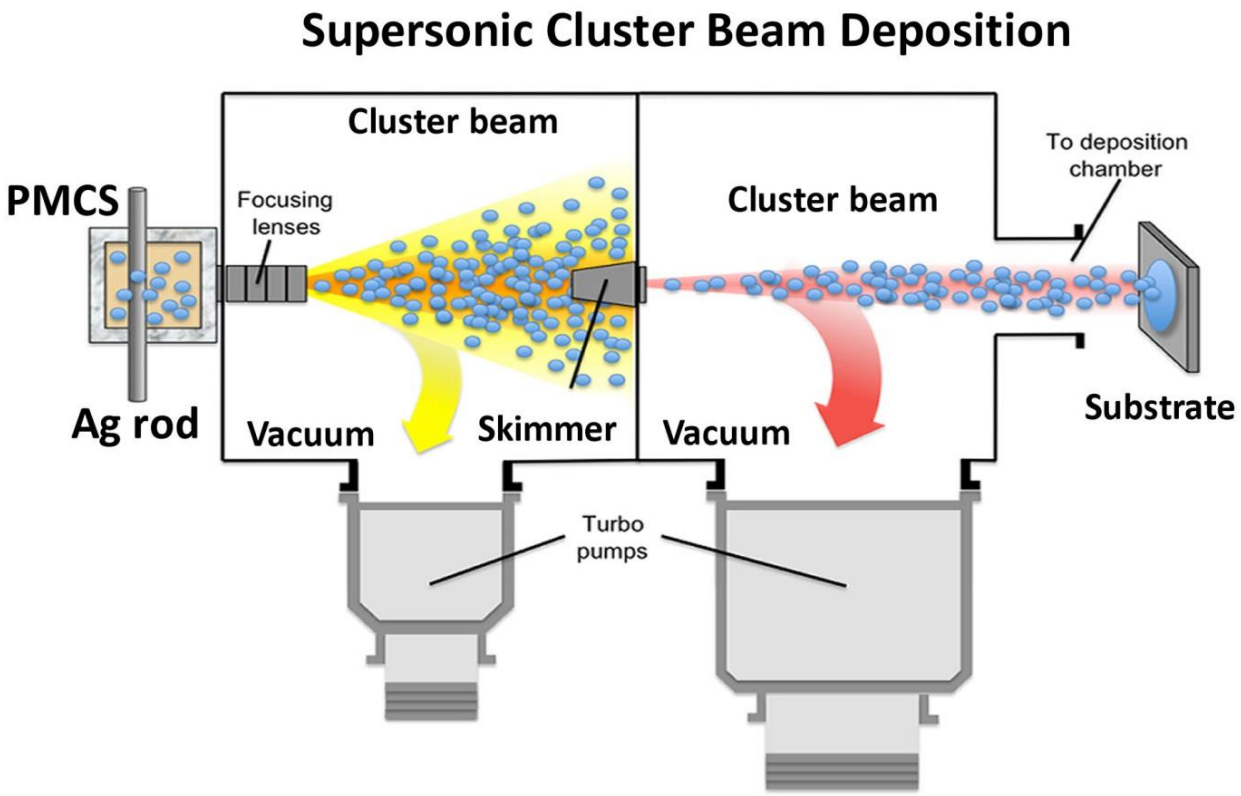

Figure S1. Scheme of the SCBD apparatus. The PMCS is the location where the clusters are generated. The first chamber is reached through a nozzle and a set of aerodynamic lenses. The skimmer selects the central part of the beam, going through the second vacuum chamber and reaching the substrate.

The basic principle of the SCBD (a scheme of the experimental setup is shown in Figure S1) is as follows: He is injected at P = 50 bar into the ablation chamber for few hundreds of microseconds directed against the Ag (purity 99.99%) target rod. Then a pulsed high voltage discharge is applied between the target rod (cathode) and the body of the source (anode), obtaining a plasma that ablates the Ag rod. Subsequently clusters condense into the ablation chamber and exit through a nozzle and a set of aerodynamic lenses to reach supersonic speed in the expansion chamber, where a skimmer of 2 mm diameter selects the central part of the beam that is directed on the substrate surface. The source have been used before to grow highly porous nanoparticle films of different materials (Ti, C, Pd) with a high surface to volume ratio.

Once deposited in the vacuum chamber, the films are extracted to air and transferred either to the measurement apparatus or left exposed to the environment. The films described in this work are obtained in vacuum conditions and the initially deposited film remains metallic, if kept in vacuum.

Film Characterization

The film morphology and the actual film thickness were obtained ex-situ by atomic force microscopy (AFM) (Solver-pro NT-MDT). The data were acquired under nitrogen flow in tapping mode employing an ETALON tip with nominal tip radius below 10 nm and oscillating frequency of 96 KHz.

The XPS data were acquired in a UHV multiscan lab (Omicron Nanotechnology) using a standard Mg -Kα X-ray source (hν = 1253.6 eV). Ex-situ XRD characterization was performed using a Bruker D8 advanced Diffractometer in Bragg-Brentano geometry. The analysis was performed using Ni-filtered Cu K_α radiation at 40 kV and 40 mA. The

crystallographic domain size was estimated using the so-called Scherrer formula after fitting the experimental profiles of the Ag(111) diffraction peak with a pseudo-Voigt function.

Optical absorption measurements were performed with a homemade apparatus consisting of a high intensity UV Xenon lamp, collimated on the sample with a UV-VIS optical fiber, and an Ocean Optics USB2000 sensor.

XRD data

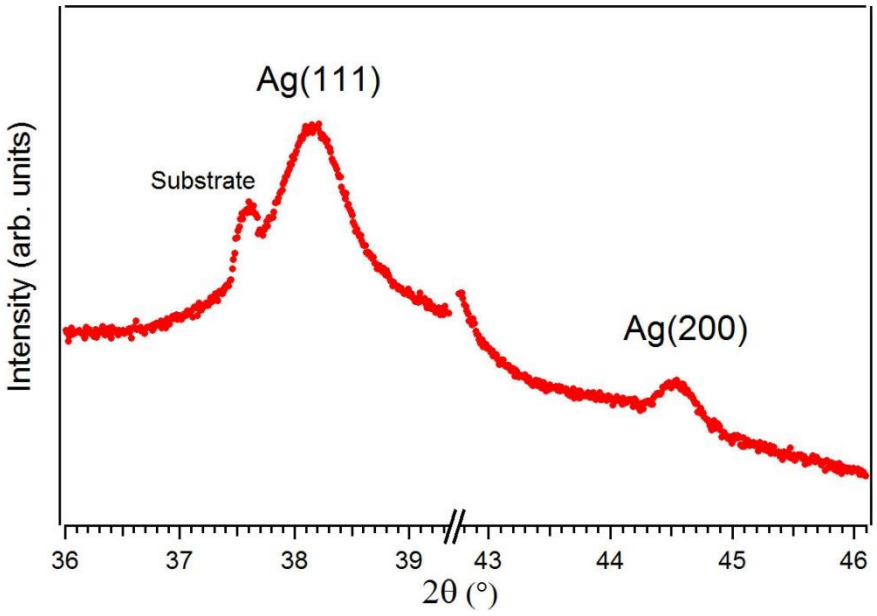

Figure S2. X-ray diffraction data. 2θ scan of Ag NPs film synthesized in the same conditions.

Figure S2 displays the diffraction peaks at 2θ= 38.1° and 44.5°, corresponding to (111) and (200) planes of fcc silver crystal. The average crystallographic domain size, estimated from the FWHM analysis of the (111) peak, gives a value of 3.2 ± 0.1 nm. This value can be explained by considering a core shell structure of the NP, composed of a crystalline core surrounded by an amorphous matrix layer, which cannot be probed by XRD. Therefore this has to be taken as a lower limit for the total NP size.

AFM analysis

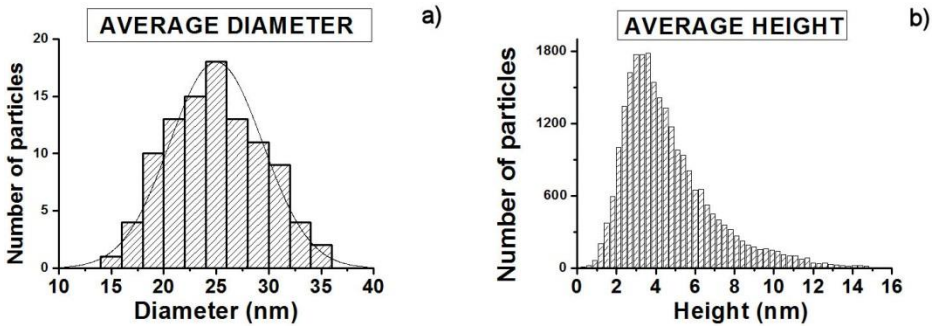

Figure S3. Analysis of the AFM images. a) Statistical distribution of the average NP diameter as obtained from AFM images. b) Statistical distribution of the average NP height as obtained from AFM images

Figure S3 displays the NP average height and diameter obtained from the AFM images. The estimation of Ag NP average diameter has been obtained by manually measuring the full width at half maximum (FWHM) of the z line profile for a hundred of nanoclusters. The obtained value is of about 25 nm, in disagreement with the XRD size estimation. However, it should be noted that AFM images have been acquired using a tip with a nominal curvature radius of 10 nm, resulting in an overestimation of the Ag NP diameter due to tip-sample convolution effects. On the other hand, the average height profile of the single layer film provides value of 3.8 nm. Since NP are very close to each other, the AFM tip will not be able to penetrate in the separation between the NP; moreover, the total film thickness is about 8 nm. Hence we can safely assume that the observed distribution corresponds to the NP radius.

XPS fitting

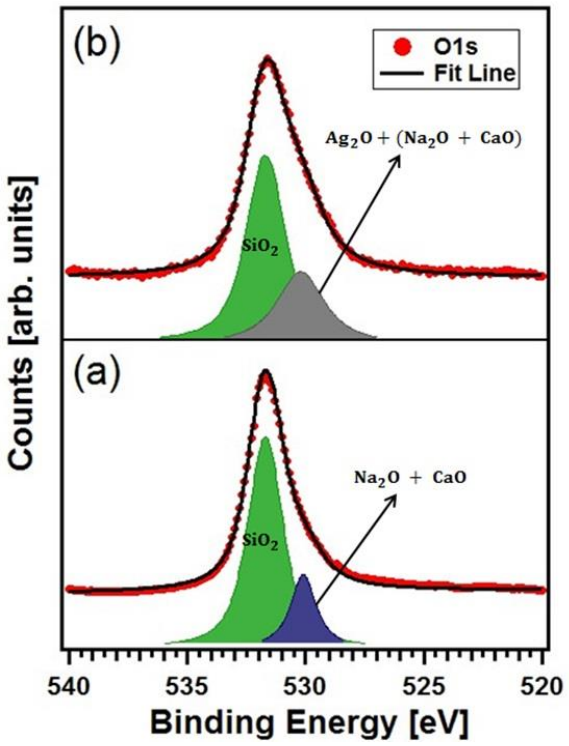

Figure S4. Least square fitting of the oxygen 1s core level. O1s core level for a) the clean soda lime glass (SLG) and b) for the SLG with 8 nm Ag NP film deposited on it, with least square fitting peaks below. Shaded green, SiO_2 core level; shaded blue, core level due to the oxidized Na and Ca components in the SLG; shaded blue, core level due to the contribution of Ag_2O.

The least square fitting results obtained for the O1s core level, showing the increase and widening of the components ah lower binding energy. Such behavior is due to the presence of oxidized Ag NP. Moreover, the values of Auger parameters, observed from the relative energy positions between Ag 3d and Ag MNN peaks, shows that Ag NP are actually oxidized and their oxidation state is compatible with an Ag2O stoichiometry. However, due to the very shallow escape depth of photoelectrons from NPs, a possible core-shell structure of NPs with an oxidized shell surrounding a metallic core cannot be ruled out.

Adhesion test

Adhesion of the Ag NP film deposited by SCBD was investigated both on bare and (3-aminopropyl) triethoxysilane (>99%, APTES) SLG surfaces. The effect of the mechanical scratching was assessed using optical grade sandpaper (mesh size 1 μm) with a controlled vertical force of 8N over an area of 0.5 cm^2 and dragging horizontally the sandpaper for 2mm on the deposited Ag film. Optical absorption was used to measure the variation of transmission from the treated region of the samples.

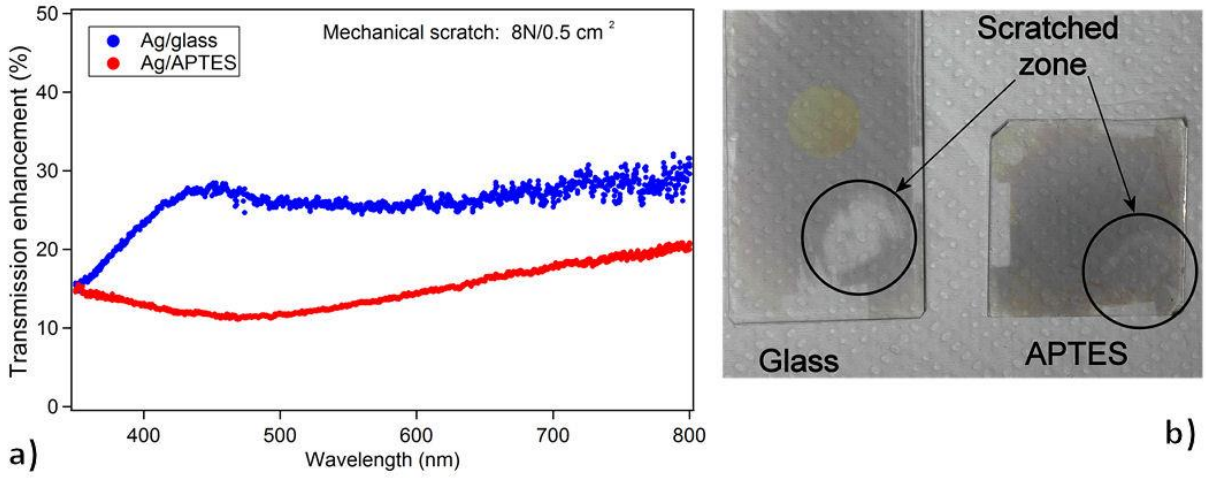

Figure S5. a) Enhancement of optical transmission through the Ag NP film deposited either on bare SLG (blue curve) or APTES covered SLG surface (red curve) after mechanical scratch exerted on the Ag NP film. b) Picture of the bare (left) and APTES precovered (right) SLG deposited with the Ag NP film after scratch performed circled areas.

Figure S5 a) shows how the optical transmission through the system is enhanced by 20 % after scratching for Ag NP film deposited on bare SLG, while such enhancement is only around 10% for Ag NP film deposited on APTES precovered SLG. Even by simple eyesight (Figure S5 b) it is then clear that the Ag film is more effectively bound on the APTES substrate than on bare SLG, though some removal of the Ag NP film occurs in both cases (the transmission is enhanced with respect to pristine, not scratched films in both cases).

Table T1 Microbicidal Effect (ME) of Ag NP films against clinically relevant microorganisms after 24 hours of exposure

Strain	**$logN_C$ [CFU ± SD]**	**$logN_E$ [CFU ± SD]**	**ME [$logN_C$ - $logN_E$]**
Gram negatives			
Escherichia coli ATCC 25922	7.2 ± 0.1	1.6 ± 0.0▼	≥ 5.6 ± 0.1
Escherichia coli CVB-1	7.3 ± 0.1	1.6 ± 0.0▼	≥ 5.7 ± 0.1
Klebsiella pneumoniae FIPP-1	7.3 ± 0.1	1.9 ± 0.4►	5.4 ± 0.4
Klebsiella pneumoniae KKBO-4	7.3 ± 0.0	2.0 ± 0.7►	5.2 ± 0.7
Pseudomonas aeruginosa PAO-1	7.3 ± 0.3	1.6 ± 0.0▼	≥ 5.7 ± 0.3
Pseudomonas aeruginosa VR-143/97	5.4 ± 0.4	2.8 ± 1.0▲	2.6 ± 0.8
Acinetobacter baumannii ATCC 17978	6.9 ± 0.1	2.7 ± 0.1	4.2 ± 0.1
Acinetobacter baumannii RUH 134	6.0 ± 0.1	2.1 ± 0.7▲	3.9 ± 0.7
Acinetobacter baumannii AB06C13	6.1 ± 0.1	1.9 ± 0.5►	4.2 ± 0.5
Gram positives			
Staphylococcus aureus ATCC 6538	6.5 ± 0.1	2.8 ± 0.9	3.7 ± 0.8
Staphylococcus aureus MRSA-IT16	6.0 ± 0.4	1.6 ± 0.0►	4.4 ± 0.4
Staphylococcus aureus MRSA-IT1	6.8 ± 0.0	4.8 ± 0.4	2.0 ± 0.4
Enterococcus faecalis ATCC 29212	6.1 ± 0.0	4.4 ± 0.6	1.7 ± 0.6
Enterococcus faecium FI2013	6.1 ± 0.0	5.1 ± 0.2	0.9 ± 0.2
Yeasts			
Candida albicans ATCC 10231	6.2 ± 0.0	5.5 ± 0.2	0.7 ± 0.1
Candida albicans EMO1303	6.0 ± 0.1	5.1 ± 0.1	1.0 ± 0.1

CFU, colony forming unit; SD, standard deviation; N_C, CFU obtained with the control slide (average of three independent experiments); N_E, CFU obtained with the Ag NP films (average of three independent experiments). The detection limit of viable cells count was 4.2×10^1 CFU. When after Ag NPs challenge no viable cells were counted in one (▲), two (►) or three (▼) independent experiments, the arbitrary value of 4.2×10^1 CFU (representing the detection limit) was used for calculating N_E and ME.

Direct synthesis of antimicrobial coatings based on tailored bi-elemental nanoparticles

Giulio Benetti,[1,2] Emanuele Cavaliere,[1] Adalberto Canteri,[1] Giulia Landini,[3] Gian Maria Rossolini,[3,4,5] Lucia Pallecchi,[3] Mirco Chiodi,[6] Margriet J. Van Bael,[2] Naomi Winckelmans,[7] Sara Bals,[7] Luca Gavioli[1,*]

1 Interdisciplinary Laboratories for Advanced Materials Physics (i-LAMP) and Dipartimento di Matematica e Fisica, Università Cattolica del Sacro Cuore, Via Musei 41, 25121 Brescia.

2 Laboratory of Solid State Physics and Magnetism, Department of Physics and Astronomy, KU Leuven, Celestijnenlaan 200D, B-3001, Leuven, Belgium

3 Department of Medical Biotechnologies, University of Siena, Viale Bracci 1, 53100 Siena, Italy

4 Department of Experimental and Clinical Medicine, University of Florence, Via San Damiano, 50134 Florence,Italy

5 Don Carlo Gnocchi Foundation, Via di Scandicci 269, 50143 Florence, Italy

6 Empa, Swiss Federal Laboratories for Materials Science and Technology, Laboratory for Joining Technologies and Corrosion, Überlandstrasse 129, 8600 Dübendorf, Switzerland

7 EMAT University of Antwerp, Groenenborgerlaan 171, B-2020 Antwerp, Belgium

KEYWORDS antimicrobial coatings, bi-elemental nanoparticles, gas phase synthesis, tunable concentrations, microbicidal activity

Abstract word count: 149

Complete manuscript word count: 4097

Number of references: 37

Number of figures: 4

Number of tables: 2

Number of Supplementary online-only files: 1

ABSTRACT Ultrathin coatings based on bi-elemental nanoparticles (NPs) are very promising to limit the surface-mediated spread of bacterial pathogens, particularly in the hospital setting. However, tailoring the coating synthesis, composition, adhesion to substrate, and antimicrobial spectrum is an open challenge. Herein, we obtain a radically new bi-elemental Ag/Ti nanostructured coating on different substrates by one-step gas-phase deposition. The coating is characterized by a cluster-in-cluster phase with metallic ultra-active Ag NPs embedded in an amorphous TiO_2 matrix and present a promising antimicrobial activity including also multidrug resistant strains. We demonstrate how to tune the Ag NPs size and the coating total relative composition, opening the possibility of tailoring the physical/chemical properties and the antimicrobial spectrum of multi-elemental NPs coatings. This work is expected to significantly spread the NPs coatings range of applications, as an effective tool in the prevention of healthcare-associated infections and in other fields like sensors or nano/micro joining.

BACKGROUND The synthesis of tunable and durable microbicidal coatings based on nanoparticles (NPs) is becoming of critical importance,[1,2] since indirect transmission of pathogens through contaminated surfaces is a recognized major global health threat, especially in the hospital setting.[3–6] The development of a functional NPs coating implies 1) the ability to precisely deposit such NPs on a wide variety of substrates; 2) the capability to tune its composition and properties through a proper combination of its constituting elements in a single NP, a critical step in achieving an effective microbicidal effect.

So far, the synthesis of NPs composed of two elements (bi-NPs) has stimulated research efforts,[7–12] due to their remarkably enhanced catalytic, microbicidal, optical, electronic and mechanical properties that goes beyond the mere sum of the effects of the constituent materials. For instance, Ag/Fe NPs allows their removal from a solution after the Ag microbicidal effect has been exploited,[7] while the combination of Au and Pt into bimetallic NPs shows a remarkable microbicidal effect that the single metal NPs (either Au or Pt) do not present.[8] Small quantities of Pd inside Pd-W NPs metal are sufficient to enhance the cluster stability and catalytic properties due to the formation of ultra-active Pd hot-spots.[9]

However, very little is known about the formation and properties of bi-NPs–based coatings.[13] Time-consuming multi-step post-synthesis processes, colloidal stabilizers, cross-linking growth or substrate functionalization are required when NPs are synthesized in a wet environment,[14] therefore increasing the degree of complexity of the system. In this respect, the synthesis and growth of controlled antimicrobial coating with bi-NPs in a single step is an open challenge. A feasible alternative to directly synthesize and deposit controlled nano-structured multi-elemental coatings is based on gas-phase synthesis techniques,[15–17] and in particular Supersonic Cluster Beam Deposition (SCBD).[16,17] Here, the synthesized NPs form a beam that allows the direct deposition of the coating on the substrate. At present, antimicrobial coatings composed of bi-NPs have never been obtained by this approach, and the dynamics of the multi-elemental condensation taking place inside the cluster source has not been comprehensively understood yet.

In this work, we present a new family of antimicrobial films composed of bi-elemental Ag-Ti NPs synthetized in a single production step. Notably, with our deposition method the size and the relative concentration of the constituents can be finely tuned. The NPs mixing phase is similar to the cluster-in-cluster aggregation,[14] with Ag crystals partly embedded in an amorphous TiO_2 matrix. The new type of nano-structured Ag-Ti coating shows good adhesion to the substrate and exhibits an exceptional bactericidal effect against major Gram-negative nosocomial pathogens. Remarkably, the new composite coating shows a bactericidal activity similar to a pure Ag NPs coating,[18] but with an 85% lower Ag mass content. Moreover, here we sketch the mechanism leading to the formation of this peculiar phase-separated structure, explaining the resulting microstructure (crystalline/amorphous) and the origin of the Ag NPs size tunability, shedding light on the influence of the carrier gas cooling rate in determining the NPs structure. Thus, this work opens the possibility to produce radically new materials for a wide variety of applications using a potentially unlimited gamma of elements to functionalize the coating properties (e.g. in health care environments broadening the antimicrobial spectrum by introducing other microbicidal metals, or tailor the coating adhesion by varying the elements relative concentration in the NPs).

METHODS The coatings have been deposited using a NPs beam obtained by SCBD (see Supplementary Note 1): a pulse of He is injected into the ablation chamber directed against the target rod. A synchronized high voltage discharge is applied between the target rod (cathode) and the body of the source (anode), obtaining a plasma that ablates the rod. The condensed NPs are extracted through a nozzle and are deposited directly on the substrate surface. The NPs coatings of three different materials, **AgTi8020** (nominal weight contents 80% Ag and 20% Ti), **AgTi5050** (nominal weight contents 50% Ag and 50% Ti) and **PureAg** (99.99% Ag), were deposited using the same operating conditions independently from the substrate, changing the deposition time to control the film thickness.

To perform a full physical and chemical characterization of the deposited bi-NPs we exploited atomic force microscopy (AFM), high resolution - high angle annular dark field - scanning transmission electron microscopy (HR-HAADF-STEM), Energy-dispersive X-ray spectroscopy (EDX), X-ray Photoemission Spectroscopy (XPS), Auger electron spectroscopy (AES) and grazing incidence X-ray diffraction (GIXD) whereas to estimate the adhesion of the coating to the substrate we performed a scratch test. Finally the antimicrobial properties of the NPs coatings (i.e. reduction of bacterial viability) were investigated against a panel of clinically relevant Gram-negative and Gram-positive nosocomial pathogens, for which contaminated surfaces represent a major vehicle for transmission.

The flexibility of SCBD allows to easily deposit scattered bi-NPs on a polished Si(100) single crystal, such bi-NPs can then be measured by atomic force microscopy (AFM), giving a precise estimation of their height distribution (Figure S1, Supplementary Information). AFM (Solver-pro NTMDT) was operated in tapping mode, using an Etalon HA-NC tip with a nominal radius of 10nm. Scattered bi-NPs have been also deposited on TEM carbon grid (quantifoil) to characterize their structure and their lateral dimension. HAADF-STEM imaging and EDX spectroscopy was performed with a probe corrected FEI TITAN microscope and a FEI Tecnai Osiris microscope respectively, both operated at 200 kV. GIXD was performed using a Bruker D8 Discovery diffractometer equipped with a Cu Kα Xray source (wavelength 0.15418 nm) on amorphous soda-lime glass substrate to eliminate the substrate contribution. XPS data were collected in an Omicron MultiScanLAB UHV apparatus (base pressure better than $2*10^{-10}$ mbar) equipped with a SPECS Phoibos 100 hemispherical electron energy analyzer, normal to the sample surface and operated at fixed analyzer transmission in small-area mode with pass energy of 30eV. A polycrystalline Ag sample (labelled AgPoly in the Figure 2 of the main text) was cleaned by several cycles of sputtering with 2.5 keV Ar ions and annealing up to 450 °C in vacuum, as reference for metallic Ag.

The antibacterial activity of AgTi5050 NPs was measured on commercially available chrome-plated supports, covered with a monolayer of NPs. Tested strains included both reference (Escherichia coli ATCC 25922, Pseudomonas aeruginosa PAO-1, Enterococcus faecalis ATCC 29212) and clinical isolates exhibiting multidrug resistance phenotypes (P. aeruginosa Z33, Acinetobacter baumannii AB06C13, Staphylococcus aureus MRSA-IT1) (**Table 1**). Briefly, each support was located in a well of a 6-well polystyrene tissue culture plate (IWAKI microplate, Bibby Scientific Limited, Staffordshire, UK) and contaminated with a standardized bacterial suspension (i.e. about 1×10^7 Colony Forming Units - CFU in Phosphate Buffered Saline - PBS pH 7.3, distributed in ten drops of 5 µl each) (Figure S4 of Supplementary Information).

Contaminated supports were then incubated at 25°C in dark and damp environment for 3 hours (extended to 24 hours for Gram-positive strains, and including additional measurements at 15, 45 and 90 minutes for the A. baumannii strain). After the incubation time, bacterial cells were removed from the supports by adding 2 ml of PBS containing 1% Tween-20 (a surfactant favoring the detachment of bacteria from the supports), incubating 30 minute and gently pipetting. Appropriate dilutions (i.e. 80 µl for each 10-fold dilution) were successively plated onto Tryptic Soy Agar (TSA) plates (Oxoid, Milan, Italy) for viable cell count. All data were obtained in at least three independent experiments.

Strain	Main features
Gram negatives	
Escherichia coli ATCC 25922	Reference strain
Pseudomonas aeruginosa PAO-1	Reference strain
Pseudomonas aeruginosa Z33	Multidrug resistant clinical isolate from cystic fibrosis
Acinetobacter baumannii AB06C13	Multidrug resistant clinical isolate belonging to global clone 2[19]
Gram positives	
Staphylococcus aureus MRSA-IT1	Methicillin-resistant clinical isolate from biofilm-associated infection[20]
Enterococcus faecalis ATCC 29212	Reference strain

Table 1. Origin and main features of the six tested bacterial strains

RESULTS Using AFM we found that the median height of the AgTi5050 bi-NPs is 4.3 nm, 30% higher than the 3.3 nm of AgTi8020 (Figure S1 b and d, Supplementary Information). Furthermore the longer tail of the AgTi5050 distribution, extending up to 12 nm, indicates an appreciable increase in the vertical dimension of the bi-NPs with increasing Ti concentration.

The HAADF-STEM images of Figure 1 show areas with different contrast inside each NP, characterized by an intense spot partly surrounded by a lighter gray zone (Figure 1a,d). The elemental maps taken on the same NPs (Figure 1b,c) clearly indicate that such contrast difference is due to Ag (red) and Ti (green) phase-separated bi-NPs. Hence, our results suggest that SCBD synthesizes aggregates of (crystalline) Ag NPs partly embedded in an amorphous Ti matrix. An increase of the Ti concentration leads to an increase in the average bi-NP size, related to the formation of aggregates having multiple Ag NPs embedded in the Ti matrix. To obtain statistical information on the size and crystallinity of the deposited bi-NPs as a function of the Ti concentration, a large number of HR-STEM images were acquired for bi-NPS and for pure Ag NPs (Figure 1e,f,g). Our data confirm the Ag and Ti phase separation at the nanoscale. Moreover, the Ag NPs observed within the Ti matrix in the AgTi8020 and AgTi5050 cases (Figure 1f,g,) are mostly polycrystalline, as they were in the pure Ag phase (Figure 1e). Interestingly, the Ti matrix partly surrounding the Ag NP (indicated with green arrows) appears to be completely amorphous instead. The crystallinity of the Ag NPs (either pure or in the Ti matrix), is confirmed by the 2D-fast Fourier transform (FFT) of the purple-squared areas shown

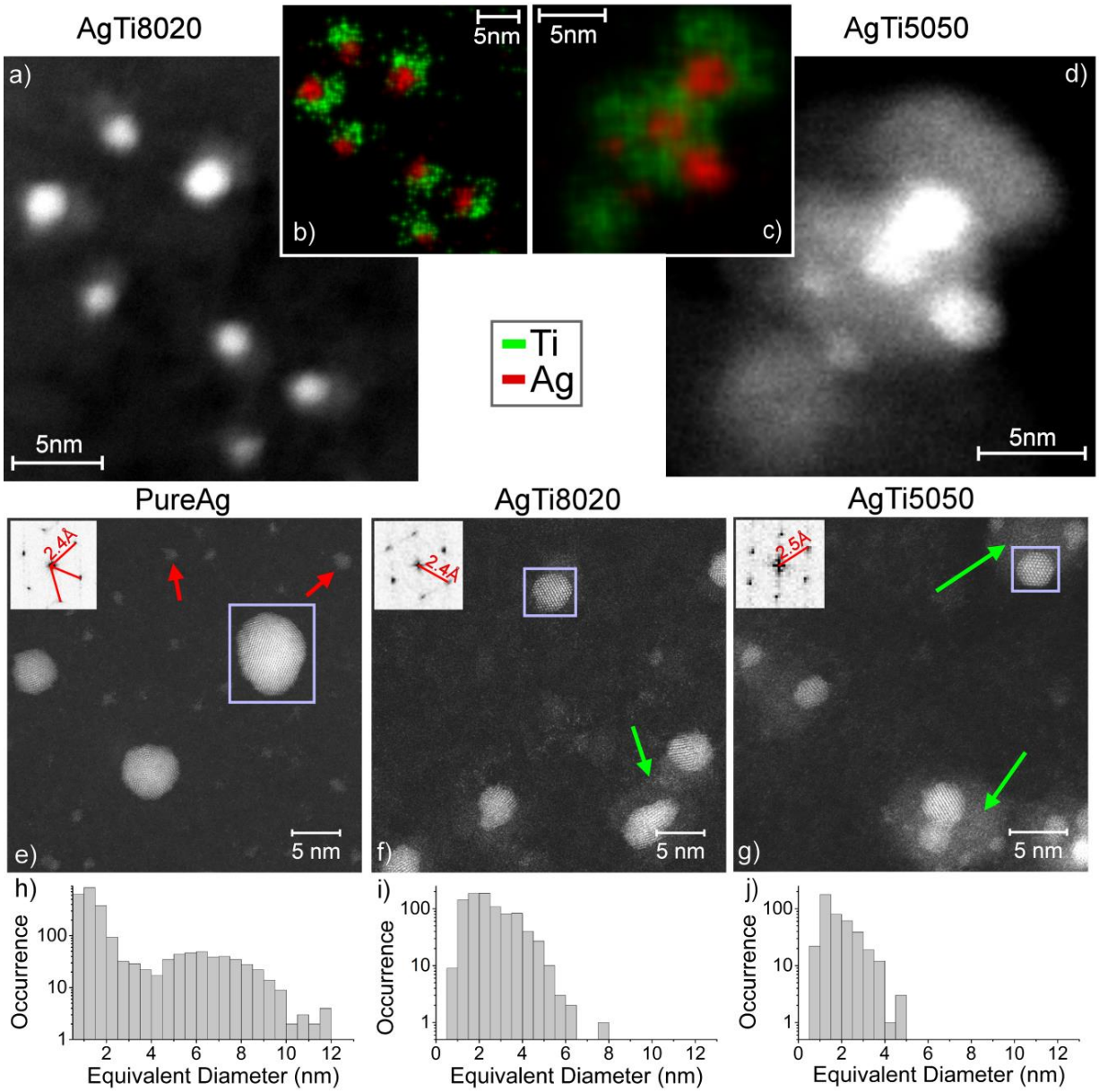

in the inserts of Figure 1e,f,g. The FFT maxima provide a vector length of 0.24 ± 0.01 nm, compatible with the one of bulk, unstrained Ag{111} spacing (0.236 nm).

Figure 1. a, b, c, d) HAADF images of AgTi8020 and AgTi5050 scattered NPs with the relative elemental map. Short acquisition times are used to limit beam-induced damage (i.e. NPs moving or deforming). e, f, g) High resolution HAADF-STEM images of the NPs and FFT analysis of Ag crystalline structure of the zone in the purple rectangle. Red arrows are indicating small Ag NP, green arrows are pointing to the Ti part of the NPs. h, i, j) frequency histograms of the Ag crystallites dimension.

This result is also confirmed by GIXD data (Figure S2 and Note 3, Supplementary Information) obtained on a 100nm-thick AgTi5050 NP film deposited on glass. Here, the diffraction pattern clearly shows the presence of Ag nano-crystallites, with the Ag{111} peak located at 0.236±0.002 nm. On the other hand, Ti-related peaks are not found. Hence, the deposited bi-NPs are composed by a mixture of Ag nanocrystals intermixed with amorphous Ti. Notably, by increasing the Ti/Ag ratio, the dimension of the Ag nano-crystallites decreases:

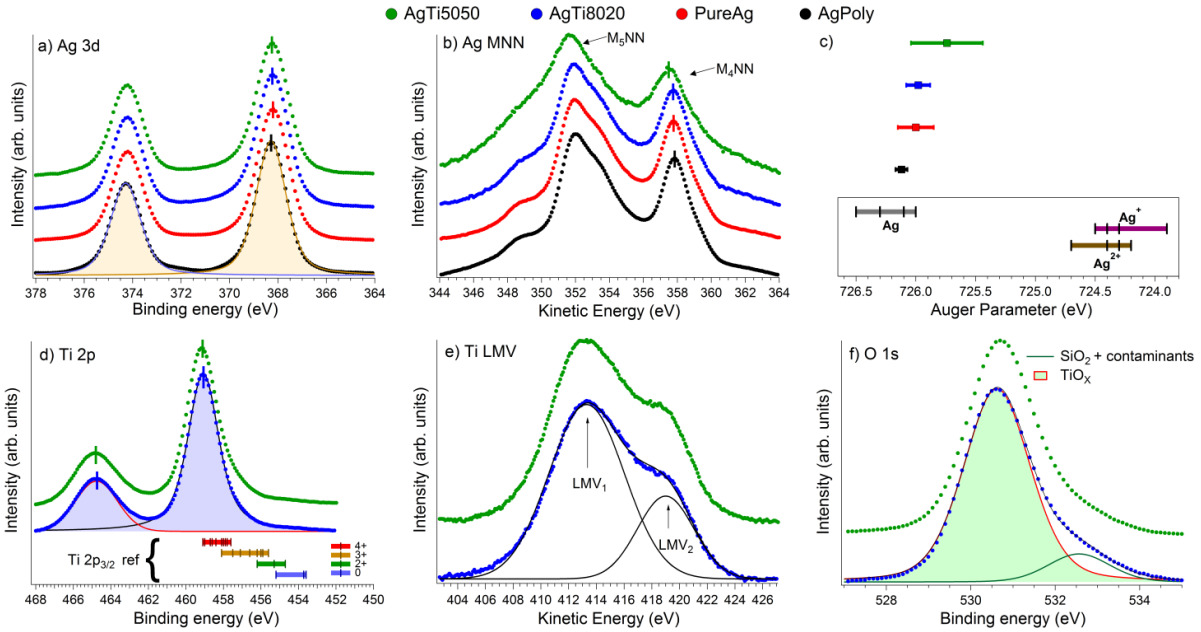

from 2.5 nm in the case of AgTi8020 to 1.8 nm in the case of AgTi5050. Providing an easy but effective way to tailor the Ag NPs size by varying the composition of the sputtered rod.

Figure 2. Spectroscopic analysis of the NPs coatings for different systems: Pure Ag (red dots), AgTi5050 (green dots), AgTi8020 (blue dots), and polycrystalline Ag (black dots). a) Ag 3d core level; b) Ag MNN Auger emission line; c) experimental Ag Auger parameter compared to literature.[21–26]; d) Ti 2p core levels compared with the literature for different electronic configurations.[27] ; e) Ti LMV Auger emission line: the relative area of Ti LMV peaks indicate the presence of Ti^{4+}; f) O 1s core level and relative fits. Highlighted area of panels a, d, f are used to obtain the relative stoichiometric and mass concentration of the three elements. Fits and quantifications were made for each peak but only the first one is displayed.

These results are also consistent with the AFM data presented before, since STEM images resolve the lateral dimension of Ag nano-crystallites embedded in the Ag-Ti bi-NPs, whereas AFM gives an estimation of the total height of the aggregate (including the Ag crystallites and the Ti matrix).

Figure 2 shows Auger electron spectroscopy (AES) and X-ray photoemission spectroscopy (XPS) data taken on three 20 nm-thick NP films deposited on Si(100) substrates having different NP compositions. As a reference, the same set of measurements is also reported for a pure (99,99%) polycrystalline Ag sample. A least square fitting procedure using Voigt functions for the core levels and Gaussian functions for the Auger has been used to determine the intensity and energy position of the structures. Table 2 reports the most important fitting parameters obtained from the XPS analysis.

Notably, in the three coatings the Ag NPs do not undergo any oxidation, as indicated by both Ag 3d core level and MNN Auger spectra reported in Fig. 2a and b. In fact, a comparison between the data obtained on the NPs and on the pure Ag reference does not show any appreciable variation in the intensity or in the energy (both Binding, BE or Kinetic, KE) position for any of the spectral lines. To this end, particularly significant is the Ag M_4NN Auger

transition, which is known to be strongly affected by the adsorption of oxygen impurities.[21] The small lineshape differences found in the AgTi5050 Auger spectrum (shoulder at 348.5eV and in the intensity and width of the peak) stem from a Ti Auger line present in the 350 - 357 eV KE region,[22] that becomes relevant with the increasing Ti content. The analysis of the corresponding Auger parameter (defined as the Ag $3d_{5/2}$ BE + Ag $M_4N_{4,5}N_{4,5}$ KE) further confirms the purely metallic character of the Ag NPs, see Figure 2c.[23–26]

Figure 2d and 2e show the Ti 2p core level and LMV Auger emission data for AgTi5050 (green dots) and AgTi8020 (blue dots) NPs coatings, respectively. The Ti 2p core level peaked at 453.6 eV BE and the spin-orbit split energy of 5.7eV indicate a Ti^{4+} configuration state.[27] Moreover, the Auger LMV spectra show that both the energy and the relative area of the two different peaks are compatible with oxidized Ti.[28]

The coating stoichiometry was estimated comparing the integral intensity of the collected core level peaks (see also the oxygen O1s in figure 2f showing the presence of a major contribution from oxygen bonded to Ti at 530.6 eV[29]) and the results are reported in Table S2 (Supplementary Information): Ag is metallic and Ti is doubly oxidized. Moreover, our data clearly indicate that the compositional changes in the pristine rod (i.e. pure Ag, AgTi8020, AgTi5050) correspond to an analogous variation in the produced bi-NPs stoichiometry. Therefore, SCBD also proves to be a powerful tool to actually tailor the NPs chemical composition simply adjusting the Ag/Ti relative concentration in the initial rod. Nonetheless, we indeed observe a slight differentiation between the Ag/Ti ratio in the rod compared to the one in the deposited bi-NPs.

		AgTi5050	AgTi8020	PureAg	AgPoly
Ag	**$3d_{3/2}$**	374.24	374.23	374.22	374.29
	$3d_{5/2}$	368.26	368.23	368.22	368.28
	3d SO	5.98	6	6	6.01
	MNN	357.5	357.75	357.78	357.84
	AP	725.7 (0.3)	725.98 (0.10)	726.00 (0.15)	726.12 (0.05)
Ti	**$2p_{1/2}$**	464.79	464.76	--	--
	$2p_{3/2}$	459.1	459.07	--	--
	2p SO	5.69	5.69	--	--
	LMV1	413.3	413.3	--	--
	LMV2	419	419	--	--
	V1/V2	0.38 (0.10)	0.36 (0.10)	--	--
O	**1s (TiO_2)**	530.73	530.62	--	--

Table 2. The table report the binding energies for the two peaks of Ag3d and Ti2p together with their difference (Spin Orbit energy, SO in the table). Kinetic energies of Ag M_4NN and Ti L_3MV are reported together with Ag Auger Parameter (AP) and its experimental error. All the four obtained AP are fully compatible with the literature. The adimensional ratio between the areas of Ti L_3MV_1 versus Ti LMV_2 (Ti V1/V2) has been reported since it can be used to identify the chemical state of Ti. Finally the binding energy of O1s related with TiO_2 is reported in the last row of the table.

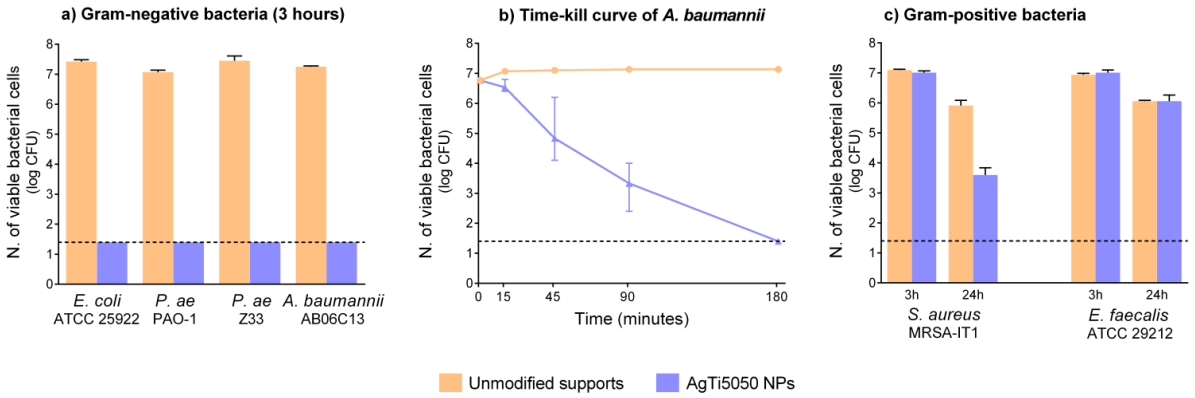

Figure 3. Antibacterial features of AgTi5050 NPs coatings: a) antibacterial activity against Gram-negative pathogens (3 hours of exposure); b) Time-kill curve of *A. baumannii* AB06C13 (multidrug resistant clinical isolate); c) antibacterial activity against Gram-positive pathogens (3 and 24 hours of exposure). CFU – Colony Forming Unit; P. ae, *Pseudomonas aeruginosa*. Dotted lines indicate the detection limit of viable cell count (1.4 log CFU).

Characterization of the antimicrobial properties of the bi-elemental coatings was performed on the AgTi5050 NPs coating (the one with lower Ag content) and compared to a similar coating based on ultrapure Ag NPs previously obtained by SCBD.[18] The AgTi5050 NPs coatings (the thickness is a single NP layer) were found to be extremely effective against all the Gram-negative strains tested, *i.e.* two reference strains of *E. coli* and *P. aeruginosa*, and two multidrug resistant clinical isolates of *P. aeruginosa* and *A. baumannii* (Table 1). In fact, a reduction by more than 5 log CFU was observed for all tested strains after 3 hours of incubation (Figure 3a).

Shorter exposure times were tested against the multidrug resistant *A. baumannii* clinical isolate, in order to evaluate the kinetics of bactericidal activity. Results showed a detectable decrease of viable cells already after 15 minutes of exposure and a bactericidal effect (i.e. usually defined as a 3 log reduction of viable cell count compared to initial bacterial inoculum) achieved after 90 minutes (Figure 3b).

An overall lower and slower bactericidal activity was instead observed against the two Gram-positive strains tested (*i.e.* a reference strain of *E. faecalis*, and a methicillin-resistant *S. aureus* clinical isolate exhibiting also non-susceptibility to glycopeptides and daptomycin (Table 1)). In particular, while a sizable reduction of viable cells was obtained with the *S. aureus* strain after a longer exposure time on AgTi5050 NPs coatings, the *E. faecalis* strain remained substantially unaffected (Figure 3c).

Besides their antimicrobial performances, the bi-elemental NPs coatings produced using our Gas-Phase deposition method also benefit from the presence of the Ti matrix described in the previous sections. In fact, Ti is one of the most common metals used to enhance thin films adhesion on various substrates due to its high oxygen affinity and its ability to act like bridging

site at a film/substrate interface. To verify this effect in our NP-assembled coating, we performed an empirical comparison between the pure Ag NPs and the AgTi5050 films adhesion on a glass substrate (see Note 4 and Figure S3 in the Supplementary Information). With respect to the pure Ag NPs, the introduction of Ti remarkably enhances the adhesion without affecting the measured antimicrobial activity, saving at the same time more than 85% of the expensive metal (Supplementary Note 5).

DISCUSSION The results of the physical and chemical characterization of both the scattered NPs and the coating, open to a number of considerations on the condensation process forming the NPs.

The SCBD synthesis of Ag and Ti NPs in the same operative conditions gives rise to crystalline Ag[18] and amorphous Ti NPs[16,17]; this suggests that the physical mechanisms underlying the creation and the solidification of the clusters are similar even in the simultaneous presence of two different elements. In particular, the cooling rate of the metal/gas mixture is critical in determining the final structure of the condensing NPs.[30]

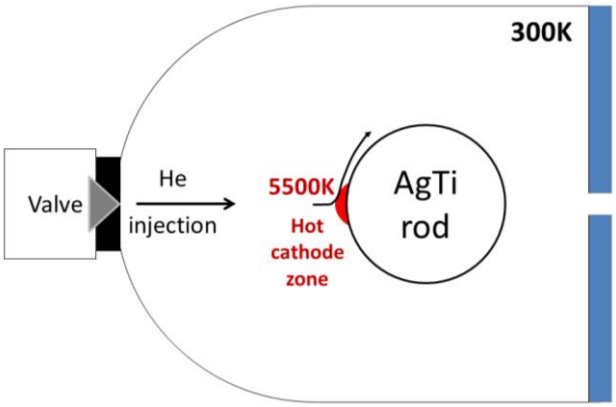

Figure 4. Internal geometry of the SCBD source.

Considering the present SCBD source geometry (see Figure 4 and Supplementary Note 1), we can roughly estimate the NPs cooling rate (dT_{NP}/dt), which is mainly due to the motion of the agglomerates from the hot cathode zone (i.e. the place where the atoms are ablated and thus the NPs start forming) to the cooler environment of the ablation chamber. The assumptions of this model are a perfect thermal coupling of the NPs with the carrier gas (due to the fact that in the proximity of the cathode zone the ambient pressure is some bars) and a constant temperature gradient near to the hot point, which involve a linear decrease of the temperature for a fixed velocity. Since we know that the NPs condensation and growth takes place only in the proximity of the cathode spot,[31] we have:

$$\frac{dT_{NP}}{dt} = \frac{\partial T}{\partial x}\frac{\partial x_{NP}}{\partial t} = \frac{\Delta T}{\Delta x} v_{NP}$$

where ΔT is the difference between the cathode spot temperature and the base temperature of the chamber, Δx is the distance the NPs have to travel to exit from the hot zone and v_{NP} is the

average velocity of the NPs. The Δ symbol indicates a macroscopic quantity. While the base temperature inside the ablation chamber can be taken, as a first approximation, equal to 300K[32] the cathode spot temperature can be estimated to be about 5500K, in agreement with the one experimentally obtained in a similar condition with a pure Ti rod[33] and with the qualitative comparison of the light emitted by the source during the discharge. On the other hand, previous fluidodynamic simulations on a geometry similar to the SCBD one show that the velocity of the carrier gas near to the cathode spot is about 10^3 m/s.[34] Therefore, considering Δx to be of the order of magnitude of the cathode spot diameter (1 mm) we obtain an estimation of the cooling rate to be about 5K/ns. This rate is in agreement with the observed values for crystalline NPs formation of Ag[30] while can also explain amorphous TiO_X cluster.

The peculiar cluster-in-cluster structure observed for the NPs synthesized in the present work clearly differs from the alloyed and the core-shell structures[13] and can be tentatively explained if we consider the different melting temperature of Ag and Ti. In fact, during the cooling process, Ti will form solid cluster when the temperature is below 1800 K, while at this temperature Ag will be still liquid. A solid Ti cluster will thus provide condensation and solidification nuclei for Ag, which become solid more or less at 700K for NPs of 5nm[35–37].

The smaller size of Ag crystallites for higher Ti rod contents is related to the fact that the major Ti presence provide a larger number of nucleation points for the Ag which is thus divided into small liquid drops before crystallization. Therefore our deposition route gives the possibility to tune the embedded Ag nano-crystals dimension and the total relative composition of the coating only by varying the starting rod element composition.

Concerning the antimicrobial features, the AgTi5050 NPs coatings were found to express a relevant bactericidal activity against representatives of the major Gram-negative pathogens for which indirect transmission through contaminated surfaces represents an important vehicle of dissemination, especially in the hospital setting (i.e. *P. aeruginosa* and *A. baumannii*). Indeed, a high inoculum of such strains (including two multidrug resistant clinical isolates) was almost completely sterilized within 3 hours of exposure to the AgTi5050 NPs coatings. Considering that environmental surfaces are thought to be contaminated with a much lower bacterial inoculum[7] than that used in the present study, our results suggest that AgTi5050 NP coatings could be highly effective antimicrobial tools for limiting the indirect transmission of Gram-negative pathogens, and could be evaluated as innovative tool for infection control purposes.

Despite an 85% lower Ag mass content, the microbicidal activity of AgTi5050 NPs coatings was found to be similar to that of pure Ag NPs coating synthetized by the same methodology.[18] Indeed, although a direct comparison was not possible due to different substrate types and revised microbiological procedures, a similar reduction in the number of viable bacterial cells was observed with strains tested in both studies, using comparable bacterial inocula for surface contamination. Overall, these results encourage further studies to exploit SCBD's ability to produce multi-elemental NPs and to include other antimicrobial metals in the NPs coating, with the principal aim of broadening the antimicrobial spectrum also toward Gram-positive bacteria.

In summary we produced a radically new nanostructured coating using a novel, one-step gas-phase deposition. The as deposited films are characterized by a cluster-in-cluster mixing phase with small metallic ultra-active microbicidal Ag hot-spots embedded in an amorphous matrix

of TiO_2, stable and strongly bonded to the substrate. Moreover, we demonstrated for the first time the possibility to exploit the flexibility of a SCBD source to produce multi-metallic NPs, opening the possibility of tailoring dimension, composition, antimicrobial spectrum and other physical/chemical properties of multi-elemental NPs only by varying the native rod's composition. The potential of this technique is also demonstrated by the wide variety of substrates employed (from conductive to insulating substrates, from single crystals to TEM grids, and commercial chromium-coated plastics) and the range of thicknesses obtained, from sub-monolayer (about 1%) up to few hundreds of nm. This work is expected to spread significantly the range of applications of NPs films, not only in the medical field but also in other technologically-relevant fields like sensors (where the selectivity to gas absorption is depending on the material employed), nano-microjoining (where NPs-based pastes are now used as a low-temperature alternatives to standard welding, brazing and soldering processes) or electrocatalysis.

ASSOCIATED CONTENT

(The Supplementary Information is available free of charge via the Internet at http://pubs.acs.org.
Details of coating preparation, data acquisition, scratch tests, bacterial tests and the data analysis.

AUTHOR INFORMATION

Corresponding Author

* e-mail: luca.gavioli@unicatt.it.

Author Contributions

The manuscript was written through contributions of all authors. All authors have given approval to the final version of the manuscript.

Funding Sources

The authors acknowledge financial support from the European Union through the 7th Framework Program (FP7) under a contract for an Integrated Infrastructure Initiative (Reference No. 312483 ESTEEM2).

Acknowledgments

We thank Urs Gfeller for the XRF measurements, Giulia Rossi and Riccardo Ferrando for discussions on the NPs condensation dynamics, and Giulio Viano for his valuable support in the microbiological analysis.

References

1. Lemire JA, Harrison JJ, Turner RJ; Antimicrobial activity of metals: mechanisms, molecular targets and applications; *Nat Rev Microbiol*; 2013;**11**(6):371-384;.**10.1038/nrmicro3028**
2. Faure E, Falentin-Daudré C, Lanero TS, Vreuls C, Zocchi G, Van De Weerdt C, et al.; Functional Nanogels as Platforms for Imparting Antibacterial, Antibiofilm, and Antiadhesion Activities to Stainless Steel; *Adv Funct Mater*; 2012;**22**(24):5271-5282;.**10.1002/adfm.201201106**
3. Humphreys H; Self-disinfecting and Microbiocide-Impregnated Surfaces and Fabrics: What Potential in Interrupting the Spread of Healthcare-Associated Infection?; *Clin Infect Dis*; November 2013:cit765;**10.1093/cid/cit765**
4. Weber DJ, Rutala WA; Self-disinfecting surfaces: Review of current methodologies and future prospects; *Am J Infect Control*; 2013;**41**(5):S31-S35;.**10.1016/j.ajic.2012.12.005**
5. Quinn MM, Henneberger PK, Braun B, Delclos GL, Fagan K, Huang V, et al.; Cleaning and disinfecting environmental surfaces in health care: Toward an integrated framework for infection and occupational illness prevention; *Am J Infect Control*; 2015;**43**(5):424-434;.**10.1016/j.ajic.2015.01.029**

6. Otter JA, Yezli S, French GL; The Role Played by Contaminated Surfaces in the Transmission of Nosocomial Pathogens; *Infect Control Hosp Epidemiol*; 2011;**32**(7):687-699;.**10.1086/660363**

7. Marková Z, Šišková KM, Filip J, Čuda J, Kolář M, Šafářová K, et al.; Air Stable Magnetic Bimetallic Fe–Ag Nanoparticles for Advanced Antimicrobial Treatment and Phosphorus Removal; *Environ Sci Technol*; 2013;**47**(10):5285-5293;.**10.1021/es304693g**

8. Zhao Y, Ye C, Liu W, Chen R, Jiang X; Tuning the Composition of AuPt Bimetallic Nanoparticles for Antibacterial Application; *Angew Chem Int Ed*; 2014;**53**(31):8127-8131;.**10.1002/anie.201401035**

9. Hu G, Nitze F, Gracia-Espino E, Ma J, Barzegar HR, Sharifi T, et al.; Small palladium islands embedded in palladium–tungsten bimetallic nanoparticles form catalytic hotspots for oxygen reduction; *Nat Commun*; 2014;**5**:5253;.**10.1038/ncomms6253**

10. Azam A, Ahmed AS, Oves M, Khan MS, Habib SS, Memic A; Antimicrobial activity of metal oxide nanoparticles against Gram-positive and Gram-negative bacteria: a comparative study; Int J Nanomedicine; 2012;**7**:6003;.**10.2147/IJN.S35347**

11. Ruparelia JP, Chatterjee AK, Duttagupta SP, Mukherji S; Strain specificity in antimicrobial activity of silver and copper nanoparticles; *Acta Biomater*; 2008;**4**(3):707-716;.**10.1016/j.actbio.2007.11.006**

12. Botequim D, Maia J, Lino MMF, Lopes LMF, Simões PN, Ilharco LM, et al.; Nanoparticles and Surfaces Presenting Antifungal, Antibacterial and Antiviral Properties; *Langmuir*; 2012;**28**(20):7646-7656;.**10.1021/la300948n**

13. Yliniemi K, Vahvaselkä M, Ingelgem YV, Baert K, Wilson BP, Terryn H, et al.; The formation and characterisation of ultra-thin films containing Ag nanoparticles; *J Mater Chem*; 2008;**18**(2):199-206;.**10.1039/B713313H**

14. Wang D, Li Y; Bimetallic Nanocrystals: Liquid-Phase Synthesis and Catalytic Applications; *Adv Mater*; 2011;**23**(9):1044-1060;.**10.1002/adma.201003695**

15. Pfeiffer TV, Feng J, Schmidt-Ott A; New developments in spark production of nanoparticles; *Adv Powder Technol*; 2014;**25**(1):56-70;.**10.1016/j.apt.2013.12.005**

16. Fraters BD, Cavaliere E, Mul G, Gavioli L; Synthesis of photocatalytic TiO2 nano-coatings by supersonic cluster beam deposition; *J Alloys Compd*; 2014;**615**:S467-S471;.**10.1016/j.jallcom.2013.12.037**

17. Chiodi M, Cheney CP, Vilmercati P, Cavaliere E, Mannella N, Weitering HH, et al.; Enhanced Dopant Solubility and Visible-Light Absorption in Cr–N Codoped TiO 2 Nanoclusters; *J Phys Chem C*; 2012;**116**(1):311-318;.**10.1021/jp208834n**

18. Cavaliere E, De Cesari S, Landini G, Riccobono E, Pallecchi L, Rossolini GM, et al.; Highly bactericidal Ag nanoparticle films obtained by cluster beam deposition; *Nanomedicine Nanotechnol Biol Med*; 2015;**11**(6):1417-1423;.**10.1016/j.nano.2015.02.023**

19. Principe L, Piazza A, Giani T, Bracco S, Caltagirone MS, Arena F, et al.; Epidemic Diffusion of OXA-23-Producing Acinetobacter baumannii Isolates in Italy: Results of the First Cross-Sectional Countrywide Survey; *J Clin Microbiol*; 2014;**52**(8):3004-3010;.**10.1128/JCM.00291-14**

20. Landini G, Riccobono E, Giani T, Arena F, Rossolini GM, Pallecchi L; Bactericidal activity of ceftaroline against mature Staphylococcus aureus biofilms; *Int J Antimicrob Agents*; 2015;**45**(5):551-553;.**10.1016/j.ijantimicag.2015.01.001**

21. Waterhouse GIN, Bowmaker GA, Metson JB; Interaction of a polycrystalline silver powder with ozone; *Surf Interface Anal*; 2002;**33**(5):401-409;.**10.1002/sia.1223**

22. Chastain J, King RC, Moulder J; *Handbook of X-Ray Photoelectron Spectroscopy: A Reference Book of Standard Spectra for Identification and Interpretation of XPS Data*; Physical Electronics Eden Prairie, MN; 1995.

23. Ferraria AM, Carapeto AP, Botelho do Rego AM; X-ray photoelectron spectroscopy: Silver salts revisited; *Vacuum*; 2012;**86**(12):1988-1991;.**10.1016/j.vacuum.2012.05.031**

24. Powell CJ; Recommended Auger parameters for 42 elemental solids; *J Electron Spectrosc Relat Phenom*; 2012;**185**(1-2):1-3;.**10.1016/j.elspec.2011.12.001**

25. Gaarenstroom SW, Winograd N; Initial and final state effects in the ESCA spectra of cadmium and silver oxides; *J Chem Phys*; 1977;**67**(8):3500-3506;.**10.1063/1.435347**

26. Kaushik VK; XPS core level spectra and Auger parameters for some silver compounds; *J Electron Spectrosc Relat Phenom*; 1991;**56**(3):273–277;.**10.1016/0368-2048(91)85008-H**

27. Sedona F, Rizzi GA, Agnoli S, Llabrés i Xamena FX, Papageorgiou A, Ostermann D, et al.; Ultrathin TiO_x Films on Pt(111): A LEED, XPS, and STM Investigation; *J Phys Chem B*; 2005;**109**(51):24411-24426;.**10.1021/jp0543173**

28. Contarini S, Van der Heide PAW, Prakash AM, Kevan L; Titanium coordination in microporous and mesoporous oxide materials by monochromated X-ray photoelectron spectroscopy and X-ray Auger electron spectroscopy; *J Electron Spectrosc Relat Phenom*; 2002;**125**(1):25–33;.**10.1016/S0368-2048(02)00041-5**

29. McCurdy PR, Sturgess LJ, Kohli S, Fisher ER; Investigation of the PECVD TiO2–Si(1 0 0) interface; *Appl Surf Sci*; 2004;**233**(1–4):69-79;.**10.1016/j.apsusc.2004.03.009**

30. Baletto F, Ferrando R; Structural properties of nanoclusters: Energetic, thermodynamic, and kinetic effects; *Rev Mod Phys*; 2005;**77**(1):371;.**10.1103/RevModPhys.77.371**

31. Barborini E, Piseri P, Milani P; A pulsed microplasma source of high intensity supersonic carbon cluster beams; *J Phys Appl Phys*; 1999;**32**(21):L105;.**10.1088/0022-3727/32/21/102**

32. Tafreshi HV, Piseri P, Barborini E, Benedek G, Milani P; Simulation on the effect of Brownian motion on nanoparticle trajectories in a pulsed microplasma cluster source; *J Nanoparticle Res*; 2002;**4**(6):511–524;.**10.1023/A:1022845401781**

33. Milani P, Iannotta S; *Cluster Beam Synthesis of Nanostructured Materials*; Springer Science & Business Media; 2012.

34. Tafreshi HV, Piseri P, Benedek G, Milani P; The Role of Gas Dynamics in Operation Conditions of a Pulsed Microplasma Cluster Source for Nanostructured Thin Films Deposition; *J Nanosci Nanotechnol*; 2006;**6**(4):1140-1149;.**10.1166/jnn.2006.139**

35. Jiang Q, Zhang S, Zhao M; Size-dependent melting point of noble metals; *Mater Chem Phys*; 2003;**82**(1):225-227;.**10.1016/S0254-0584(03)00201-3**

36. Lobato I, Rojas J, Landauro CV, Torres J; Atomic and electronic structure transformations of silver nanoparticles under rapid cooling conditions; *J Phys Condens Matter*; 2009;**21**(5):55301;.**10.1088/0953-8984/21/5/055301**

37. Asoro M, Damiano J, Ferreira P; Size Effects on the Melting Temperature of Silver Nanoparticles: In-Situ TEM Observations; *Microsc Microanal*; 2009;**15**(S2):706-707;.**10.1017/S1431927609097013**

Lasers Med Sci
DOI 10.1007/s10103-016-2025-5

ORIGINAL ARTICLE

The effects of diode laser on *Staphylococcus aureus* biofilm and *Escherichia coli* lipopolysaccharide adherent to titanium oxide surface of dental implants. An in vitro study

Marco Giannelli[1] · **Giulia Landini**[2] · **Fabrizio Materassi**[1] · **Flaminia Chellini**[3] · **Alberto Antonelli**[2,4] · **Alessia Tani**[3] · **Sandra Zecchi-Orlandini**[3] · **Gian Maria Rossolini**[2,4,5] · **Daniele Bani**[3]

Received: 18 December 2015 / Accepted: 4 July 2016
© Springer-Verlag London 2016

Abstract Effective decontamination of biofilm and bacterial toxins from the surface of dental implants is a yet unresolved issue. This in vitro study aims at providing the experimental basis for possible use of diode laser (λ 808 nm) in the treatment of peri-implantitis. *Staphylococcus aureus* biofilm was grown for 48 h on titanium discs with porous surface corresponding to the bone-implant interface and then irradiated with a diode laser (λ 808 nm) in noncontact mode with airflow cooling for 1 min using a Ø 600-μm fiber. Setting parameters were 2 W (400 J/cm^2) for continuous wave mode; 22 μJ, 20 kHz, 7 μs (88 J/cm^2) for pulsed wave mode. Bactericidal effect was evaluated using fluorescence microscopy and counting the residual colony-forming units. Biofilm and titanium surface morphology were analyzed by scanning electron microscopy (SEM). In parallel experiments, the titanium discs were coated with *Escherichia coli* lipopolysaccharide (LPS), laser-irradiated and seeded with RAW 264.7 macrophages to quantify LPS-driven inflammatory cell activation by measuring the enhanced generation of nitric oxide (NO). Diode laser irradiation in both continuous and pulsed modes induced a statistically significant reduction of viable bacteria and nitrite levels. These results indicate that in addition to its bactericidal effect laser irradiation can also inhibit LPS-induced macrophage activation and thus blunt the inflammatory response. The λ 808-nm diode laser emerges as a valuable tool for decontamination/detoxification of the titanium implant surface and may be used in the treatment of peri-implantitis.

Keywords Diode laser · Dental implants · Titanium oxide · *Staphylococcus aureus* · Lipopolysaccharide

✉ Marco Giannelli
dott.giannellimarco@gmail.com

[1] Odontostomatologic Laser Therapy Center, Via dell' Olivuzzo 162, 50143 Florence, Italy

[2] Department of Medical Biotechnologies, University of Siena, Santa Maria alle Scotte University Hospital, Viale Bracci, Siena, Italy

[3] Department of Experimental and Clinical Medicine - Section of Anatomy and Histology, Largo Brambilla 3, University of Florence, 50134 Florence, Italy

[4] Department of Experimental and Clinical Medicine, Section of Critical Care and Specialistic Medicine, University of Florence, and 5Clinical Microbiology and Virology Unit, Florence Careggi University Hospital, Via San Damiano, 50134 Florence, Italy

[5] Clinical Microbiology and Virology Unit, Florence Careggi University Hospital, Via San Damiano, 50134 Florence, Italy

Introduction

Peri-implantitis is one of the most severe complications of implant therapy: It is defined as an inflammatory reaction associated with loss of supporting bone around an implant in function [1]. According to the Consensus Report of the Sixth European Workshop in Periodontology (2008), implant therapy is associated with up to 80 % incidence of mucositis and 28–56 % incidence of peri-implantitis [2].

A substantial body of literature has shown that bacterial pathogens and their pro-inflammatory products, such as the bacterial endotoxin lipopolysaccharide (LPS), play a central role in pathogenesis of peri-implantitis and failing implants [3–5]. Many studies have shown that *Staphylococcus aureus* is one of the most common bacterial pathogens involved in the early failure of dental implants [6–9] as it efficiently attaches onto different titanium surfaces [10]. LPS is also regarded as a key factor implicated in peri-implantitis, since it has been reported to adhere tenaciously to dental titanium implants

Published online: 30 July 2016

and identified as a major factor of bacterial origin influencing bone resorption [11–13].

On these premises, an effective treatment of peri-implantitis should reach a dual goal: (i) remove bacteria and (ii) inactivate LPS present at the titanium interface with the host tissues [14]. Several methods of implant decontamination have been proposed for the treatment of peri-implantitis, including air-powered abrasive treatments, citric acid, mechanical cleaning with metal and plastic curettes or ultrasonic scalers [15–18], in combination with local and systemic antibiotic therapy [19, 20]. However, none of these methods gave satisfactory results in terms of eradication of bacteria from the contaminated implant surfaces [21, 22]. Paradoxically, a further release of LPS from dead bacteria might even enhance the inflammatory reaction around the dental implant. In the last decade, the positive effects of laser irradiation in cleaning and decontaminating the implant surfaces have been widely reported [23–26]. Various laser systems are in use in dental practice for different purposes: (i) Er:YAG laser was mainly used to ablate dental and bone hard tissues and to remove bacterial deposits and calculus from the dental and implant surfaces [23, 26]; (ii) Nd:YAG laser at low-power with high frequency irradiation was recognized to have bactericidal effects [27]; and (iii) diode laser was shown to be effective in the decontamination of implant surfaces with no side effects on the surrounding tissues [28]. In a previous study, we showed that irradiation with Nd:YAG laser, in addition to inducing bacterial implant decontamination, was capable of attenuating the LPS-induced inflammatory response [29]. Moreover, a recent study of our group has demonstrated that different titanium surfaces can greatly influence the temperature range measurable on the titanium target in response to laser diode (λ 808 nm) irradiation, highlighting the need to identify specific setting parameters to maintain the temperature below the tissue damage threshold, i.e. 50 °C [30]. Despite the numerous reports in the literature on the clinical use of lasers in implantology [31–34], little is known about the mechanisms by which lasers exert their effects on dental implant surfaces. Moreover, considering that the physical characteristics of implants vary greatly among different producers, there is no consensus on a standard laser-aided treatment for peri-implantitis.

In the present in vitro study, we investigated the effects of diode laser (λ 808 nm) in noncontact mode and in continuous or pulsed wave emission on both *S. aureus* biofilm and LPS adherent to titanium discs with rough titanium oxide coating reproducing the osseous interface of dental implants, in order to mimic the clinical conditions occurring at the implant/tissue interface.

Materials and methods

Materials The experiments were performed on titanium discs, 6 mm in diameter, 2 mm thick, with the same surface finish as the osseous interface (TiUnite) of dental implants (Nobel Biocare Services AG, Zürich, Switzerland). The discs were ultrasonically cleaned in acetone, rinsed in distilled water, and autoclaved at 121 °C for 15 min.

Bacterial biofilm formation *Staphylococcus aureus* strain ATCC 25923 was used for biofilm experiments. In a typical experiment, a suspension of about 3×10^5 CFU/ml was prepared in Tryptic Soy Broth (TSB, Oxoid, Milan, Italy) plus 0.5 % of D-glucose, in Tryptic Soy Agar (TSA, Oxoid). The bacterial suspension was dispensed in sterile 12-well polystyrene tissue culture plates (IWAKI microplate, Bibby Scientific Limited, Staffordshire, UK) (1.5 ml/well), and three discs were placed in each well. Biofilms were grown for 48 h at 35 °C (50 rpm in humid atmosphere), adding fresh medium (1.5 ml/well) after the first 24 h of incubation.

Laser treatment Prior to laser treatment, planktonic or loosely adherent bacterial cells were removed by gently rinsing twice the discs with 1.5-ml sterile phosphate-buffered saline (PBS). After that, the samples of *S. aureus* biofilm grown on titanium discs were placed on sterile slides and irradiated. The treatment was carried out for 1 min with a diode laser emitting at λ 808 nm (Dental Laser System 4 × 4™, General Project Ltd., Montespertoli, Florence, Italy) in noncontact mode through a polyimide-coated silica fiber (Ø 600 μm) positioned perpendicular to the disc surface. The fiber tip was kept at a distance of about 2–5 mm from the disc surface. To minimize heating, the laser beam was continuously moved to draw adjacent horizontal lines over the whole disc surface at a speed of 2.5 mm/s, under airflow cooling. Respect to random movements on the surface, this procedure assures a systematic irradiation of the whole disc without untreated zones. The detailed laser specification and irradiation parameters are reported in Table 1. During the treatment, the temperature of the titanium surface was measured by a thermal probe included

Table 1 Laser irradiation parameters

Operation mode	Continuous	Pulsed
Center wavelength (nm)	808 ± 10	808 ± 10
Frequency (Hz)	N.A.	20 kHz
Pulse on duration (μs)	N.A.	7
Duty cycle (%)	N.A.	14 %
Peak radiant power(W)	N.A.	3.1
Average radiant power (W)	2	0.44
Fiber diameter (μm)	600	600
Numeric aperture	0.22	0.22
Beam divergence (°)	25	25
Target diameter (mm)	6	6
Target area (cm^2)	0.3	0.3
Fluence at target surface (J/cm^2)	400	88

in the console of the laser and monitored by a thermal camera (Ti9, Fluke Corp., Everett, USA). The mean temperature was maintained below the 50 °C thermal damage threshold, as reported in preliminary experiments [30].

Viable cell count (CFU) after laser irradiation Following the laser treatment, the discs were transferred in 1.5-ml sterile tubes (one disc/tube) containing 500 μl of TSB plus 0.1 % Tween 20 (Sigma-Aldrich, Milan, Italy) as recovery medium [35]. To allow biofilm disgregation, each tube was vortexed for 30 s and sonicated for 30 min at 30 KHz and 300 W (Elma Transsonic T 460, Singen, Germany). After the second cycle of 30-s vortexing, serial dilutions in sterile saline solution were prepared, and 100 μl of each dilution was plated onto TSA and incubated for 24 h at 35 °C for CFU count (limit of detection = 5.0 CFU/disc). The experiments were performed in triplicate. Controls consisted of biofilms processed in the same way, excluding laser irradiation.

Fluorescence analysis Subsequent to the laser treatment, *S. aureus* biofilms formed on the titanium discs ($n = 9$) were stained with the fluorescent LIVE/DEAD BacLight™ (Invitrogen/Molecular Probes, Milan, Italy) solution for 2 min at 37 °C. The fluorescent kit contains a mixture of two dyes: SYTO 9 (green: excitation λ 488 nm, emission λ 500–540 nm) and propidium iodide (red: excitation λ 561 nm, emission λ 600–695 nm). SYTO 9 labels all bacteria, whereas propidium iodide enters only bacteria with damaged membranes. Thus, viable bacteria with intact cell membranes show green fluorescence, whereas dead bacteria with damaged membranes show red-yellow fluorescence. Labeled biofilms were washed twice with PBS, fixed with 0.5 % paraformaldehyde for 10 min and observed with a fluorescent microscope equipped with a digital camera (4000 B, Leica Microsystems, Milan, Italy). From each disc, three digital images (RGB color) from randomly selected microscopic fields were taken. Using ImageJ 1.42q software (http://rsb.info.nih.gov/ij), the green and red channels were split and the resulting two images were separately subjected to densitometry to evaluate the staining intensity of SYTO 9 and propidium iodide, corresponding to live and dead bacteria, respectively. Values were reported as means ± standard error of the mean (s.e.m.).

SEM To evaluate the possible morphological changes of the titanium surface and the bacterial biofilm after laser treatment, biofilm-coated titanium discs ($n = 9$) were subjected ($n = 6$) or not ($n = 3$) to laser irradiation. The negative control was an uncoated, un-irradiated disc. Upon sputter-coating with platinum (10 nm), the discs were examined with a Supra 40VP scanning electron microscope (Zeiss, Oberkochen, Germany) by a trained observer blinded to the experimental conditions.

Experiments on LPS-coated titanium discs In these experiments, we applied minor changes to the previously described method to study the effects of different laser treatments on LPS-induced inflammatory activation [5, 29]. Briefly, mouse RAW 264.7 macrophages obtained from the European Collection of Cell Cultures (ECACC, Salisbury, UK) were maintained in Dulbecco's modified Eagle medium (DMEM) supplemented with 10 % fetal bovine serum (FBS, Gibco Invitrogen, Milan, Italy), 100 U/ml penicillin-streptomycin, 200 mM L-glutamine (Sigma-Aldrich, Milan, Italy) and 4.5 g/l glucose, and cultured in 5 % CO_2 atmosphere at 37 °C. In each set of experiments, macrophages were seeded on titanium discs subjected to different pretreatments:

1. One disc was washed in sterile PBS, dried at 37 °C, and used as negative control.
2. Two discs were coated with LPS via immersion in a solution of *E. coli* LPS (Sigma-Aldrich, 50 μg/ml in PBS) for 15 min and dried at 37 °C for 1 h (positive control).
3. Six discs were LPS-coated, dried at 37 °C, and subjected to irradiation treatments detailed in Table 1.

The discs were then individually placed into the wells of a 96-well plate and RAW 264.7 macrophages (8×10^4 cells) were seeded on the discs and cultured in 250 μl of DMEM without phenol red, supplemented with 20 % of FBS, for 24 h. RAW 264.7 macrophages cultured alone in the same conditions without discs were used as basal controls. The generation of nitric oxide (NO), a typical reaction product of activated macrophages [36], was evaluated by measurement of nitrites, stable end-products of NO metabolism, in the conditioned medium of RAW 264.7 cells. The amounts of nitrites were determined spectrophotometrically by the Griess reaction, as previously described [37], and the optical density of the reaction product was measured at λ 546 nm with a Bio-Rad 550 microplate reader (Bio-Rad, Milan, Italy). Nitrite concentrations in the conditioned media were determined by comparison with standard concentrations of $NaNO_2$ dissolved in culture medium and expressed as nMol/ml. To assess RAW 264.7 cell viability upon the different treatments, the 3-(4,5-dimethylthiazol-2-yl)-2,5-diphenyl tetrazolium bromide (MTT) assay (Sigma-Aldrich) was used according to the manufacturer's instructions. After 24-h incubation and removal of the conditioned medium, MTT stock solution was added to each well and incubated for 4 h at 37 °C. Dimethyl sulfoxide was added to each well to dissolve the formazan crystals. The plate was gently shaken for 10 min and read at λ 550 nm with the microplate reader (Bio-Rad). Optical density (OD) was assumed as indicator of cell viability. The MTT data were used to normalize the production of nitrites by the amount of viable RAW 264.7 cells.

Statistical analysis The values are expressed as mean ± standard error of the mean (s.e.m.) of triplicate experiments.

Statistical analysis of differences between the experimental groups was performed using one-way ANOVA followed by Newman-Keuls multiple comparison test, and results were considered statistically significant if $p \leq 0.05$. Calculations were performed using the GraphPad Prism 4.0 statistical software (GraphPad, San Diego, CA, USA).

Results

Effect of laser treatment on S. aureus biofilm viability Adherent *S. aureus* biofilm onto TiUnite titanium discs ($n = 27$) was 7.3 ± 0.1 log CFU/disc (Fig. 1). The treatment with diode laser in both pulsed and continuous mode induced a statistically significant reduction of viable cell as compared with the untreated biofilm (1.5 and 2.2 log CFU/disc reduction, respectively: $p < 0.01$) (Fig. 1). In particular, the irradiation in continuous mode appeared to have a higher efficacy in terms of viability reduction, even if the comparison between the two treatments did not reach statistical significance ($p > 0.05$).

Fluorescence analysis of *S. aureus* biofilm viability The fluorescence analysis with BacLight staining method showed that, in comparison with the nonirradiated control discs, the diode laser used in pulsed or in continuous mode on *S. aureus* biofilm adherent to titanium discs caused a well-appreciable increase in the amount of red-stained dead bacteria in respect with green-stained viable ones (Fig. 2a). This visual finding was confirmed by densitometric analysis, which showed a remarkable, statistically significant increase ($p < 0.01$) in the percentage of dead over viable bacteria (Fig. 2b).

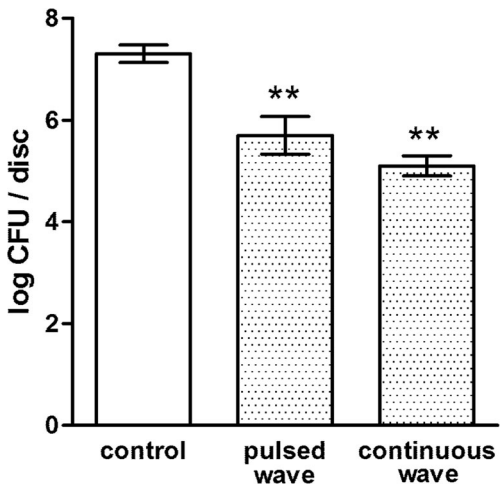

Fig. 1 Effect of the different laser treatments on decontamination of the titanium surface coated with *S. aureus* biofilm evaluated by residual bacterial growth. The *columns* represent the number of postirradiation *S. aureus* colonies grown upon 24-h incubation in selective medium. Values are means ± s.e.m. $*p < 0.05$; $**p < 0.01$ vs. controls

SEM examination of *S. aureus* biofilm morphology The surface of the titanium discs, analyzed by scanning electron microscope, revealed the presence of a titanium oxide layer with numerous micro-cavities, designed to favor colonization by cells of the peri-implant tissues and hence to increase osteoconductivity (Fig. 3a). Analysis of the titanium discs with 48-h bacterial coating (Fig. 3b) revealed the presence of an adherent layer of closely packed bacteria with the typical features of a biofilm, which partially filled the cavities present on the titanium surface. The laser treatment both in continuous (Fig. 3c) and pulsed (Fig. 3d) wave mode caused a sharp reduction of the amount of adherent bacteria. No clear difference was evident between the continuous and pulsed wave mode of irradiation.

Effect of laser treatment on LPS-induced macrophage activation Endogenous generation of NO/nitrites by activated RAW 264.7 macrophages was determined to investigate if the λ 808-nm diode laser was capable of inactivating the LPS adherent to titanium discs, thereby inhibiting macrophage activation (Fig. 4); the diode laser used in both continuous and pulsed wave mode caused a statistically significant decrease in nitrite production in comparison with the nonirradiated LPS-coated discs used as positive controls ($p < 0.001$).

Discussion

Decontamination of bacteria and bacterial toxins from implant surfaces is a prerequisite to arrest the progression of peri-implantitis and for a successful treatment of failing implants. It has been shown that *S. aureus*, a Gram-positive bacterium, has an increased affinity to titanium substrates, being consistently found adherent to the surface of implants, particularly those with a rough surface finish [10, 38, 39]. *S. aureus* has been frequently isolated from failing dental implant sites and associated with poor clinical outcome [40]. LPS, the Gram-negative endotoxin, has received considerable attention because of its crucial role as a mediator of peri-implant inflammation [41]. Therefore, for a successful treatment of peri-implant disease, it is mandatory to eliminate bacteria and, in the meantime, remove all bacterial by-products and toxins which can hinder tissue regrowth on implant surfaces and osteo-integration.

The present findings offer evidence that the λ 808-nm diode laser can achieve an efficient reduction of *S. aureus* biofilm and detoxification of LPS on the tested titanium surface. In particular, 1-min irradiation of the biofilm-coated discs was able to reduce the number of colony forming units of 99 and 94 % for continuous and pulsed wave mode, respectively. Scanning electron microscopy (SEM) analysis of the titanium discs revealed that, with the adopted irradiation procedure, the λ 808-nm diode laser did not alter the original features of the

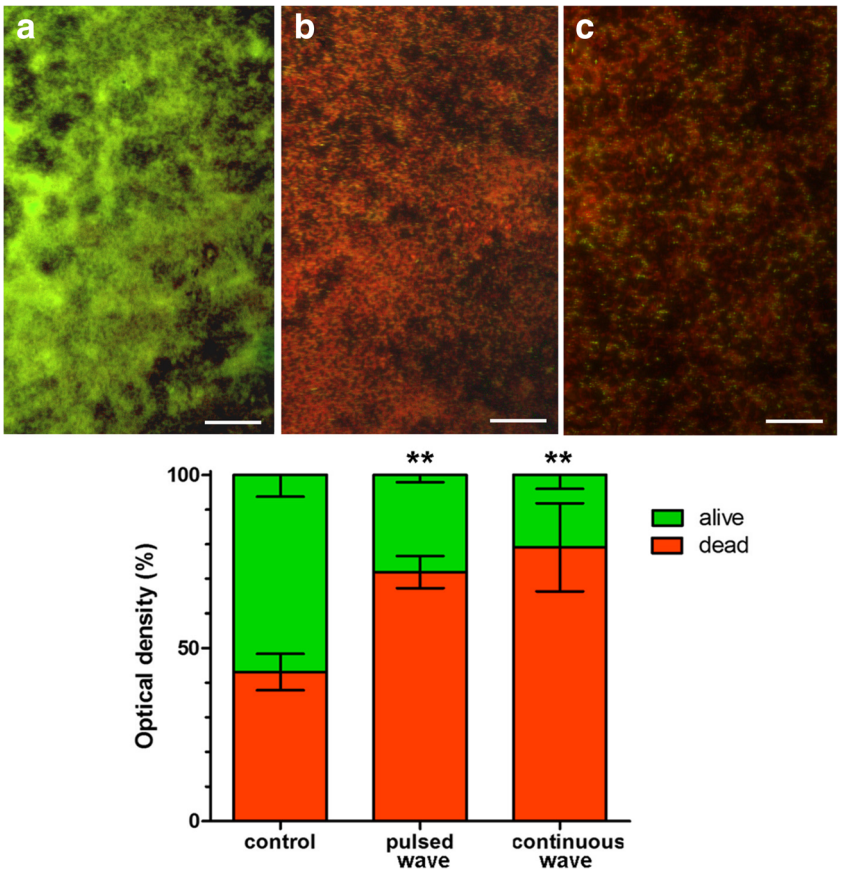

Fig. 2 Effect of the different laser treatments on decontamination of the titanium surface coated with *S. aureus* biofilm evaluated by BacLight fluorescent vital stain. **a** Untreated control shows mostly viable bacteria (*green*). Upon irradiation in pulsed (**b**) or continuous (**c**) wave modes, most bacteria appear dead (*red*). *Bars* = 100 μm. In **d**, the corresponding densitometric analysis is shown. Values are means ± s.e.m. $^{**}p < 0.01$ vs. controls

titanium oxide surface layer, characterized by micro-roughness and micro-pores. However, despite the remarkable reduction of microbial load upon laser treatment, the present findings showed that a complete decontamination and cleaning of the titanium discs were not achieved, as can be argued by the detection of residual organic remnants of the bacterial biofilm on the targeted surfaces by SEM and fluorescence analyses. On the other hand, our data indicated that both continuous and pulsed wave laser irradiation were capable of inactivating the titanium-adherent LPS, as judged by failed induction of inflammatory activation of RAW 264.7 macrophages used as a probe to measure LPS bioactivity.

A decontaminating potential of λ 808-nm diode laser had been previously shown in vitro [42] as well as on intraoral biofilms grown on rough titanium surfaces [43]. The present findings confirm and extend this notion, although our results are difficult to compare with the previous ones because of substantially different irradiation parameters, treatment modalities and physical-chemical characteristics of the targeted titanium surfaces. It has been reported that Gram-negative species show immediate structural damage after treatment with λ 808-nm diode laser, whereas Gram-positive micro-organisms require repeated irradiations [44]. Our study provides experimental evidence that, with proper irradiation modes and parameters, the λ 808-nm diode laser is endowed with a reasonable activity against the *S. aureus* biofilm and pro-inflammatory bacterial by-products, such as LPS, adherent to the titanium surface. This effect was exerted in the absence of alterations of titanium surface morphology and below the threshold for thermal tissue damage. This decrease in bacterial load can reestablish a more favorable balance between peri-implant microbiota and host defenses, allowing a stable clinical improvement over time [45].

A limitation of the present study is the fact that the treatments were performed on new, clean discs in simplified and highly standardized laboratory conditions, which are substantially different from a real clinic situation of laser-aided implant surgery, where a dental implant has a markedly different mass and surface geometry, is interlocked with peri-implant bone, and can be covered by subgingival plaque, blood, inflammatory cells, proteins, and calculus. Another limitation comes from the fact that we did not compare this laser treatment with other decontaminating procedures. Therefore, caution is required when extrapolating the present findings to clinical practice. In addition, further studies are necessary to evaluate the effects of λ 808-nm diode laser on a broader spectrum of oral micro-organisms and for longer irradiation times.

In conclusion, our data suggest that the λ 808-nm diode laser can be considered a valuable tool for bacteria/LPS reduction adherent to the titanium oxide

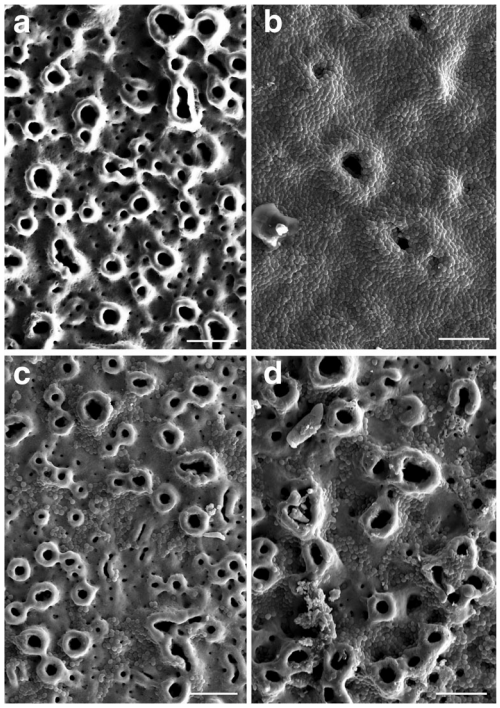

Fig. 3 Representative scanning electron micrographs of uncoated (**a**) and biofilm-coated titanium discs from **b** untreated control, showing a dense bacterial layer masking the roughness of the titanium oxide surface, and **c** pulsed and **d** continuous wave laser irradiation, showing an almost complete removal of the biofilm coating and few residual bacteria. *Bars* = 10 μm

implant surface, which in turn may increase the odds of successful control of peri-implant disease.

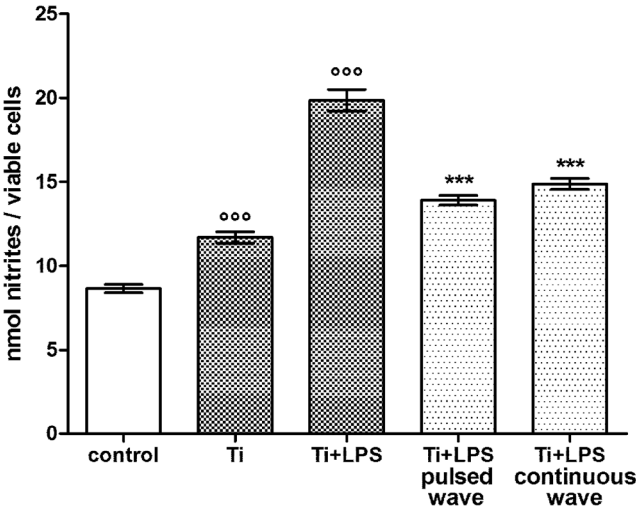

Fig. 4 Effect of the different laser treatments on detoxification of the titanium surface coated with bacterial LPS evaluated by RAW 264.7 macrophage activation. The *columns* represent the amount of nitrites, an index of LPS-induced iNOS activation and nitric oxide generation, in the cells' conditioned medium, normalized by the amount of viable cells. Control indicates cell grown in standard conditions, *Ti* indicates cells grown on uncoated titanium discs, and *Ti + LPS* indicates cells grown on LPS-coated titanium discs. Values are means ± s.e.m. °°°$p < 0.001$ vs. the control; ***$p < 0.001$ vs. Ti + LPS

Acknowledgments The authors are grateful to Dr. Peter Schüpbach, from Schüpbach Ltd. (Thalwil, Switzerland) for conducting the SEM investigation and Dr. Waldemar Hoffmann, Nobel Biocare Services AG (Zürich, Switzerland) for reviewing the manuscript.

This study was supported in part by General Project Ltd. (Montespertoli, Florence, Italy).

Compliance with ethical standards

Conflict of interest The authors declare that they have no conflict of interest.

References

1. Zitzmann NU, Berglundh T (2008) Definition and prevalence of peri-implant diseases. J Clin Periodontol 35:286–291
2. Lindhe J, Meyle J (2008) Group D of european workshop on periodontology. "Peri-implant diseases: consensus report of the sixth european workshop on periodontology". J Clin Periodontol 35: 282–285
3. Nouneh RA, Wataha JC, Hanes PJ, Lockwood PE (2001) Effect of lipopolysaccharide contamination on the attachment of osteoblast-like cells to titanium and titanium alloy in vitro. J Oral Implantol 27: 174–179
4. Greenfield EM, Bi Y, Ragab AA, Goldberg VM, Nalepka JL, Seabold JM (2005) Does endotoxin contribute to aseptic loosening of orthopedic implants? J Biomed Mater Res B Appl Biomater 72: 179–185
5. Giannelli M, Pini A, Formigli L, Bani D (2011) Comparative in vitro study among the effects of different laser and LED irradiation protocols and conventional chlorhexidine treatment for deactivation of bacterial lipopolysaccharide adherent to titanium surface. Photomed Laser Surg 29:573–580
6. Shrestha B, Theerathavaj ML, Thaweboon S, Thaweboon B (2012) In vitro antimicrobial effects of grape seed extract on peri-implantitis microflora in craniofacial implants. Asian Pac J Trop Biomed 2:822–825
7. Cortizo AM, Fernández Lorenzo de Mele MA (2012) Chlorhexidine delivery system from titanium/polybenzyl acrylate coating: evaluation of cytotoxicity and early bacterial adhesion. J Dent 40:329–337
8. Zhao B, van der Mei HC, Subbiahdoss G, de Vries J, Rustema-Abbing M, Kuijer R, Busscher HJ, Ren Y (2014) Soft tissue integration versus early biofilm formation on different dental implant materials. Dent Mater 30:716–727
9. Thurnheer T, Belibasakis GN (2015) Incorporation of staphylococci into titanium-grown biofilms: an in vitro "submucosal" biofilm model for peri-implantitis. Clin Oral Implants Res. doi:10.1111/clr.12715
10. Harris LG, Richards RG (2004) Staphylococcus aureus adhesion to different treated titanium surfaces. J Mater Sci Mater Med 15:311–314
11. Nelson SK, Knoernschild KL, Robinson FG, Schuster GS (1997) Lipopolysaccharide affinity for titanium implant biomaterials. J Prosthet Dent 77:76–82
12. Dixon DR, Darveau RP (2005) Lipopolysaccharide heterogeneity: innate host responses to bacterial modification of lipid A structure. J Dent Res 84:584–595
13. Ozaki Y, Ukai T, Yamaguchi M et al (2009) Locally administered T cells from mice immunized with lipopolysaccharide (LPS) accelerate LPS-induced bone resorption. Bone 44:1169–1176
14. Renvert S, Samuelsson E, Lindahl C, Persson GR (2009) Mechanical non-surgical treatment of peri-implantitis: a double-

blind randomized longitudinal clinical study. I: clinical results. J Clin Periodontol 36:604–609
15. Fox SC, Moriarty JD, Kusy RP (1990) The effects of scaling a titanium implant surface with metal and plastic instruments: an in vitro study. J Periodontol 61:485–490
16. Suarez F, Monje A, Galindo-Moreno P, Wang HL (2013) Implant surface detoxification: a comprehensive review. Implant Dent 22: 465–473
17. Mettraux GR, Sculean A, Bürgin WB, Salvi GE (2015) Two-year clinical outcomes following non-surgical mechanical therapy of peri-implantitis with adjunctive diode laser application. Clin Oral Implants Res. doi:10.1111/clr.12689
18. Sahrmann P, Ronay V, Hofer D, Attin T, Jung RE, Schmidlin PR (2015) In vitro cleaning potential of three different implant debridement methods. Clin Oral Implants Res 26:314–319
19. Dörtbudak O, Haas R, Bernhart T, Mailath-Pokorny G (2001) Lethal photosensitization for decontamination of implant surfaces in the treatment of peri-implantitis. Clin Oral Implants Res 12:104–108
20. Javed F, Alghamdi AS, Ahmed A, Mikami T, Ahmed HB, Tenenbaum HC (2013) Clinical efficacy of antibiotics in the treatment of peri-implantitis. Int Dent J 63:169–176
21. Mouhyi J, Sennerby L, Pireaux JJ, Dourov N, Nammour S, Van Reck J (1998) An XPS and SEM evaluation of six chemical and physical techniques for cleaning of contaminated titanium implants. Clin Oral Implants Res 9:185–194
22. Mouhyi J, Sennerby L, Van Reck J (2000) The soft tissue response to contaminated and cleaned titanium surfaces using CO2 laser, citric acid and hydrogen peroxide. An experimental study in the rat abdominal wall. Clin Oral Implants Res 11:93–98
23. Kreisler M, Götz H, Duschner H (2002) Effect of Nd:YAG, Ho: YAG, Er:YAG, CO2, and GaAIAs laser irradiation on surface properties of endosseous dental implants. Int J Oral Maxillofac Implants 17:202–211
24. Sculean A, Schwarz F, Becker J (2005) Anti-infective therapy with an Er:YAG laser: influence on peri-implant healing. Expert Rev Med Devices 2:267–276
25. Roncati M, Lucchese A, Carinci F (2013) Non-surgical treatment of peri-implantitis with the adjunctive use of an 810-nm diode laser. J Indian Soc Periodontol 17:812–815
26. Aoki A, Mizutani K, Schwarz F, Sculean A, Yukna RA, Takasaki AA, Romanos GE, Taniguchi Y, Sasaki KM, Zeredo JL, Koshy G, Coluzzi DJ, White JM, Abiko Y, Ishikawa I, Izumi Y (2015) Periodontal and peri-implant wound healing following laser therapy. Periodontol 68:217–269
27. Giannini R, Vassalli M, Chellini F, Polidori L, Dei R, Giannelli M (2006) Neodymium:yttrium aluminum garnet laser irradiation with low pulse energy: a potential tool for the treatment of peri-implant disease. Clin Oral Implants Res 17:638–643
28. Romanos GE, Everts H, Nentwig GH (2000) Effects of diode and Nd: YAG laser irradiation on titanium discs: a scanning electron microscope examination. J Periodontol 71:810–815
29. Giannelli M, Bani D, Tani A, Pini A, Margheri M, Zecchi-Orlandini S, Tonelli P, Formigli L (2009) In vitro evaluation of the effects of low-intensity Nd:YAG laser irradiation on the inflammatory reaction elicited by bacterial lipopolysaccharide adherent to titanium dental implants. J Periodontol 80:977–984
30. Giannelli M, Lasagni M, Bani D (2015) Thermal effects of λ = 808 nm GaAlAs diode laser irradiation on different titanium surfaces. Lasers Med Sci 30:2341–2352
31. Romanos GE, Gutknecht N, Dieter S, Schwarz F, Crespi R, Sculean A (2009) Laser wavelengths and oral implantology. Lasers Med Sci 24:961–970
32. Subramani K, Wismeijer D (2012) Decontamination of titanium implant surface and re-osseointegration to treat peri-implantitis: a literature review. Int J Oral Maxillofac Implants 27:1043–1054
33. Romanos GE, Gupta B, Yunker M, Romanos EB, Malmstrom H (2013) Lasers use in dental implantology. Implant Dent 22:282–288
34. Yan M, Liu M, Wang M, Yin F, Xia H (2015) The effects of Er: YAG on the treatment of peri-implantitis: a meta-analysis of randomized controlled trials. Lasers Med Sci 30:1843–1853
35. Harrison JJ, Stremick CA, Turner RJ, Allan ND, Olson ME, Ceri H (2010) Microtiter susceptibility testing of microbes growing on peg lids: a miniaturized biofilm model for high-throughput screening. Nat Protoc 5:1236–1254
36. Moncada S, Palmer RM, Higgs EA (1991) Nitric oxide: physiology, pathophysiology, and pharmacology. Pharmacol Rev 43:109–142
37. Masini E, Nistri S, Vannacci A, Bani Sacchi T, Novelli A, Bani D (2004) Relaxin inhibits the activation of human neutrophils: involvement of the nitric oxide pathway. Endocrinology 145:1106–1112
38. Izquierdo-Barba I, García-Martín JM, Álvarez R, Palmero A, Esteban J, Pérez-Jorge C, Arcos D, Vallet-Regí M (2015) Nanocolumnar coatings with selective behavior towards osteoblast and Staphylococcus aureus proliferation. Acta Biomater 15:20–28
39. Aguayo S, Donos N, Spratt D, Bozec L (2015) Nanoadhesion of staphylococcus aureus onto titanium implant surfaces. J Dent Res 94:1078–1084
40. Lee A, Wang HL (2010) Biofilm related to dental implants. Implant Dent 19:387–393
41. Barão VA, Mathew MT, Assunção WG, Yuan JC, Wimmer MA, Sukotjo C (2011) The role of lipopolysaccharide on the electrochemical behavior of titanium. J Dent Res 90:613–618
42. Kreisler M, Kohnen W, Marinello C, Schoof J, Langnau E, Jansen B, d'Hoedt B (2003) Antimicrobial efficacy of semiconductor laser irradiation on implant surfaces. Int J Oral Maxillofac Implants 18: 706–711
43. Sennhenn-Kirchner S, Klaue S, Wolff N, Mergeryan H, Borg von Zepelin M, Jacobs HG (2007) Decontamination of rough titanium surfaces with diode lasers: microbiological findings on in vivo grown biofilms. Clin Oral Implants Res 18:126–132
44. Schoop U, Kluger W, Moritz A, Nedjelik N, Georgopoulos A, Sperr W (2004) Bactericidal effect of different laser systems in the deep layers of dentin. Lasers Surg Med 35:111–116
45. Mombelli A (2002) Microbiology and antimicrobial therapy of peri-implantitis. Periodontol 28:177–189

Journal of Antimicrobial Chemotherapy Advance Access published June 21, 2016

J Antimicrob Chemother
doi:10.1093/jac/dkw227

Journal of Antimicrobial Chemotherapy

Characterization of KPC-encoding plasmids from two endemic settings, Greece and Italy

Costas C. Papagiannitsis[1,2]†, Vincenzo Di Pilato[3,4]†, Tommaso Giani[3], Panagiota Giakkoupi[1], Eleonora Riccobono[3,5], Giulia Landini[3], Vivi Miriagou[6], Alkiviadis C. Vatopoulos[1,7] and Gian Maria Rossolini[3,5,8,9]*

[1]Department of Microbiology, National School of Public Health, Athens, Greece; [2]Department of Microbiology, Faculty of Medicine and University Hospital in Plzen, Charles University in Prague, Plzen, Czech Republic; [3]Department of Medical Biotechnologies, University of Siena, Siena, Italy; [4]Department of Surgery and Translational Medicine, University of Florence, Florence, Italy; [5]Department of Experimental and Clinical Medicine, University of Florence, Florence, Italy; [6]Laboratory of Bacteriology, Hellenic Pasteur Institute, Athens, Greece; [7]Central Public Health Laboratory, Hellenic Centre of Disease Control and Prevention, Vari, Greece; [8]Microbiology and Virology Unit, Careggi University Hospital, Florence, Italy; [9]Don Carlo Gnocchi Foundation, Florence, Italy

*Corresponding author. Department of Experimental and Clinical Medicine, University of Florence, Via San Damiano, 50134 Florence, Italy.
E-mail: gianmaria.rossolini@unifi.it
†These authors contributed equally to this study.

Received 7 February 2016; returned 8 April 2016; revised 4 May 2016; accepted 13 May 2016

Objectives: Global dissemination of KPC-type carbapenemases is mainly associated with the spread of high-risk clones of *Klebsiella pneumoniae* and of KPC-encoding plasmids. In this study, we explored the population structure of KPC-encoding plasmids from the recent epidemics of KPC-producing *K. pneumoniae* (KPC-Kp) in Greece and Italy, the two major European endemic settings.

Methods: Thirty-four non-replicate clinical strains of KPC-Kp representative of the early phases (2008–11) of the Greek ($n=22$) and Italian ($n=12$) epidemics were studied. Isolates were typed by MLST, and bla_{KPC}-carrying plasmids were characterized by S1 profiling, PCR-based replicon typing and RFLP. Transfer experiments by conjugation or transformation were carried out with *Escherichia coli* recipients. Eleven plasmids, representative of all different restriction profiles, were completely sequenced.

Results: The representative Greek strains belonged to 14 sequence types (STs), with a predominance of ST258. The representative Italian strains belonged to three STs, with a predominance of clonal complex 258 (ST258, ST512). The 34 strains carried plasmids of variable size (78–166 kb), either with bla_{KPC-2} or bla_{KPC-3} gene embedded in a Tn*4401a* transposon. Plasmids from Greek strains were mostly of a single RFLP type (A) and resembled the archetypal pKpQIL KPC-encoding plasmid, while plasmids from Italian strains belonged to a more heterogeneous population, showing five RFLP profiles (A, C–F). Types A and C resembled pKpQIL or deletion derivatives thereof, while types D–F included plasmids with hybrid structures between pKpQIL, pKPN3 and pKPN101-IT.

Conclusions: pKpQIL-like plasmids played a major role in the dissemination of bla_{KPC} in Greece and Italy, but evolved with different dynamics in these endemic settings.

Introduction

In recent years, carbapenem-resistant *Klebsiella pneumoniae* producing KPC-type carbapenemases (KPC-Kp) have emerged as challenging pathogens causing healthcare-associated infections, due to their extremely drug-resistant phenotypes and ability to cause infections associated with high mortality.[1] KPC-Kp have shown a remarkable ability to spread, and in some settings have established high-level endemicity.[2,3] In Europe, Greece and Italy are the most affected countries, with high proportions of KPC-Kp.[3] Strains belonging in clonal complex (CC) 258 have been the major ones responsible for epidemic diffusion of KPC-Kp in Greece and Italy. However, some clonal diversification has been reported in Greece[4,5] and subsequently in Italy.[6]

Most of the $bla_{KPC-type}$ genes are located on Tn*4401*-like transposons carried by transferable plasmids.[7] To date, several types of KPC-encoding plasmids belonging to various incompatibility (Inc) groups have been reported, including IncN, IncL/M, IncFII, IncR, IncX, ColE1 and untypeable.[8]

In *K. pneumoniae*, IncFII plasmids appeared to be the most widespread, and pKpQIL was the first characterized $IncFII_{K2}$ bla_{KPC}-carrying plasmid in Israel in 2006, and associated with ST258.[8–10] Subsequently, pKpQIL-like plasmids have been reported in several other countries,[11–16] being identified in

© *The Author 2016. Published by Oxford University Press on behalf of the British Society for Antimicrobial Chemotherapy. All rights reserved. For Permissions, please e-mail: journals.permissions@oup.com*

Downloaded from http://jac.oxfordjournals.org/ at Universia degli Studi di Siena on June 29, 2016

KPC-Kp strains responsible for several epidemics.[2,10] To date, several IncFII KPC-encoding plasmids have been completely sequenced and characterized, including either K1 or K2 sublineages.[9,12,17,18] However, few studies have investigated the complete sequence of KPC-encoding plasmids among large KPC-Kp collections,[14,16,18,19] and none of them in the endemic settings of Greece and Italy.

In the present study, we characterized KPC-encoding plasmids of representative *K. pneumoniae* clinical strains, associated with the emergence and dissemination of KPC-Kp in Greece and Italy.

Materials and methods

Bacterial isolates

Thirty-four non-replicate KPC-Kp clinical strains representative of the early phases of the Greek and Italian epidemics were studied (Table 1).[20–23] The selection was designed to include strains of all different PFGE patterns observed in Greece during the period 2008–11 ($n=22$ strains, from a total of 933 non-replicate KPC-Kp isolates from 40 hospitals),[4] and in Italy during the first nationwide survey on carbapenem-resistant Enterobacteriaceae, carried out in 2011 ($n=11$, from a total of 204 non-replicate KPC-Kp isolates from 25 hospitals).[22] The Italian KPC-Kp index strain, isolated in 2008,[21] was also included. MLST was carried out as previously described for all isolates for which these data were not previously available[24] and STs were assigned using the database available at http://www.pasteur.fr/mlst.

Molecular analysis and transferability of bla_{KPC} genes

Detection of bla_{KPC} genes and mapping of the Tn*4401* transposon were performed by PCR and sequencing.[25] Size of the KPC-encoding plasmids was assessed by PFGE of total DNA digested with S1 nuclease (PFGE-S1),[26] followed by hybridization with a digoxigenin-labelled bla_{KPC}-specific probe (Roche Diagnostics GmbH, Mannheim, Germany).

Conjugal transfer of bla_{KPC}-harbouring plasmids from the KPC-Kp clinical strains was carried out in mixed broth cultures,[27] using the streptomycin-resistant *Escherichia coli* 1R716 laboratory strain (F− *lac his pro trp* Str^R) as recipient;[28] transconjugants were selected on MacConkey agar plates supplemented with streptomycin (1500 mg/L) and ampicillin (50 mg/L), and replica-plated on LB agar plates containing ertapenem (0.5 mg/L). The transfer frequency was expressed as the number of transconjugants per donor cells. Plasmid DNA from strains that failed to transfer bla_{KPC} by conjugation was extracted using a Nucleobond AX Midi Kit (Macherey-Nagel, Düren, Germany) and used to transform *E. coli* DH10B (Invitrogen) competent cells by electroporation.[29] Transformants were selected on LB agar plates with ampicillin (50 mg/L), followed by replica plating on LB agar plates containing ertapenem (0.5 mg/L). Additional conjugal transfer experiments were carried out with two plasmids (pGR-1504 and pGR-3913), selected for being almost identical but showing a different transfer behaviour, using *E. coli* DH10B transformants (DH10B/pGR-1504 and DH10B/pGR-3913) as donors and *E. coli* J53Azi^R (*met pro*) as recipient. In this case, transconjugants were selected on LB agar plates plus sodium azide (100 mg/L) and ampicillin (100 mg/L). Transfer of bla_{KPC} to transconjugants or transformants was always confirmed by PCR targeting the bla_{KPC} gene.

Plasmid typing

Plasmids from transconjugants or transformants were extracted using the Qiagen Large-Construct Kit (Qiagen, Hilden, Germany). For RFLP analysis, plasmids were digested with PstI endonuclease and restriction fragments were separated by electrophoresis in 1.0% agarose gel. The genetic relatedness among plasmids was determined by the number of band differences observed in the RFLP profiles. RFLP profiles that differed by ≤3 bands were considered to be within the same restriction pattern type (e.g. A). Additionally, plasmids with RFLP profiles that differed by ≤1 band were assigned to the same subtype (e.g. A1). Plasmid incompatibility groups were determined by PCR-based replicon typing.[30,31] IncF plasmids were further characterized by replicon sequence typing and by a specific PCR assay for the presence of the FIB-like *repA* gene,[11,32] which was previously identified within the pKPN4-derived region of several pKpQIL-like plasmids.[9]

Plasmid sequencing and bioinformatics

Eleven plasmids were selected for complete sequencing. Among these, nine plasmids were selected as representatives of all different RFLP types and subtypes (two from Greek strains and seven from Italian strains). Additionally, two more plasmids belonging to the major RFLP profile were selected for studying their different transferability behaviour (Table 1).

Whole sequencing was performed using the Illumina MiSeq platform (Illumina Inc., San Diego, CA, USA) on plasmid DNA preparations extracted from *E. coli* transconjugants/transformants, as described above. Reads were assembled using the ABySS *de novo* assembler and gaps were filled by a PCR-based strategy and Sanger sequencing.[33] For sequence analysis and annotation, the BLAST algorithm (www.ncbi.nlm.nih.gov/BLAST), ISFinder database (www-is.biotoul.fr/) and ORF finder tool (http://www.bioinformatics.org/sms2/orf_find.html) were utilized. Comparative genome alignments and SNP count were performed using Mauve 2.3.1.[34]

Nucleotide sequence accession numbers

Sequenced plasmids were named according to the code of the cognate strains. The nucleotide sequences of the KPC-encoding plasmids pGR-1504, pGR-1780, pGR-1870 and pGR-3913 from *K. pneumoniae* strains recovered in Greece have been deposited in GenBank under accession numbers KF874496, KF874497, KF874498 and KF874499, respectively. The bla_{KPC}-carrying plasmids pIT-01C03, pIT-12C47, pIT-12C73, pIT-01C22, pIT-11C07, pIT-06C07 and pIT-FIPP-1 from Italian *K. pneumoniae* strains were deposited in GenBank under accession numbers HG969995, HG969996, LT009689, HG969997, HG969998, LT009688 and HG969999, respectively.

Results and discussion

KPC-Kp strains from early phases of the Greek and Italian epidemics, and plasmid diversity

The 34 KPC-Kp strains comprised 16 different STs with a notable diversity observed among Greek isolates, likely reflecting the earlier emergence of KPC-Kp in this country and the larger number of studied isolates, while the diversity among Italian isolates was considerably lower, with most of them belonging in CC258 (Table 1). All the Greek strains carried bla_{KPC-2}, while Italian strains carried either bla_{KPC-3} ($n=7$) or bla_{KPC-2} ($n=5$). Characterization of the bla_{KPC} genetic context by PCR mapping and sequencing showed that all strains harboured the Tn*4401a* isoform of the Tn*4401* transposon.[25]

Southern blotting on PFGE-S1 of KPC-Kp revealed that the majority of plasmids sized ∼110 kb ($n=30$, from both Greece and Italy), while the remaining were ∼80 kb ($n=3$, from Italy) or ∼150 kb ($n=1$, from Italy) (Table 1). All KPC-encoding plasmids were transferred by conjugation ($n=10$) or transformation ($n=24$) from the clinical strains (Table 1).

RFLP analysis of plasmid DNAs extracted from the *E. coli* transconjugants/transformants revealed six types of restriction patterns (A–F), with type A being the most prevalent and including three

Downloaded from http://jac.oxfordjournals.org/ at Universia degli Studi di Siena on June 29, 2016

Table 1. List of KPC-Kp strains selected as representative of the Greek and Italian epidemics

Strain	Year of isolation	Geographical region	Sequence type (CC)	KPC allele	Size of bla_{KPC} plasmids[a] (kb)	Conjugal transfer frequencies[b]	RFLP type	Replicon(s)	Ref.
GR-1370	2008	Greece, Chania	160	2	≈110	2×10^{-7}	**A0**	FII_{K2}-FIB	5
GR-1504	**2008**	**Greece, Athens**	**258 (CC258)**	**2**	**≈110 (113.640)**	**BLD**[c]	**A0**	**FII_{K2}-FIB**	5
GR-1516	2008	Greece, Athens	17	2	≈110	5×10^{-6}	**A0**	FII_{K2}-FIB	5
GR-1725	2008	Greece, Athens	494	2	≈110	1×10^{-7}	**A0**	FII_{K2}-FIB	5
GR-1780	**2009**	**Greece, Heraklion**	**147**	**2**	**≈110 (113.622)**	**8×10^{-8}**	**A0**	**FII_{K2}-FIB**	20
GR-1825	2009	Greece, Kavala	258 (CC258)	2	≈110	BLD	**A0**	FII_{K2}-FIB	4
GR-1841	2009	Greece, Athens	133	2	≈110	1×10^{-6}	**A0**	FII_{K2}-FIB	4
GR-1997	2009	Greece, Athens	383	2	≈110	BLD	**A0**	FII_{K2}-FIB	4
GR-2015	2009	Greece, Athens	274	2	≈110	6×10^{-8}	**A0**	FII_{K2}-FIB	4
GR-2138	2009	Greece, Thessaloniki	86	2	≈110	2×10^{-6}	**A0**	FII_{K2}-FIB	4
GR-2312	2009	Greece, Athens	495	2	≈110	7×10^{-7}	**A0**	FII_{K2}-FIB	4
GR-2868	2010	Greece, Athens	383	2	≈110	BLD	**A0**	FII_{K2}-FIB	23
GR-2878	2010	Greece, Athens	832	2	≈110	BLD	**A0**	FII_{K2}	23
GR-2951	2010	Greece, Thessaloniki	147	2	≈110	BLD	**A0**	FII_{K2}-FIB	23
GR-3003	2010	Greece, Athens	258 (CC258)	2	≈110	BLD	**A0**	FII_{K2}-FIB	23
GR-3913	**2011**	**Greece, Athens**	**35**	**2**	**≈110 (113.640)**	**4×10^{-7}**	**A0**	**FII_{K2}-FIB**	this study
GR-3956	2011	Greece, Rhodes Island	258 (CC258)	2	≈110	BLD	**A0**	FII_{K2}-FIB	this study
GR-4077	2011	Greece, Heraklion	258 (CC258)	2	≈110	BLD	**A0**	FII_{K2}-FIB	this study
GR-4294	2011	Greece, Thessaloniki	147	2	≈110	BLD	**A0**	FII_{K2}-FIB	this study
GR-4406	2011	Greece, Athens	792	2	≈110	3×10^{-6}	**A0**	FII_{K2}-FIB	this study
GR-4407	2011	Greece, Thessaloniki	383	2	≈110	BLD	**A0**	FII_{K2}-FIB	this study
GR-1870	**2009**	**Greece, Agios Niokolaos**	**11**	**2**	**≈110 (116.047)**	**BLD**	**B0**	**FII_{K2}-FIB**	4
IT-03C06	2011	Italy, Lecco	512 (CC258)	3	≈110	BLD	**A1**	FII_{K2}-FIB	22
IT-01C03	**2011**	**Italy, Milan**	**258 (CC258)**	**2**	**≈110 (113.642)**	**BLD**	**A1**	**FII_{K2}-FIB**	22
IT-01C22	**2011**	**Italy, Milan**	**512 (CC258)**	**3**	**≈110 (114.173)**	**BLD**	**A2**	**FII_{K2}-FIB**	22
IT-FIPP-1	**2008**	**Italy, Florence**	**258 (CC258)**	**3**	**≈80 (78.232)**	**BLD**	**C0**	**FIB**	21
IT-PA3	2011	Italy, Palermo	258 (CC258)	3	≈80	BLD	**C0**	FIB	22
IT-24C02	2011	Italy, Catania	258 (CC258)	3	≈80	BLD	**C0**	FIB	22
IT-11C07	**2011**	**Italy, Modena**	**512 (CC258)**	**3**	**≈110 (103.164)**	**BLD**	**D0**	**FII_{K2}-FIB**	22
IT-20C14	2011	Italy, Naples	512 (CC258)	3	≈110	BLD	**D0**	FII_{K2}-FIB	22
IT-06C07	**2011**	**Italy, Genoa**	**258 (CC258)**	**2**	**≈150 (166.484)**	**BLD**	**E0**	**FII_{K2}-FIB**	22
IT-12C73	**2011**	**Italy, Florence**	**101**	**2**	**≈110 (106.320)**	**BLD**	**F0**	**FII_{K2} and R**	22
IT-12C72	2011	Italy, Florence	101	2	≈100	BLD	**F1**	FII_{K2} and R	22
IT-12C47	**2011**	**Italy, Florence**	**101**	**2**	**≈110 (98.184)**	**BLD**	**F1**	**FII_{K2} and R**	22

Strains from which KPC-encoding plasmids were completely sequenced and characterized in this study are shown in bold.
[a]Sizes of all plasmids were deduced by S1 nuclease assay, the size of fully sequenced plasmids is reported in parentheses.
[b]Transfer frequencies are expressed as transconjugants per donor cell.
[c]BLD, below the limit of detection ($\leq1\times10^{-9}$).

subtypes (A0, A1, A2). Among the Greek collection almost all plasmids showed an indistinguishable restriction profile (A0) and were obtained from KPC-Kp belonging to different STs ($n=13$, including ST258 strains); the only exception was a plasmid showing a unique profile (type B0) obtained from an ST11 KPC-Kp (Table 1). On the other hand, a higher heterogeneity was observed among plasmids from the Italian collection that exhibited a total of seven distinct restriction patterns, five of which (types A1, A2, C0, D0 and E0) were observed in plasmids derived from the CC258 strains, and the two remaining (types F0 and F1) in plasmids from ST101 strains.

Replicon typing revealed that all plasmids belonging to RFLP types A (except for pGR-2878), B, D and E were positive for the $IncFII_K$ (K2) allele and an FIB-like *repA* gene, while RFLP type C was positive only for a FIB-like *repA* gene, and RFLP type F was positive for the FII_K (K2) and R replicons (Table 1).[11,30–32]

Overall, the present results revealed a predominance of KPC-encoding $IncFII_K$-FIB plasmids carrying the Tn*4401a* isoform in KPC-Kp strains representative of the early phases of the Greek and Italian epidemics, and were consistent with the data recently reported by a large study on KPC-Kp from colonized patients in Europe and Israel.[15]

Structure of KPC-encoding plasmids

The complete sequence of KPC-encoding plasmids representative of different RFLP types and subtypes ($n=9$) was determined.

Downloaded from http://jac.oxfordjournals.org/ at Universia degli Studi di Siena on June 29, 2016

All sequenced plasmids of RFLP type A (representative of subtypes A0, A1 and A2) showed a high similarity to each other and to the archetypal $IncFII_{K2}$ KPC-encoding plasmid pKpQIL (GenBank accession no. NC_014016), originally described in the ST258 *K. pneumoniae* Kpn557 isolated in Israel in 2006, and then reported worldwide (Figure S1, available as Supplementary data at *JAC* Online).[8] Differences among these plasmids consisted of insertion/deletion of IS elements (Figure S1) and in few SNPs (minimum of 6, maximum of 23), almost all located in intergenic regions or in mobile elements. A comparative analysis of RFLP type A plasmids with previously sequenced pKpQIL-like plasmids isolated in the USA in the late 2000s ($n=3$),[14] in 2011 ($n=3$)[35,36] or during the 2004–13 period ($n=5$),[18,37] revealed that the content and organization of these plasmids were overall stable despite their geographical and temporal distribution, and that SNP variations were minimal (minimum of 1, maximum of 30).

Plasmids pGR-1870 (RFLP type B0) from Greece and pIT-11C07 (RFLP type D0) from Italy appeared to be novel pKpQIL fusion and deletion derivatives in which different regions, covering the *tra* operon, had been replaced with the cognate segments of pKPN3 (GenBank accession no. CP000648), a non-KPC-encoding $IncFII_{K1}$-FIB plasmid described in *K. pneumoniae* MGH78578 (ATCC 700721) in 1994 (http://hamap.expasy.org/proteomes/KLEP7.html) (Figure 1). Recombination events occurred between homologous regions (adjacent to the *ardA* and *traU* or *traE* genes) present on both type B0 and type D0 plasmids and pKPN3 could have promoted these rearrangements. Compared with pKpQIL and with pGR-1870, pIT-11C07 lacked a 13 kb region downstream of Tn*4401a* (including remnants of transposons, ISs,

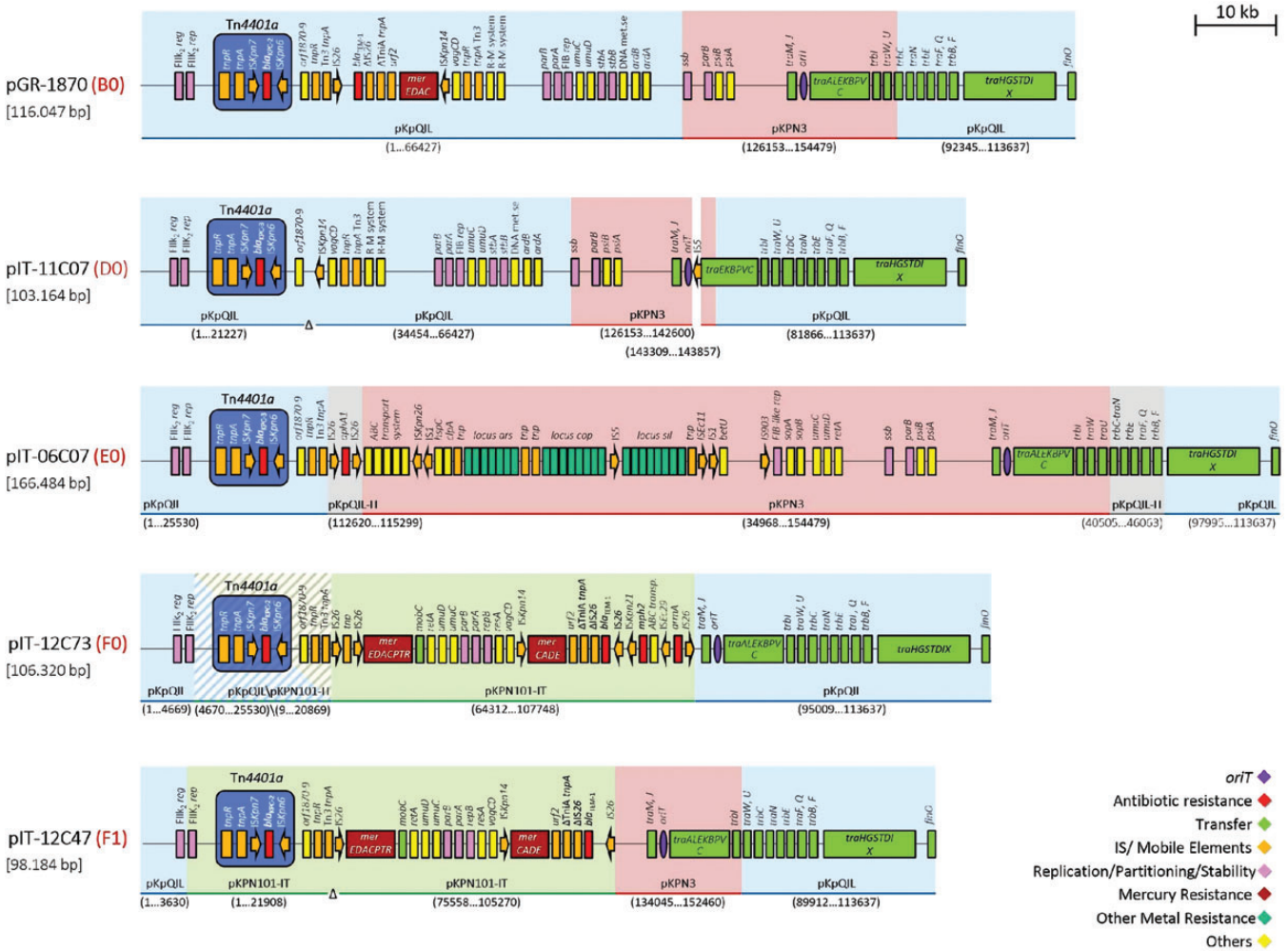

Figure 1. Linear maps of novel KPC-encoding derivative plasmids belonging to RFLP types B0, D0, E0, F0 and F1. RFLP group is stated in red flanking the respective plasmid name. Genes are represented by bars and are classified by function into different groups; intact IS are represented by arrows, showing the transcription direction, while truncated IS appear as rectangles. Boundaries of Tn*4401* transposon are also shown. For each plasmid, the coloured blocks identify the most similar (≥99% sequence identity) regions shared with other plasmids: light blue for pKpQIL (GenBank NC_014016), light grey for pKpQIL-IT (GenBank JN233705), light red for pKPN3 (GenBank CP000648) and light green for pKPN101-IT (GenBank JX283456). Striped box in pIT-12C73 represents a plasmid portion for which it was not possible to assess the precise DNA source (i.e. not enough SNPs were present). Nucleotide coordinates of comparator plasmids are also shown. This figure appears in colour in the online version of *JAC* and in black and white in the printed version of *JAC*.

Downloaded from http://jac.oxfordjournals.org/ at Universia degli Studi di Siena on June 29, 2016

the bla_{TEM-1} gene and a mercury resistance operon), and a small portion of the *tra* locus (including the *traAL* genes). Similar chimeric plasmids, even if differently rearranged, have also been described in KPC-Kp from the USA,[17,18] pointing out that recombination events between pKpQIL-like and pKPN3-like plasmids are common, likely due to the presence of highly homologous regions and their frequent coexistence in *K. pneumoniae*.[18,38]

Plasmid pIT-FIPP-1 (RFLP type C0) from the Italian KPC-Kp index strain was a deletion derivative of pKpQIL, where portions of the FII_{K2} replicon and part of the *tra* locus were lacking (Figure S1), thus explaining the failure in conjugal transfer of this RFLP type (Table 1). Of note, pIT-FIPP-1 was very similar (>99% nucleotide identity) to pKpQIL-LS6 (GenBank accession no. JX442975), which to date has been described only in Italy from ST258 *K. pneumoniae* LS6 isolated in 2011.[39] These findings suggest the presence, in Italy, of a defined pKpQIL lineage that originally emerged during the early stages of the KPC-Kp dissemination in this region and has circulated here since 2008.[21]

Plasmid pIT-06C07 (RFLP type E0) appeared to be a novel chimeric element resembling pKPN3, pKpQIL and pKpQIL-IT (GenBank accession no. JN233705), as also suggested by the presence of the IS*26*-*aphA1*-IS*26* composite transposon (the unique significant difference distinguishing pKpQIL-IT from pKpQIL) (Figure 1).[12] Complex rearrangements have occurred within the *tra* locus and a large recombination (likely occurred between the *traN* locus and an IS*26* element) might have led to the acquisition of a 51 kb segment from a pKPN3-like plasmid (belonging to the $IncFII_{K1}$-FIB family) to pKpQIL/pKpQIL-IT (belonging to the $IncFII_{K2}$-FIB family), thus generating the hybrid $IncFII_{K2}$-FIB pIT-06C97 plasmid. This hypothesis is also supported by the description of pKpQIL-IT (pKpQIL-like) and pKPN-IT (pKPN3-like) plasmids coexisting in the same ST258 KPC-Kp, isolated in Italy in 2010.[12]

Plasmid pIT-12C73 (RFLP type F, subtype F0) was a fusion derivative of pKpQIL and pKPN101-IT (GenBank accession no. JX283456), a multireplicon $IncFII_{K2}$-IncR KPC-encoding plasmid originally described from an ST101 KPC-Kp isolated in Italy in 2011.[40] Comparative analysis suggested that IS*26*-mediated recombination events likely played a major role in generating this fusion plasmid, which inherited the complete *tra* and *rep* loci from pKpQIL. Additionally to bla_{KPC}, pIT-12C73 carried also a macrolide (*mph2*) and an aminoglycoside (*armA*) resistance gene, as pKPN101-IT (Figure 1).

Finally, plasmid pIT-12C47 (RFLP type F, subtype F1) was a pKPN101-IT-related plasmid with a mosaic structure, where part of the *tra* and *rep* loci were replaced with cognate segments of pKPN3 and pKpQIL (Figure 1). Differently from pKPN101-IT and pIT-12C73, plasmid pIT-12C47 lacked a small IS*26* composite transposon (including a *tnpA* gene) downstream of Tn*4401a*, and the resistance region (including the *mph2* and *armA* genes) located downstream of bla_{TEM-1}. Interestingly, even though IncR pKPN101-IT-like plasmids have never been documented in STs different from ST101, and only a single description is available,[40] our findings suggest that a constant evolution by large genetic rearrangements occurred also within plasmids circulating in this ST (a clonal group sporadically detected in Italy)[22] as observed for the pKpQIL lineage in the ST258 strains.

Transferability of KPC-encoding plasmids

Plasmids of RFLP type A (the most prevalent, corresponding to pKpQIL-like plasmids) could be transferred by conjugation from several strains (belonging in STs 17, 35, 86, 133, 147, 274, 160, 494, 495 and 792), although with different transfer frequencies (ranging from 1×10^{-6} to 8×10^{-8} transconjugants per donor cell), but not in all cases. In particular, conjugal transfer of these plasmids was not detected from strains of CC258. Similarly, transferability was not observed for plasmids of RFLP types B–F (Table 1).

To investigate further the different transferability behaviour of the pKpQIL-like plasmids, two additional members of RFLP subtype A0, namely pGR-3913 and pGR-1780, which unlike pGR-1504 were transferable by conjugation (Table 1), were completely sequenced. Sequence comparison confirmed that these three plasmids were pKpQIL-like and almost identical to each other, and that pGR-3913 was the most similar to pGR-1504 (Table 1, Figure S1). Based on this, pGR-3913 was selected for additional conjugation experiments, together with pGR-1504. Both plasmids were first transferred by transformation into *E. coli* DH10B, and the respective transformants were then mated with *E. coli* J53 Azi^R. In these experiments, J53 transconjugants were obtained from both donors (DH10B/pGR-1504 and DH10B/pGR-3913) with a similar transfer frequency of $\sim1\times10^{-6}$ transconjugants per donor cell. These findings therefore indicated that differences in transferability of the two plasmids from their original hosts were apparently due to the different donor background rather than to minimal differences in the plasmid sequences.

Altogether, our results are consistent with previous observations that described successful conjugal transfer for pKpQIL-like plasmids from various hosts (including members of CC258) both to laboratory strains and *in vivo*, and underscored the role of horizontal spread of these plasmids in KPC-Kp dissemination.[41–49] The lack of detectable transferability of pKpQIL-like plasmids from CC258 KPC-Kp strains observed in this study was likely due to the limited sensitivity of the experimental methodology. Nevertheless, a lower transferability potential of KPC-encoding plasmids from strains of CC258 was evident, which could be consistent with the observation that expansion of CC258 clones has played a major role in KPC-Kp dissemination.[49] A number of factors might be responsible for the reduced ability of CC258 strains to transfer pKpQIL-like plasmids, and it would be interesting to investigate further these features using *in vivo* models.[50]

Conclusions

The present study investigated the population structure of KPC-encoding plasmids in *K. pneumoniae* from Greece and Italy, which are the two major endemic sites in Europe for this type of resistant pathogen.

Results revealed that pKpQIL-like plasmids played a major role in both places, even though with different dynamics. In Greece, a highly conserved KPC-2-encoding pKpQIL-like plasmid was observed in a polyclonal population of KPC-Kp (14 different STs), with ST258 as the predominant clonal lineage. In Italy, on the other hand, a variety of pKpQIL-like plasmids were found in an oligoclonal population of KPC-Kp, belonging almost exclusively in the CC258 (ST258 or ST512). This different epidemiological scenario could reflect, at least in part, the delayed emergence of bla_{KPC}-carrying plasmids in Italy, while additional factors could have reasonably contributed, including a different genetic background of circulating CC258 *K. pneumoniae* clones (i.e. belonging to the recently identified clade I or clade II).[2,8] In fact, the CC258

Downloaded from http://jac.oxfordjournals.org/ at Universia degli Studi di Siena on June 29, 2016

KPC-Kp clones circulating in Italy belonged to both clades, with the predominance of clade II,[38,51] and might have driven a possible segregation and a parallel evolution/recombination of pKpQIL-like plasmids within an oligoclonal, but well distinct, population of KPC-Kp. Conversely, the absolute predominance of strains producing KPC-2,[4,5] which appears to be strongly associated with clade I,[2,8,38] could have favoured the persistence of a more homogeneous plasmid population in Greece.

Acknowledgements

This work was partially presented at the 42nd National Congress of the Italian Society of Microbiology (SIM), Turin, Italy, 28 September–1 October 2014 (Abstract number P51).

Funding

This work was partially supported by European Community FP7 no. 282004 (EvoTAR) to G. M. R.

Transparency declarations

None to declare.

Supplementary data

Figure S1 is available as Supplementary data at *JAC* Online (http://jac.oxfordjournals.org/).

References

1 Tumbarello M, Trecarichi EM, De Rosa FG *et al*. Infections caused by KPC-producing *Klebsiella pneumoniae*: differences in therapy and mortality in a multicentre study. *J Antimicrob Chemother* 2015; **70**: 2133–43.

2 Pitout JD, Nordmann P, Poirel L. Carbapenemase-producing *Klebsiella pneumoniae*, a key pathogen set for global nosocomial dominance. *Antimicrob Agents Chemother* 2015; **59**: 5873–84.

3 Albiger B, Glasner C, Struelens MJ *et al*. Carbapenemase-producing *Enterobacteriaceae* in Europe: assessment by national experts from 38 countries, May 2015. *Euro Surveill* 2015; **20**: pii=30062.

4 Giakkoupi P, Papagiannitsis CC, Miriagou V *et al*. An update of the evolving epidemic of bla_{KPC-2}-carrying *Klebsiella pneumoniae* in Greece (2009–10). *J Antimicrob Chemother* 2011; **66**: 1510–3.

5 Giakkoupi P, Maltezou HC, Polemis M *et al*. KPC-2-producing *Klebsiella pneumoniae* infections in Greek hospitals are mainly due to a hyperendemic clone. *Euro Surveill* 2009; **14**: pii=19218.

6 Bonura C, Giuffrè M, Aleo A *et al*. An update of the evolving epidemic of bla_{KPC} carrying *Klebsiella pneumoniae* in Sicily, Italy, 2014: emergence of multiple non-ST258 clones. *PLoS One* 2015; **10**: e0132936.

7 Cuzon G, Naas T, Truong H *et al*. Worldwide diversity of *Klebsiella pneumoniae* that produce β-lactamase bla_{KPC-2} gene. *Emerg Infect Dis* 2010; **16**: 1349–56.

8 Chen L, Mathema B, Chavda KD *et al*. Carbapenemase-producing *Klebsiella pneumoniae*: molecular and genetic decoding. *Trends Microbiol* 2014; **22**: 686–96.

9 Leavitt A, Chmelnitsky I, Carmeli Y *et al*. Complete nucleotide sequence of KPC-3-encoding plasmid pKpQIL in the epidemic *Klebsiella pneumoniae* sequence type 258. *Antimicrob Agents Chemother* 2010; **54**: 4493–6.

10 Mathers AJ, Peirano G, Pitout JD. The role of epidemic resistance plasmids and international high-risk clones in the spread of multidrug-resistant *Enterobacteriaceae*. *Clin Microbiol Rev* 2015; **28**: 565–91.

11 Baraniak A, Grabowska A, Izdebski R *et al*. Molecular characteristics of KPC-producing *Enterobacteriaceae* at the early stage of their dissemination in Poland, 2008-2009. *Antimicrob Agents Chemother* 2011; **55**: 5493–9.

12 Garcıa-Fernadez A, Villa L, Carta C *et al*. *Klebsiella pneumoniae* ST258 producing KPC-3 identified in Italy carries novel plasmids and OmpK36/OmpK35 porin variants. *Antimicrob Agents Chemother* 2012; **56**: 2143–5.

13 Hidalgo-Grass C, Warburg G, Temper V *et al*. KPC-9, a novel carbapenemase from clinical specimens in Israel. *Antimicrob Agents Chemother* 2012; **56**: 6057–9.

14 Chen L, Chavda KD, Melano RG *et al*. Comparative genomic analysis of KPC-encoding pKpQIL-like plasmids and their distribution in New Jersey and New York Hospitals. *Antimicrob Agents Chemother* 2014; **58**: 2871–7.

15 Baraniak A, Izdebski R, Fiett J *et al*. KPC-Like carbapenemase-producing Enterobacteriaceae colonizing patients in Europe and Israel. *Antimicrob Agents Chemother* 2015; **60**: 1912–7.

16 Findlay J, Hopkins KL, Doumith M *et al*. KPC enzymes in the UK: an analysis of the first 160 cases outside the North-West region. *J Antimicrob Chemother* 2016; **71**: 1199–206.

17 Chen L, Chavda KD, Melano RG *et al*. Complete sequence of a bla_{KPC-2}-harboring IncFII(K1) plasmid from a *Klebsiella pneumoniae* sequence type 258 strain. *Antimicrob Agents Chemother* 2013; **57**: 1542–5.

18 Wright MS, Perez F, Brinkac L *et al*. Population structure of KPC-producing *Klebsiella pneumoniae* isolates from midwestern U.S. hospitals. *Antimicrob Agents Chemother* 2014; **58**: 4961–5.

19 Chmelnitsky I, Shklyar M, Leavitt A *et al*. Mix and match of KPC-2 encoding plasmids in Enterobacteriaceae-comparative genomics. *Diagn Microbiol Infect Dis* 2014; **79**: 255–60.

20 Giakkoupi P, Pappa O, Polemis M *et al*. Emerging *Klebsiella pneumoniae* isolates coproducing KPC-2 and VIM-1 carbapenemases. *Antimicrob Agents Chemother* 2009; **53**: 4048–50.

21 Giani T, D'Andrea MM, Pecile P *et al*. Emergence in Italy of *Klebsiella pneumoniae* sequence type 258 producing KPC-3 carbapenemase. *J Clin Microbiol* 2009; **47**: 3793–4.

22 Giani T, Pini B, Arena F *et al*. Epidemic diffusion of KPC carbapenemase-producing *Klebsiella pneumoniae* in Italy: results of the first countrywide survey, 15 May to 30 June 2011. *Euro Surveill* 2013; **18**: pii=20489.

23 Papagiannitsis CC, Giakkoupi P, Kotsakis SD *et al*. OmpK35 and OmpK36 porin variants associated with specific sequence types of *Klebsiella pneumoniae*. *J Chemother* 2013; **25**: 250–4.

24 Diancourt L, Passet V, Verhoef J *et al*. Multilocus sequence typing of *Klebsiella pneumoniae* nosocomial isolates. *J Clin Microbiol* 2005; **43**: 4178–82.

25 Naas T, Cuzon G, Villegas MV *et al*. Genetic structure at the origin of acquisition of the β-lactamase bla_{KPC} gene. *Antimicrob Agents Chemother* 2008; **52**: 1257–63.

26 Barton BM, Harding GP, Zuccarelli AJ. A general method for the detecting and sizing large plasmids. *Anal Biochem* 1995; **226**: 235–40.

27 Vatopoulos AC, Philippon A, Tzouvelekis LS *et al*. Prevalence of a transferable SHV-5 type β-lactamase in clinical isolates of *Klebsiella pneumoniae* and *Escherichia coli* in Greece. *J Antimicrob Chemother* 1990; **26**: 635–48.

28 McConnell MM, Willshaw GA, Smith HR *et al*. Transposition of ampicillin resistance to an enterotoxin plasmid in an *Escherichia coli* strain of human origin. *J Bacteriol* 1979; **139**: 346–55.

29 Sambrook J, MacCallum P, Russell D. *Molecular Cloning: A Laboratory Manual*, 3rd edn. New York: Cold Spring Harbor, 2001.

Downloaded from http://jac.oxfordjournals.org/ at Universia degli Studi di Siena on June 29, 2016

30 Carattoli A, Bertini A, Villa L *et al*. Identification of plasmids by PCR-based replicon typing. *J Microbiol Methods* 2005; **63**: 219–28.

31 Johnson TJ, Bielak EM, Fortini D *et al*. Expansion of the IncX plasmid family for improved identification and typing of novel plasmids in drug-resistant *Enterobacteriaceae*. *Plasmid* 2012; **68**: 43–50.

32 Villa L, García-Fernández A, Fortini D *et al*. Replicon sequence typing of IncF plasmids carrying virulence and resistance determinants. *J Antimicrob Chemother* 2010; **65**: 2518–29.

33 Simpson JT, Wong K, Jackman SD *et al*. ABySS: a parallel assembler for short read sequence data. *Genome Res* 2009; **19**: 1117–23.

34 Darling AE, Mau B, Perna NT. progressiveMauve: multiple genome alignment with gene gain, loss and rearrangement. *PLoS One* 2010; **5**: e11147.

35 Marsh JW, Krauland MG, Nelson JS *et al*. Genomic epidemiology of an endoscope-associated outbreak of *Klebsiella pneumoniae* carbapenemase (KPC)-producing *K. pneumoniae*. *PLoS One* 2015; **10**: e0144310.

36 Snitkin ES, Zelazny AM, Thomas PJ *et al*. Tracking a hospital outbreak of carbapenem-resistant *Klebsiella pneumoniae* with whole-genome sequencing. *Sci Transl Med* 2012; **4**: 148ra116.

37 Conlan S, Thomas PJ, Deming C *et al*. Single-molecule sequencing to track plasmid diversity of hospital-associated carbapenemase-producing Enterobacteriaceae. *Sci Transl Med* 2014; **6**: 254ra126.

38 Bowers JR, Kitchel B, Driebe EM *et al*. Genomic analysis of the emergence and rapid global dissemination of the clonal group 258 *Klebsiella pneumoniae* pandemic. *PLoS One* 2015; **10**: e0133727.

39 Villa L, Capone A, Fortini D *et al*. Reversion to susceptibility of a carbapenem-resistant clinical isolate of *Klebsiella pneumoniae* producing KPC-3. *J Antimicrob Chemother* 2013; **68**: 2482–6.

40 Frasson I, Lavezzo E, Franchin E *et al*. Antimicrobial treatment and containment measures of an extremely drug-resistant *Klebsiella pneumoniae* ST101 isolate carrying pKPN101-IT, a novel fully sequenced bla_{KPC-2} plasmid. *J Clin Microbiol* 2012; **50**: 3768–72.

41 Sidjabat HE, Silveira FP, Potoski BA *et al*. Interspecies spread of *Klebsiella pneumoniae* carbapenemase gene in a single patient. *Clin Infect Dis* 2009; **49**: 1736–8.

42 Goren MG, Carmeli Y, Schwaber MJ *et al*. Transfer of carbapenem-resistant plasmid from *Klebsiella pneumoniae* ST258 to *Escherichia coli* inpatient. *Emerg Infect Dis* 2010; **16**: 1014–7.

43 Leavitt A, Chmelnitsky I, Ofek I *et al*. Plasmid pKpQIL encoding KPC-3 and TEM-1 confers carbapenem resistance in an extremely drug-resistant epidemic *Klebsiella pneumoniae* strain. *J Antimicrob Chemother* 2010; **65**: 243–8.

44 Adler A, Shklyar M, Schwaber MJ *et al*. Introduction of OXA-48-producing Enterobacteriaceae to Israeli hospitals by medical tourism. *J Antimicrob Chemother* 2011; **66**: 2763–6.

45 Cantón R, Akóva M, Carmeli Y *et al*. Rapid evolution and spread of carbapenemases among *Enterobacteriaceae* in Europe. *Clin Microbiol Infect* 2012; **18**: 413–31.

46 Sheng JF, Li JJ, Tu S *et al*. bla_{KPC} and *rmtB* on a single plasmid in *Enterobacter amnigenus* and *Klebsiella pneumoniae* isolates from the same patient. *Eur J Clin Microbiol Infect Dis* 2012; **31**: 1585–91.

47 Warburg G, Hidalgo-Grass C, Partridge SR *et al*. A carbapenem-resistant *Klebsiella pneumoniae* epidemic clone in Jerusalem: sequence type 512 carrying a plasmid encoding aac(6')-Ib. *J Antimicrob Chemother* 2012; **67**: 898–901.

48 Gona F, Barbera F, Pasquariello AC *et al*. *In vivo* multiclonal transfer of *bla*(KPC-3) from *Klebsiella pneumoniae* to *Escherichia coli* in surgery patients. *Clin Microbiol Infect* 2014; **20**: O633–5.

49 Adler A, Khabra E, Paikin S *et al*. Dissemination of the bla_{KPC} gene by clonal spread and horizontal gene transfer: comparative study of incidence and molecular mechanisms. *J Antimicrob Chemother* 2016; doi:10.1093/jac/dkw106.

50 Göttig S, Gruber TM, Stecher B *et al*. *In vivo* horizontal gene transfer of the carbapenemase OXA-48 during a nosocomial outbreak. *Clin Infect Dis* 2015; **60**: 1808–15.

51 D'Andrea MM, Amisano F, Giani T *et al*. Diversity of capsular polysaccharide gene clusters in Kpc-producing *Klebsiella pneumoniae* clinical isolates of sequence type 258 involved in the Italian epidemic. *PLoS One* 2014; **9**: e96827.

Downloaded from http://jac.oxfordjournals.org/ at Universia degli Studi di Siena on June 29, 2016

Supplementary data

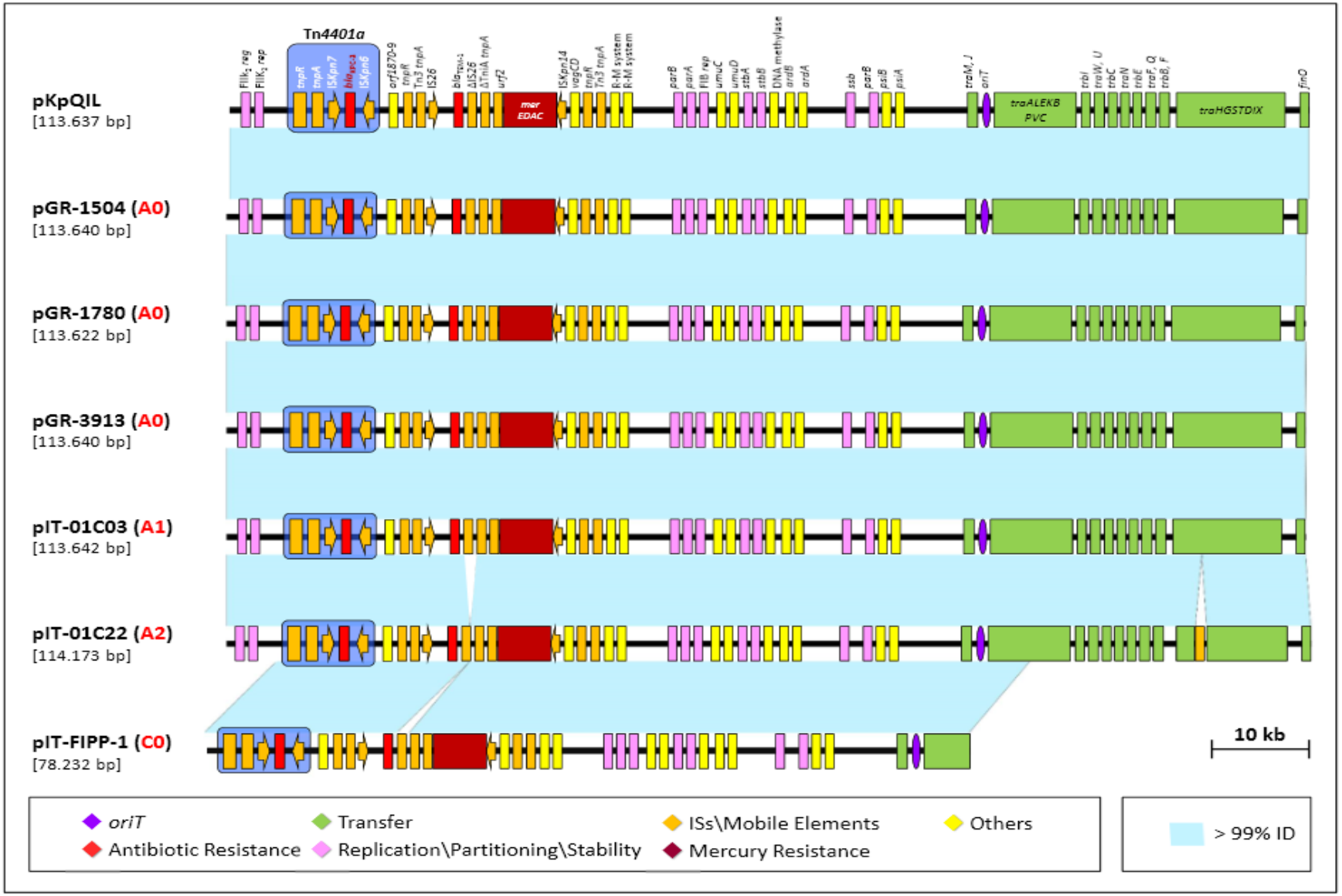
Tn4401a
pKpQIL
[113.637 bp]
pGR-1504 (A0)
[113.640 bp]
pGR-1780 (A0)
[113.622 bp]
pGR-3913 (A0)
[113.640 bp]
pIT-01C03 (A1)
[113.642 bp]
pIT-01C22 (A2)
[114.173 bp]
pIT-FIPP-1 (C0)
[78.232 bp]
10 kb
oriT
Transfer
ISs\Mobile Elements
Others
Antibiotic Resistance
Replication\Partitioning\Stability
Mercury Resistance
> 99% ID

Figure S1. Linear map and comparison of sequenced KPC-encoding plasmids belonging to RFLP types A (n=5) and C (n=1). For each plasmid, the RFLP group is indicated in red flanking the respective name. Genes are represented by bars and are classified by function into different groups only for pKpQIL plasmid, used as reference element. Boundaries of Tn*4401* transposon are also shown. Homologous segments are indicated by light blue shading, representing ≥99% sequence identity. Compared to pKpQIL, the variation was of 6 SNPs for pGR-1504, 8 SNPs for pGR-1780, 10 SNPs for pGR-3913, 15 SNPs for pIT-01C03 and of 23 SNPs for pIT-01C22 (with almost all polymorphisms located in intergenic regions or mobile elements). The RFLP subtype A0 plasmids pGR-1504 and pGR-3913, selected for additional transfer experiment (please refer to the Transferability of KPC-encoding plasmids subsection for further details), differed in 4 SNPs only: 1 SNP was located within an intergenic region, 1 SNP caused a silent mutation within the *traN* gene, and 2 SNPs caused missense mutations within the *traC* gene (conservative mutation) and a hypothetical protein (non-conservative mutation). This figure appears in colour in the online version of *JAC* and in black and white in the print version of *JAC*.